STUDENT REPORTS

International Summer Student Program 2002

DESY Zeuthen, Germany

Contents

Preface

This book consists of a compilation of reports from almost all students who participated in the DESY Zeuthen Student Program 2002, from the 16^{th} of July to the 6^{th} of September. These reports span almost all disciplines linked with Physics that are studied in DESY Zeuthen.

All the authors of this book whould like to thank the DESY Zeuthen for this instructive stay, and personally thank all their tutors for the help of making these scientific studies. This book is dedicated to all people who took part to organize Student Program 2002, especially to Karl-Heinz Hiller.

I whould like to acknowledge all the students who gave me some important suggestions in the preparation of this Report Book. I belive that a good tradition of making Student Report Books has been born and will continue to exist many many years...

Boris Skorodumov

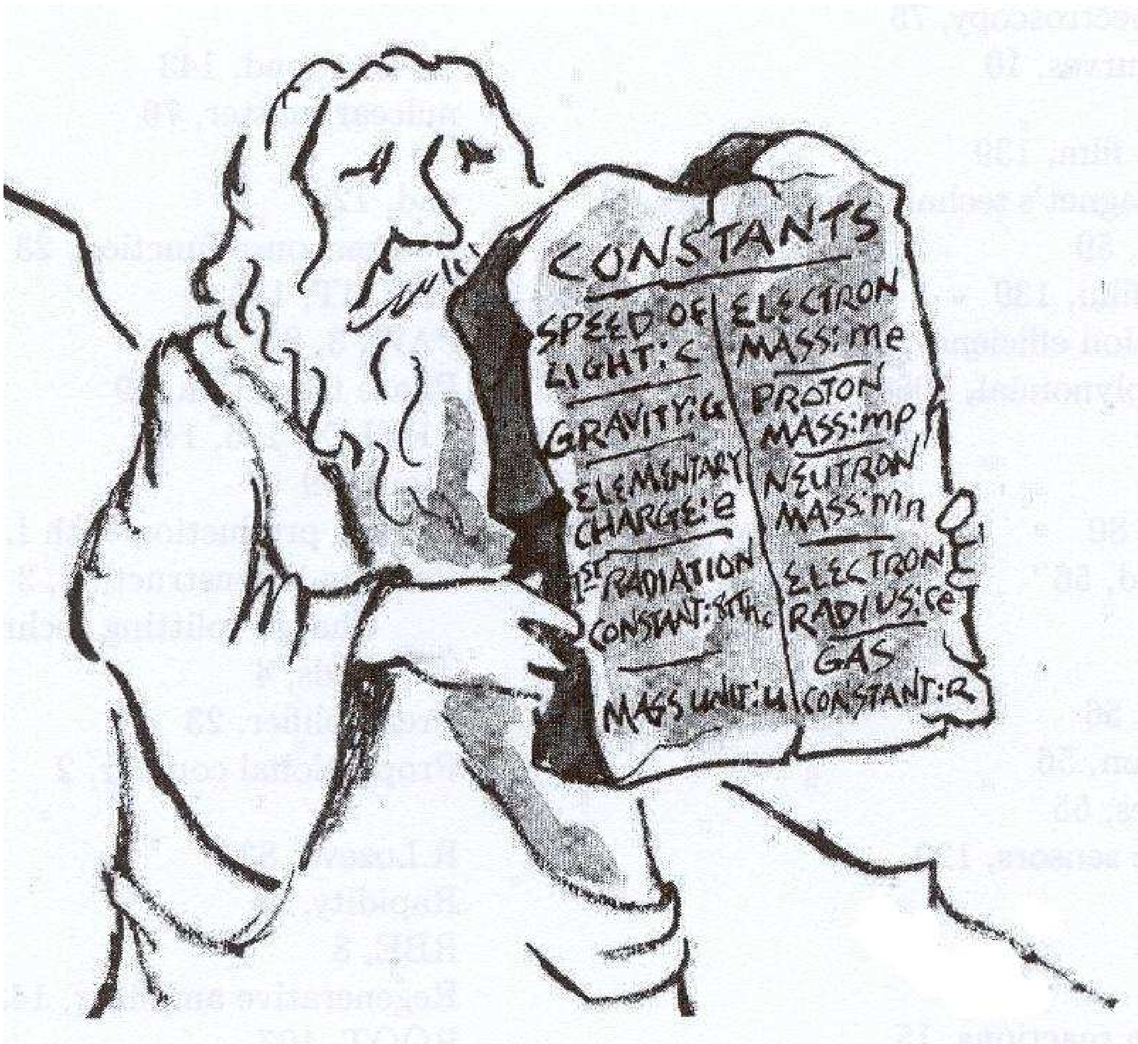
CONSTANTS
SPEED OF LIGHT: c
ELECTRON MASS: me
GRAVITY: G
PROTON MASS: mp
ELEMENTARY CHARGE: e
NEUTRON MASS: mn
1ST RADIATION CONSTANT: 8πhc
ELECTRON RADIUS: re
GAS CONSTANT: R
MASS UNIT: u

Vacuum polarization, gauge symmetries and path integral

Iván Calvo
Departamento de F´isica Teórica
Universidad de Zaragoza
E-mail: icalvo@dftuz.unizar.es

In this report I explain the most important concepts I have lernt during the Summer Student Program 2002 at DESY Zeuthen under the supervision of Fred Jegerlehner and Mikhail Kalmykov. My work consisted of two different parts. First, I worked out the calculations of the vacuum polarization effect in QED, which was very useful to have a first contact with dimensional regularization and renormalization theory. Then, I studied Yang-Mills theories, Goldstone theorem and Higgs mechanism in a classical way. The quantization of non-abelian gauge theories requires the path integral approach to QFT and my next step was the study of such tool. I finished my work learning how to construct the path integral for scalar, Dirac and gauge bosons fields.

1 Vacuum Polarization in QED

1.1 Introduction

The tree level Feynman diagram for the calculation of the scattering of an electron from a heavy target looks like shown in Fig. 1.

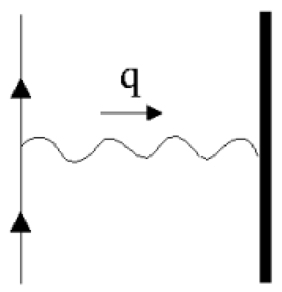

Fig. 1: *Tree level scattering of an electron from a heavy target*

However, in higher orders of perturbation theory, this result is modified by several types of radiative corrections, among which vacuum polarization (also called photon self-energy) plays an important role. It can be viewed as a modification to the free photon propagator by a virtual electron-positron pair (Fig. 2). As we shall see, the modification of the propagator implies the renormalizacion of the coupling constant α, which will not be constant anymore, but it will depend on the external momentum q.

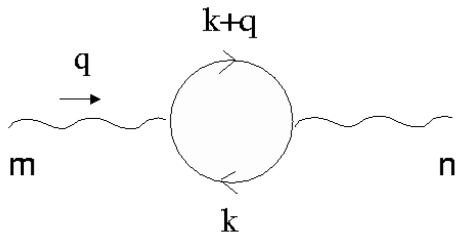

Fig. 2: *Vacuum polarization diagram*

1.2 Renormalization of the electric charge

Let us denote by $i\Pi^{\mu\nu}$ (polarization tensor) the photon propagator including all 1-particle-irreducible insertions (represented by a diagram that cannot be split into two diagrams by removing a single line).

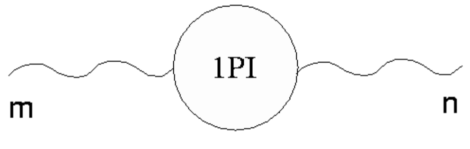

The exact photon propagator must have the form $\Pi^{\mu\nu}(q) = (q^2 g^{\mu\nu} - q^\mu q^\nu)\Pi(q^2)$ due to the

Ward identity, where $\Pi(q^2)$ is regular at $q^2 = 0$. Using this notation, the exact photon propagator is

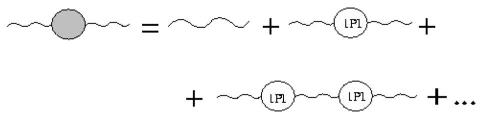

$$S_{\mu\nu}(q) = \frac{-ig_{\mu\nu}}{q^2} + \frac{-ig_{\mu\rho}}{q^2}[i(q^2 g^{\rho\sigma} - q^\rho q^\sigma)\Pi(q^2)]\frac{-ig_{\sigma\nu}}{q^2} + ...$$

This is a geometrical series that can be summed up to yield (by using again the Ward identity and throwing away terms proportional to q^μ or q^ν which will disappear when contracting the propagator with a fermion line),

$$S_{\mu\nu} = \frac{-ig_{\mu\nu}}{q^2(1-\Pi(q^2))}$$

which shows that the exact propagator has always a pole in $q^2 = 0$ (because $\Pi(q^2)$ is regular) and hence, the photon remains massless at all orders in perturbation theory.

The residue of the $q^2 = 0$ pole is $Z_3 \equiv \frac{1}{1-\Pi(0)}$

The ampitude for any low-q^2 scattering process will be shifted by this factor, relative to the tree level approximation. Since a factor of e_0 lies at each end of the photon propagator, we can account for this shift by replacing $e_0 \to \sqrt{Z_3}e_0$. This replacement is called **charge renormalization**. It is e and not e_0 which is measured in experiments.

The full effect of replacing the tree level photon propagator with the exact photon propagator to lowest order in α is to replace

$$\alpha_0 \to \alpha_{eff}(q^2) = \frac{e^2/4\pi}{1-[\Pi_2(q^2)-\Pi_2(0)]}$$

where the subscript 2 in the polarization tensor makes reference to the lowest order correction in α to the photon propagator, which corresponds to Fig. 2.

1.3 Computation of Π_2

$$i\Pi_{\mu\nu}(q) = \\ = e^2 \int \frac{d^4k}{(2\pi)^4} Tr[\gamma^\mu \frac{i}{k^\mu\gamma_\mu - m}\gamma^\nu \frac{i}{k^\mu\gamma_\mu + q^\mu\gamma_\mu - m}]$$

I will only sketchly explain how to calculate the polarization function. The first step is to perform a Wick rotation, getting an euclidean metric. It allows to introduce a Feynman parameter and leave and integral which only depends on k^2. After doing this, it is easy to see that our integral is badly divergent in the usual sense. So, if we want to get finite results we must do some prescriptions to define our otherwise infinite expressions. These prescriptions are called **regularizations**. There are many ways to regularize an integral and for systems with several types of symmetries the result can depend on the regularization. When two regulators give different answers for observable quantities, it is generally because some symmetry is being violated by one or both of them. In these cases we take the symmetry to be fundamental and demand that it be preserved by the regulator.

Dimensional regularization ('t Hooft and Veltman, Nucl. Phys. B44, 189. 1972) has become a very popular method since it is quite transparent and preserves automatically the symmetries of the system which do not depend on the space-time dimension. The idea of dimensional regularization is simple to state: compute the Feynman diagram as an analytic function of the dimensionality of space-time, d. Any observable quantity should have a well-defined limit as $\epsilon \to 0, \epsilon = 4 - d$.

In our case, the polarization function has not a well-defined limit

$$\Pi_2(q^2) = -\frac{2\alpha}{\pi}\int_0^1 dxx(1-x)(\frac{2}{\epsilon} - log\Delta - \gamma) + o(\epsilon)$$

but the difference

$$\Pi_2'(q^2) \equiv \Pi_2(q^2) - \Pi_2(0)$$

has got, yielding

$$\Pi_2'(q^2) = \frac{-2\alpha}{\pi}\int_0^1 dxx(1-x)\log\frac{m^2}{m^2 - x(1-x)q^2}$$

It can be shown that in the nonrelativistic limit, when it makes sense to calculate the potential $V(r)$ created by the heavy target, the vacuum polarization diagram modifies the Coulomb potential with a short range term (of the order of the electron wavelenght) that screens the charge of the electron. The effect reminds that observed in a dielectric, where the dipoles are, now, the electron-positron pairs.

2 Global and local gauge symmetries and Yang-Mills theories

2.1 Global gauge symmetry

It is well known that the Klein-Gordon (for a complex field) and Dirac lagrangian densities exhibit global U(1) symmetry which is related to electric charge conservation.

It is easy to construct theories with larger symmetry groups, just by taking multiplets of n scalar fields or spinors. If we denote those multiplets by $\Phi(x)$ and $\Psi(x)$ respectively, the lagrangian densities

$$L_0^\Phi = (\partial_\mu \Phi)^+ (\partial^\mu \Phi) - \mu^2 \Phi^+ \Phi$$

$$L_0^\Psi = \bar{\Psi}\,(i\gamma^\mu \partial_\mu - m)\Psi$$

posses U(n) *global* symmetry, i.e., they are invariant under a U(n) transformation in which the multiplets of fields transform as vectors under the fundamental represantion of this group and where the U(n) transformation does not depend on the space-time point. The equations of motion are equivalent to n free scalar and Dirac fields. In fact, as long as U(n)=U(1)xSU(n), we will restrict ourselves to consider only SU(n) transformations.

2.2 Local gauge symmetry

Global gauge symmetry can be viewed as a manifestation that physics does not depend on the coordinate system for the internal degrees of freedom. It seems natural to impose that our physical laws be also the same when the observers at different points of space-time choose these coordinate systems independently. This means that our lagrangian density should be invariant under *local* SU(n) transformations.

It is clear that L_0^Φ and L_0^Ψ do not have this kind of symmetry. Under very general assumptions, it can be shown that the only way to make these lagrangian densities locally symmetric is by substituting the ordinary derivative ∂_μ by the covariant derivative

$$D_\mu = \partial_\mu - igV_\mu = \partial_\mu - igT_k V_\mu^k$$

where $T_k, k = 1, ..., n^2-1$ are the generators of the group in the fundamental representation, g is the coupling constant and V_μ^k are additional vector fields whose transformation law will compensate the undesirable terms resulting from the transformation of the matter fields and will make the lagrangian density invariant. This transformation law reads:

$$V_\mu \to V'_\mu = U(x)(V_\mu - \tfrac{i}{g} U^{-1}(\partial_\mu U))U^{-1}(x)$$

and for infinitesimal transformations,

$$V'^i_\mu = V^i_\mu - gc_{ikl} V^l_\mu \omega^k + \partial_\mu \omega^i$$

where $\omega^k(x)$ are the parameters of the local gauge transformation. This means that for infinitesimal transformations, the vector fields change under the adjoint representation of SU(n).

2.3 Yang-Mills theories

We have just seen that the postulate of local gauge invariance implies the introduction of gauge vector fields. For U(1) we reproduce the well known electromagnetic interaction where A_μ corresponds to the photon field. It is natural, then, to interpret the vector fields as the bosons which carry the intereaction for the general SU(n) case. If we want to construct the dynamics of a theory with such an interaction we need to introduce a gauge invariant kinetic term for the vector fields. The right expression for this term is:

$$L_{YM} = \frac{-1}{4} \sum_{i=1}^{n^2-1} G^i_{\mu\nu} G^{i\mu\nu}$$

where

$$G^i_{\mu\nu} = \partial_\mu V^i_\nu - \partial_\nu V^i_\mu + gc_{ijk} V^j_\mu V^k_\nu$$

L_{YM} by itself defines the so called pure Yang-Mills theory and

$$L = \frac{-1}{4} \sum_{i=1}^{n^2-1} G^i_{\mu\nu} G^{i\mu\nu} + \bar{\Psi}\,(i\gamma^\mu D_\mu - m)\Psi$$

is the local gauge invariant Yang-Mills lagrangian density, describing a multiplet of n spinors which suffer the interaction carried by n^2-1 vector fields.

We should notice four important points:

1) The postulate of local gauge invariance gives automatically the form of the interaction. Furthermore, the possible fundamental interactions that can be found in nature is restricted to a very small number.

2) QED is not only a particular case of gauge theory, but a very special one due to the abelian character of the symmetry group. In fact, it is the only case in which the gauge bosons do not couple to themselves. Photons couple to electric charge and they are electrically neutral, whereas the gauge bosons in the non-abelian cases carry non-zero value of the quantum nuber to which they couple.

3) There are more lagrangian densities which satisfy the local gauge invariance. However,

some of the, in principle, possible terms are rejected by imposing renormalizability. The rest of gauge invariant terms that do not appear in L are of dimension larger than four and therefore, irrelevant.

4) A mass term for the gauge bosons is not gauge invariant and therefore, not allowed. Massive gauge bosons obtain their masses through a quite tricky process called Higgs machanism, which is treated below.

3 Spontaneous symmetry breaking. Goldstone theorem and Higgs mechanism

3.1 Spontaneous breaking of a global symmetry. Goldstone theorem

Let L be a lagrangian which is symmetric under a global transformation F (which could belong to a transformation group G). We say that the symmetry is spontaneously broken if the ground state (vacuum) of the system is not invariant under such transformation. It means that the vacuum is not unique, and it usually happens that there exists a field $\phi(x)$ which has got non-vanishing value in the ground state in the classical case or non-zero expectation value in the vacuum state in quantum theories.

The Goldstone theorem states that $\phi(x)$ must be, in the general case, a multiplet of n complex scalar fields (2n real fields) which describes a number of massless particles equal to the number of broken symmetries (**Goldstone bosons**) and a number of massive particles equal to the remaining number of degrees of freedom. In the case of $G = SU(n)$ there are $2n - 1$ Goldstone bosons and one massive scalar particle.

3.2 Spontaneous breaking of a local symmetry. Higgs mechanism

Let us consider a Yang-Mills theory coupled to a multiplet of n scalar fields (so that the total lagrangian is invariant under $SU(n)$ transformations) in a special way:

$$L = \frac{-1}{4}(F_{\mu\nu})^2 + (D_\mu\Phi)^+(D^\mu\Phi) - V(\Phi)$$

$$V(\Phi) = -\mu^2\Phi^+\Phi + \frac{\lambda}{2}(\Phi^+\Phi)^2, \mu^2, \lambda > 0$$

The scalar part shows a spontaneous symmetry breaking in the sense of the preceding subsection, but the final result will be quite different. When the scalar field is expressed as $\Phi(x) = \Phi_0 + \Phi'(x)$ (where Φ_0 is the vacuum expectation value of $\Phi(x)$), there appear a semi-positive definite term which gives masses≥ 0 to the gauge bosons (coming from the covariant derivative), and a term which does the same with scalar fields $\Phi'(x)$ (coming from the cuadratic part of the potential). In fact, there are as many massless scalar bosons (Goldstone bosons) as massive gauge bosons, and this number equals the number of spontaneously broken symmetries.

However, due to the local character of the symmetry, the Goldstone bosons can be completely removed from the theory, and they are called **Goldstone ghosts**. Notice that the massive gauge bosons have gained one degree of freedom, which is compensated by the disappearance of a Goldstone boson in such a way that the total number of degrees of freedom of the system remains constant.

This process, by which the gauge bosons as well as the fermions in the Standard Model acquire mass without violating the gauge symmetry, is known as the **Higgs mechanism**.

The massive scalar fields generated by this mechanism remain as real particles. In the Standard Model one of this particles appears in the theory: the renowned **Higgs boson**.

4 Path integral quantization of Yang-Mills theories

4.1 Introduction to Path integral formalism

Path Integral (also called functional integral) was introduced by Feynman in 1940's. For many years the canonical quantization method was still the favourite one for physicists because it has got a clear physical interpretation and is mathematically well defined. However, everything changed in 1970's when it was discovered that the quantization and derivation of Feynman rules for non-abelian gauge theories could be carried out using the path integral approach.

I will not try to give a precise mathematical meaning for the path integrals. Whenever it can be done, it is a subtle topic, and there are many cases in which this rigorous treatment simply cannot be done. Instead of that, I will quote some formal expressions which show the equivalence of the canonical and path integral approaches and I will construct the path integral for bosons, fermions and Yang-Mills fields.

4.2 Path integral for bosons

It is possible to show that the following formal expression holds for a real-valued scalar field:

$$Z[J] \equiv< 0|T \exp i \int d^d x \phi(x) J(x)|0 >=$$

$$\int_o D\phi(x) \exp i \int d^d x[L(\phi(x)) + \phi(x)J(x)]$$

where the subscript o means that the path integral measure is normalized so that $Z[0] = 1$. $Z[J]$ is called generating functional, because the Green functions are obtained by functional derivation with respect to $J(x)$.

Intuitively, a path integral is a sum over the fields configurations. The measure $D\phi(x)$ is the limit when N tends to infinity of $\prod_{i=1}^{N} d\phi(x_i)$ and the integrand, then, is a function of infinite variables, which is precisely an intuitive form to understand a functional.

The path integral defined in this way defines a probability distribution for $J(x) = 0$ and we easily find a functional integral expression for the Green functions (which in our new approach remind the correlation functions of statistical mechanics) of our theory:

$$(-i)^n \frac{\delta^n}{\delta J(x_1)...\delta J(x_n)} Z[J]|_{J=0} =$$

$$=< 0|T\phi(x_1)...\phi(x_n)|0 >=$$

$$= \int_o D\phi(x)\phi(x_1)...\phi(x_n) \exp i \int d^d x L(\phi) =$$

$$=< \phi(x_1)...\phi(x_n) >$$

Hence, the path integral formulation contains all the information of the quantum theory, and provides a non-perturbative approach (notice that the splitting of L into a free term and an interaction term no longer appears).

Furthermore, in the functional integral formalism we do not need to talk about operators and Hilbert spaces. Only classical fields are used.

4.3 Path integral for fermions

The fermionic case is mathematically more complicated than the bosonic one and less intuitive. The generating functional for Dirac fields reads:

$$Z[\bar{\xi}, \xi] \equiv< 0|T \exp i \int d^d x(\bar{\xi}\ \Psi + \bar{\Psi}\ \xi)|0 >=$$

$$\int_o \prod_x d\bar{\Psi}_x d\Psi_x \exp i \int d^d x[L(\bar{\Psi}, \Psi) + \bar{\xi}\Psi + \bar{\Psi}\xi]$$

where now all the fields in the integrand are anticommuting classical objects called **Grassmann variables**. All the anticommutators that can be formed with $\xi(x), \bar{\xi}(x), \Psi(x), \bar{\Psi}(x)$ vanish.

The derivation and integration of Grassmann variables is defined in an algebraic way and has nothing to do with Riemann integral or measure theory. For a set of discrete independent Grassmann variables $\eta_1, ..., \eta_N, \bar{\eta}_1, ..., \bar{\eta}_N$ we have,

$$\frac{\partial}{\partial \eta_i}\eta_k = \delta_{ik}; \frac{\partial}{\partial \bar{\eta}_i}\bar{\eta}_k = \delta_{ik}$$

$$\frac{\partial}{\partial \eta_i}\bar{\eta}_k = 0; \frac{\partial}{\partial \bar{\eta}_i}\eta_k = 0$$

$$\frac{\partial}{\partial \eta_i}1 = 0; \frac{\partial}{\partial \bar{\eta}_i}1 = 0$$

And the rules for integration are isomorphic to those of derivation and are obtained by performing the substitutons:

$$\frac{\partial}{\partial \eta_i} \to \eta_i$$

$$\frac{\partial}{\partial \bar{\eta}_i} \to \bar{\eta}_i$$

An interesting property of Grassmann variables is that

$$\int_o \prod_x d\bar{\Psi}_x d\Psi_x \exp i \sum_{x,y} \bar{\Psi}_x A_{xy} \Psi_y = detA$$

whereas the gaussian integral with commuting variables (c-numbers) depends on $(detA)^{\frac{-1}{2}}$.

The Green funtions for Dirac fields are obtained by functional derivation in an analogous manner to that for bosons.

4.4 Path integral for gauge fields

The path integral for pure Yang-Mills theories cannot be defined in the naive way

$$\int DV_{i\mu} \exp i \int d^d x(\frac{-1}{4} F_{\mu\nu} F^{\mu\nu})$$

The result of this expression is infinite. Physically, it is easy to guess where the problem comes from; the theory presents gauge invariance, so if we integrate over A, we are summing many times over equivalent field configurations. The solution is to include a constraint (gauge fixing) and, at the same time, to preserve gauge invariance.

The trick which fulfills this two conditions was invented by Faddeev and Popov (Phys. Lett. 25B, 29. 1967). The proper path integral is

$\int DV_{i\mu} det(\frac{\delta C_i}{\delta \omega_j}) \exp i \int d^d x (L + L_{GF})$

where ω_j are the parameters of the gauge transformation, the conditions $C_i(V(x)) = 0, i = 1, ..., n^2 - 1$ are the gauge fixing conditions, L is the kinetic term for the gauge vector fields and

$L_{GF} = \frac{-1}{2\xi} \sum_i [C_i(V(x))]^2$

The determinant which appears in the integrand is called **Faddeev-Popov determinant**. The crucial point is that this determinant can be represented as an exponential, using the generalization for functional determinants of the property of gaussian integrals mentioned above. Introducing $2(n^2 - 1)$ auxiliary Grassmann variables we can write

$det(\frac{\delta C_i}{\delta \omega_j}) = \int d\bar{\eta}_k d\eta_k \exp \int d^d x L_{FP}$

$L_{FP} = \bar{\eta}_i M_{ik} \eta_k$ is the **Faddeev-Popov lagrangian density** and $M_{ik} = \frac{\delta C_i}{\delta \omega_k}$.

The auxiliary Grassmann variables have been artificially introduced in the theory and should disappear when calculating observable quantities. Actually, this is the situation and they are called **Faddeev-Popov ghosts**.

If we now want to write the generating functional for the full Yang-Mills theory, it reads

$Z[J, \bar{\xi}, \xi, \bar{\beta}, \beta] = \int_0 DV_{j\mu} D\bar{\Psi} D\Psi D\bar{\eta}_j D\eta_j$
$\exp i \int d^d x (L_{eff} + J^\mu_k V + \bar{\xi}\Psi + \bar{\Psi}\xi + \bar{\beta}\eta + \bar{\eta}\beta)$
$L_{eff} = L_{YM} + L_{GF} + L_{FP}$

Acknowledgments

I would like to thank Fred Jegerlehner and Mikhail Kalmykov for his support during my stay in DESY Zeuthen. My discussions with them have been absolutely essential to understand the topics summarized in this report.

I specially express my gratitude to Professor Jegerlehner, because he agreed to take me under his supervision as a Summer Student, giving me the chance to work not only in the field of Theoretical Physics, but on topics which were the natural continuation of my degree.

For the nice time I have had during the Summer Student Program, thanks to the rest of students, to Karl-Heinz Hiller and the staff at DESY Zeuthen.

References

[1] Fred Jegerlehner, *Electroweak theory and LEP Physics.* Lectures given in the Troisime Cycle de la Physique en Suisse Romande at the École Polytechnique Fédérale Laussane.

[2] Michael Peskin and Daniel V. Schoeder, *An introduction to Quantum Field Theory.* Addison-Wesley (1995).

[3] Steven Weinberg, *The Quantum Theory of Fields.* Cambridge University Press (1996).

Progress report on investigations on the PITZ quadrupoles and dipoles

Stephan von Coelln
hospitalstr. 100, 22767 hamburg, germany
e-mail: stephan_von_stephan@public.uni-hamburg.de

Theoretical and experimental investigations are performed on the dipole and quadrupoles for PITZ in order to determine the magnetic field distributions. The configuration of the experiment, the measurement performance and the hall probe measurements are described in the following.

1 A brief introduction to PITZ

A photo injector test facility is in the commissioning phase at DESY Zeuthen in order to optimize injectors for different applications like free electron lasers, production of flat beams for linear colliders and polarized electron sources. The experimental setup in the start up phase is shown in Fig. 1. A primary goal is the stable production of short electron bunches ($\approx 20\,\mathrm{ps}$) with a transverse emittance of $\approx 1\pi$ mm mrad at 1 nC and a small energy spread of about 1%.

2 The ray guiding components

In principle in accelerators electric fields are used to accelerate the particles whereas magnetic fields are used to bend and focus the beam. The main components of magnetic devices are solenoids, quadrupoles and dipoles, where solenoids are made up of magnetic dipoles, with the difference that the fields of solenoids are almost parallel to the beam with a gradient, whereas in dipoles the beam passes perpendicular to the field which is homogeneously in this case.
The solenoid at the PITZ is used to focus the beam right behing the electron source. In general solenoids are used to focus charged particle beam at low energies.
The dipole at the end of the setup is used to bend the beam in order to determine the momentum of the e^-.
The three quads are used to focus the beam at higher energies ($\tilde{1}$0MeV). A solenoid together with a quadrupole is also needed in order to produce flat beams, which is a important demand of TESLA. While the beam passes the solenoid, it received an angular momentum. In the quads this angular momentum can be used to produce the neededflat beam. With other quads the flat beam can be skewed in any direction in order to customize the beam to the measurent devices.

2.1 The dipole

The dipole consists of two coils, which produce a homogeneous magnet field perpendicular to the beam. The Lorentz-force

$$F_l = e(\vec{v} \times \vec{B})$$

bends the beam. It's easy to proof, that

$$\theta = \frac{LB}{(B\rho)} = \frac{LeB}{mv} \tag{1}$$

where L is the lenght of the dipole, B the magnetic field and m the electron mass. Hence from the measuring of the angle θ it is possible to obtain the momentum of the electrons.

2.2 The solenoids

In a solenoid the charged particles describe a spiral with decreasing radius in order to get the particles in the center of the soleniod, where the magnetic field is weaker than in a distance from the beam axis.

2.3 the quadrupole

The quadrupole magnet at PITZ is used to focus the electron bunches in order to provide the

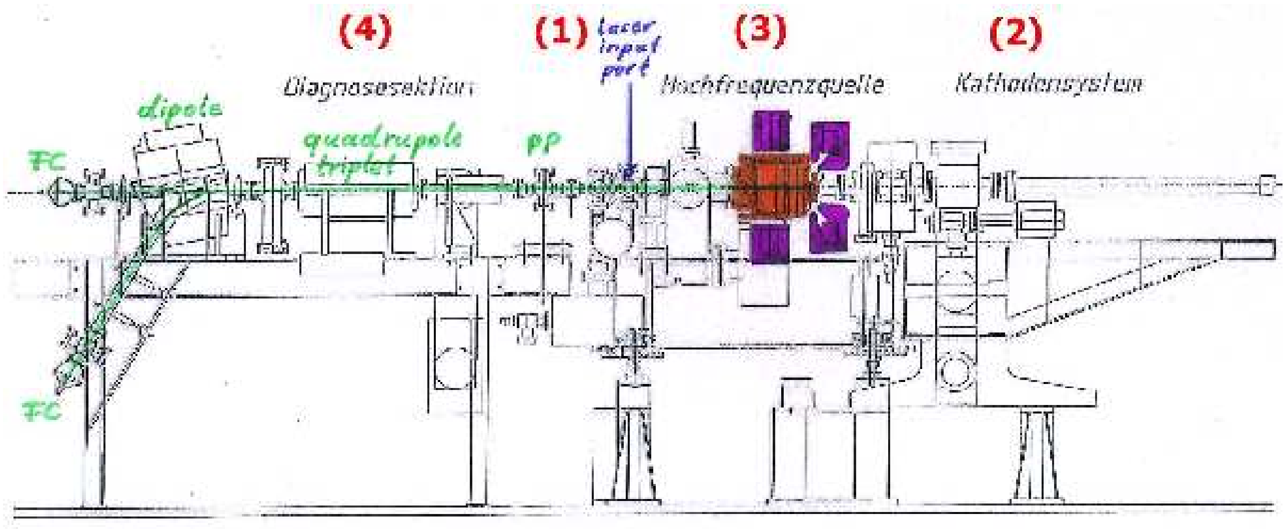

Fig. 1: *schematic view of the PITZ setup*

needed beam quality for use in the TESLA accelerator. Moreover it is used to produce flat beams in further investigations. The beam is passing trough a so called quadrupole triplet which consists of 3 magnetic quadrupoles.
The magnetic field of one quad can be described by:

$$\vec{B} = \frac{B_0}{r_0}(y\vec{e_x} + x\vec{e_y})$$

Now the electron is accelerated by the Lorentz-force:

$$F_l = e(\vec{v} \times \vec{B})$$

¿From this, one can derive the equations of motion. The differential equation for the moving of the electrons are independent for the x and y direction where z denotes the direction of the beam axis and $\ddot{x}$ is the second derivative $\frac{\delta^2}{\delta z^2}$ along z.

$$\ddot{x} = -\frac{x}{\lambda^2} \qquad \ddot{y} = \frac{y}{\lambda^2} \tag{2}$$

where $\lambda = \sqrt{\frac{pr}{qB_0}}$. The equations 2 can be solved with the ansatz of exponential functions plus initial values for x and $\dot{x}$. Because the effect of a quadrupole is dependent of the position x (or y) and $\dot{x}$ (or $\dot{y}$), its convenient to put it in vectors $\vec{x} = (x, \dot{x})$. Now the solutions to eq. 2 are:

$$J_{xab} = \begin{pmatrix} cos\theta & \lambda sin\theta \\ -\lambda^{-1 sin\theta} & cos\theta \end{pmatrix} \tag{3}$$

$$J_{yab} = \begin{pmatrix} cosh\theta & \lambda sinh\theta \\ \lambda^{-1} sinh\theta & cosh\theta \end{pmatrix} \tag{4}$$

with $\theta = \frac{L}{\lambda}$ where L is the lenght of the quad. J_{xab} and J_{yab} matrizes are the transfermatrizes for the quadrupole. There is to mention, that the upper right entry of the matrix describes the translation term of a beam without any lenses etc, whereas the lower left entry desribes the effect of a lense. If this entry is negative it results in a focusing effect and if it‘s negative it results in a defocusing effect. Hence this solutions 4 show that there is a focusing in one direction and a defocusing effect in the other direction. Similar to a lense system it‘s now possible to obtain a net-focusing effect, when two quads are set one after the other. If we put the matrizes (4) together in a 4×4 matrix like this:

$$J_{xy} = \begin{pmatrix} cos\theta & \lambda sin\theta & 0 & 0 \\ -\lambda^{-1} sin\theta & cos\theta & 0 & 0 \\ 0 & 0 & cosh\theta & \lambda sinh\theta \\ 0 & 0 & \lambda^{-1} sinh\theta & cosh\theta \end{pmatrix} \tag{5}$$

. If you have two quads one after another the net effect is given through the product of the two matrizes. If the second quad is 90 degrees turned against the first, one obtains what can be seen in equation (6)

The two entrys in eq. (6) which determine the focusing effect are negative, because θ is positive and smaller than one, so that the sinh and the sin terms are positive. Hence this arrangment of quads results in a net-focusing effect.
In our case, we deal with a quad-triplet where the first and the third quads are same in size and

field, where the second quad is twice as strong as the other one with a field which is orientated 90^o turned to the others. The proof of the focusing effect has to be done in the same manner, but its more difficult to see, cause the matrix has in principle to be decomposed in terms of translation and bending, so that one can see the minus at the right position. Here's a intuitive picture of what happens when the beam passes a quadrupole:

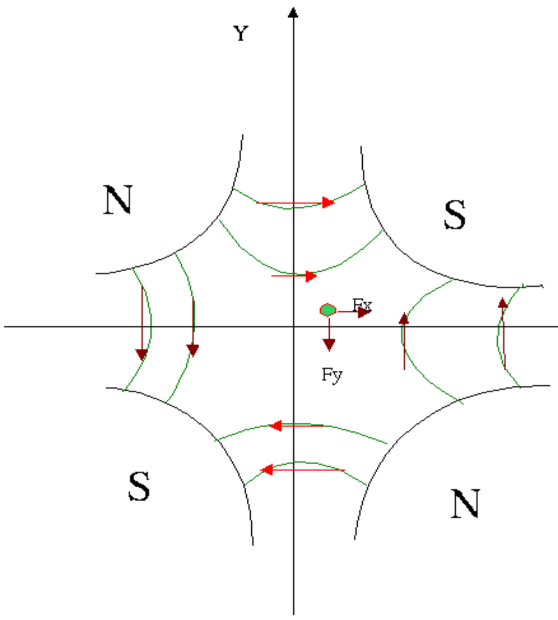

Fig. 2: *illustration of a electron passing a quadrupole field*

3 the issue

The quads have iron yokes inside. Because iron is a ferromagnetic material, it will keep a remantent magnetic field, even after the current is switched off. This feature of ferromagnetic materials is called hysteresis effect and is shown in the following figure (3)

After the magnetic induction H is decreased to zero, it can be seen that there remains a so called remanent field H_r. This magnetic field can be a problem for PITZ, whenever any influence on the e^- is not wished. The same problem appears with the dipole magnet at the end of the PITZ. A remaining field would bend the beam in a unwanted way.

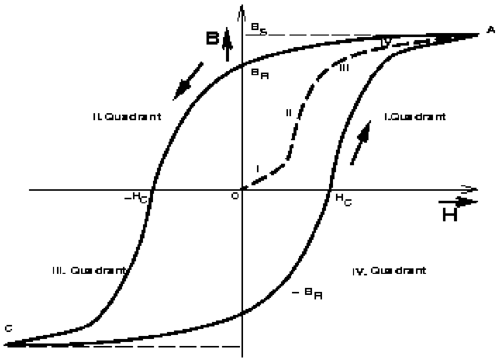

Fig. 3: *Hysteresis-plot of an ferromagnetic material*

3.1 the solution

The idea was to write a perl-script (or other language, but i chose perl) which applies an exponential damped cosine oszillated current on the magnets. This should decrease the remanace with each zerocrossing. This Perl script has to be implemented into the "DOOCS" environment, which is used to control and supervise the whole PITZ remote from the control room. The parameter, which can be changed are the cycle duration(T), the damping factor of the exponential function(invdamp), the start current (max) , and the current at which the routine ends (min). So the formula is this:

$$A(t) = start * e^{\frac{-t}{invdamp}} cos(\frac{2t\pi}{T})$$

At the end of this article you find a plot of the test run (4) and the two perlscripts for the quadrupole und for the dipole (4).

3.2 the measurements

In the test-phase it is measured the remanent magnetic field with a teslameter (a hall probe) with different parameters to optimize the script to obtain a optimum of degaussing in a reasonable time duration. The remanent field should be in the order of the earth magnetic field, which is about 0.05 mT. (time denotes the whole time to process the script, mag denotes the sign of the startcurrent(+/−))
Note: The given measurement errors are about 1% of the range, so it is about 0.02 mT. I chosed the position of the hallprobe so that the remanent field has a maximaum value. The results are shown in Tab(1) and Tab(2):

3.3 the results

Because the measurement exactness of the teslameter is just 0.02mT, and because there were two many parameters, which are perhaps not independent from eachother, it was not possible to find the best possible solution. Fortunately, the effect of chanageing the parameters was in a broad range almost independent of the parameters. Finally i have choosen parameters which should do the job good. In Tab(3) are the final parameters for both scripts.

Both scripts were implemented with the above given params into DOOCS. (contact person: Bert Schoeneich).

4 the iongetter-pump

The next task which i got after the quad-and dipole job was done, was to measure the magnetic field of a ion-getter pump with a permanent magnet, which would be later connected close to the beam pipe. My aim was to show the influence of this magnet-field on the beam. To do this i measured the magnetic field all around the pump on many position in many direction. After all, it turned out that the magnetic field close at the beam pipe would be neglegtible, at least as far the exactness of the measurements allow.

5 Conclusions

Both scripts for the quads and for the dipole decrease the remanent magnetic field very good. For the quads the field decreased from 0.33 mT to 0.03 mT and for the dipole the improofment was from 1mT to 0.1 mT. This is a reasonable result, cause in both cases the remanent measured field was in the order of the magnetic field of the earth (which is 0.03mT - 0.05mT) This is just valid for the positions at which i could measure the fields. Especially at the quads i could only measure at the edges without knowing the remanent field in the second quad. In case of insufficient measures this should be taken into consideration.
The iongetter pump measurements showed no measurable fields in a distance larger than 30 cm from the pump. Hence this field should be neglegtible.

Tab. 1: *the quad-measurements*

No	T	invdamp	start	min	time	mag	H
1	20	15	2.0	0.01	85	+	0.04
2	20	15	2	0.01	85	+	-0.1
3	20	15	2	0.01	85	+	0.01
4	20	15	2	0.01	85	-	-0.12
5	20	15	5	0.01	99	-	-0.05
6	20	15	4	0.01	95	-	-0.06
7	20	25	5	0.01	161	-	-0.02
8	20	35	5	0.01	223	+	-0.02
9	20	20	5	0.01	130	+	-0.01
10	20	20	5	0.01	130	-	-0.04
11	20	25	5	0.01	161	-	-0.05
12	20	12	5	0.01	80	-	-0.06
13	20	25	5	0.01	161	-	-0.05
14	12	15	5	0.01	99	-	-0.04
15	25	15	5	0.01	99	-	-0.05
16	25	25	5	0.01	161	-	-0.05
17	12	10	5	0.01	68	-	-0.05
18	12	10	5	0.01	68	+	-0.02
19	10	5	5	0.005	40	+	-0.04
20	15	15	5	0.005	109	+	-0.02
21	15	15	5	0.002	123	+	-0.02
22	15	15	5	0.005	109	-	-0.03
23	15	25	5	0.005	176	-	-0.03
24	15	18	4.5	0.005	126	-	-0.03
25	15	18	4.5	0.005	126	+	-0.02
26	15	18	4.5	0.01	114	+	-0.015
27	15	18	4.5	0.01	114	+	-0.03
28	12	18	4.5	0.01	114	-	-0.05
29	23	23	4.5	0.01	195	-	-0.03

Tab. 2: *the dipole measurements*

No	T	invdamp	start	min	time	mag	H
1	15	20	2.4	0.004	132	+	0.09
2	15	15	2.4	0.01	87	+	0.008
3	15	15	2.4	0.01	87	-	0.1
4	15	15	2.0	0.001	119	-	-0.09
5	22	22	2.0	0.005	136	-	0.09
6	22	22	2.0	0.005	136	+	0.11
7	15	25	2.2	0.005	139	+	0.1

$$J_{xy1}J_{xy2} = \begin{pmatrix} cosh\theta_2 cos\theta_1 & \lambda_1\lambda_2 sin\theta_1 sinh\theta 2 & 0 & 0 \\ -(\lambda_1\lambda_2)^{-1} sin\theta_1 sinh\theta_2 & cos\theta_1 cosh\theta_2 & 0 & 0 \\ 0 & 0 & cosh\theta_2 cos\theta_1 & \lambda_1\lambda_2 sin\theta_1 sinh\theta 2 \\ 0 & 0 & -(\lambda_1\lambda_2)^{-1} sin\theta_1 sinh\theta_2 & cosh\theta_2 cos\theta_1 \end{pmatrix} \quad (6)$$

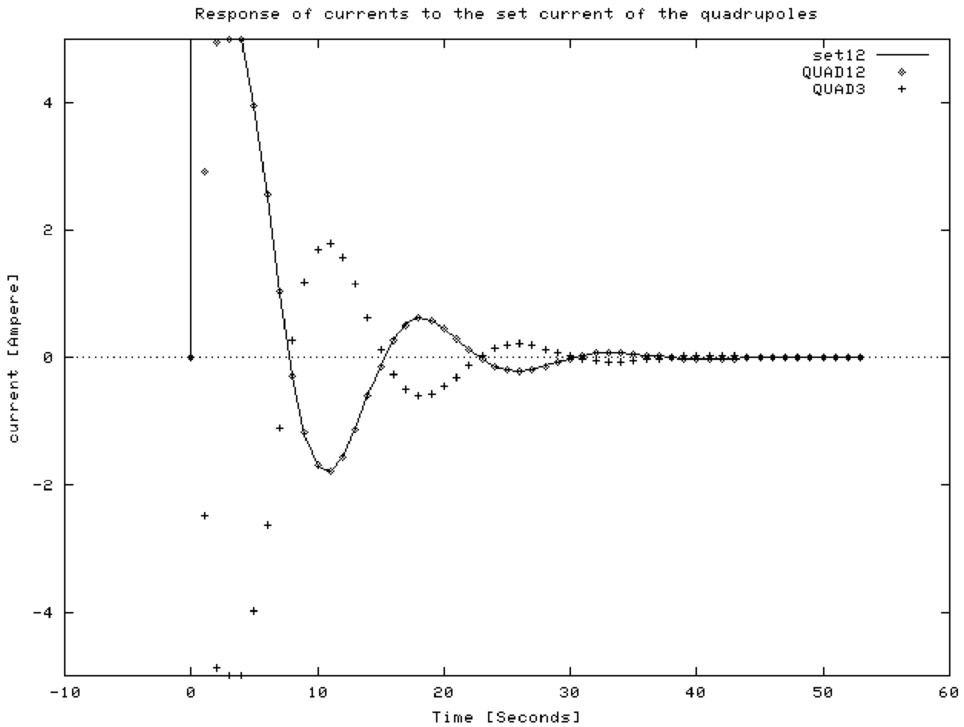

Fig. 4: *testrun of the script, applied on the 3 magnets of the quadrupole*

Tab. 3: *the final params*

-	T	invdamp	start	min	time	H
quads	15	18	4.5	0.01	114	-0.022
dipole	15	25	2.2	0.005	139	0.1

The quadrupole script

```
#! /usr/bin/perl
# This script is made to remove the remanent magnetic field from the quadrupol triplet in the ”PITZ”
# by S.v.Coelln , made during the summerstudentprogramm 2002 at the DESY Zeuthen

# [PART 1] - list of params
$T=15; # time of one periode in seconds
$min=0.01 ; # value when the mainloops ends (Ampere)
$startcurrent=4.5 ; # current which to start with (Ampere)
$invdamp=18 ;  inverse damp factor for the exp-function (increasing this results in decreasing damp)

$pi=3.1413 ;

# [PART 2] - Calculation of the whole time which is needed to process the script
$zeit=-$invdamp*log($min/$startcurrent) ;
print 'Processing time:'.(int($zeit)+5).”” ; # 4 seconds of sleep plus 1 sec for rounding integer = 6

$testcurrent=startcurrent;

# [PART 3] - setting the startcurrents for the Quads
system ”doocsput -c PITZ.MAGNETS/QUAD12/PS5/SETPOINT -t 2 -d $startcurrent” ; # set the
current for QUAD12
system ”doocsput -c PITZ.MAGNETS/QUAD3/PS6/SETPOINT -t 2 -d -$startcurrent” ; #set the
current for QUAD3
system ”sleep 3” ;# give time for reaching stationary state

# [PART 4] - the main loop
for($i=0 ; $testcurrent¿$min ; $i++)
{
$testcurrent=$startcurrent*exp(-$i/$invdamp) ; #just the damped term which is used for aborting loop
$current=$testcurrent*cos(2*pi*i/T); #valuesofthedampedcosineoszilation
$quad3curr = −$current;
system”doocsput − cPITZ.MAGNETS/QUAD12/PS5/SETPOINT − t2 − d$current”;
system”doocsput − cPITZ.MAGNETS/QUAD3/PS6/SETPOINT − t2 −
d$quad3curr”; #currentofQUAD3settominuscurrentQUAD12
system”sleep1”;
}

# [PART 5] - decrease the current to the minus ten'th of the last value
$endcurrent=-0.5*($current) ;
$endquad3curr=-$endcurrent ;
system ”doocsput -c PITZ.MAGNETS/QUAD12/PS5/SETPOINT -t 2 -d $endcurrent” ;
system ”doocsput -c PITZ.MAGNETS/QUAD3/PS6/SETPOINT -t 2 -d $endquad3curr” ;
system ”sleep 1” ;

# Set current to zero
system ”doocsput -c PITZ.MAGNETS/QUAD12/PS5/SETPOINT -t 2 -d 0” ;
system ”doocsput -c PITZ.MAGNETS/QUAD3/PS6/SETPOINT -t 2 -d 0” ;
```

The dipole Script

```
#! /usr/bin/perl
# This script is made to remove the remanent magnetic field from the dipole magnet at the "PITZ"
# by S.v.Coelln , made during the summerstudentprogramm 2002 at the DESY Zeuthen
# [PART 1] - list of params

$T=15 ; # time of one periode in seconds
$min=0.005 ;  value when the mainloops ends (Ampere)
$startcurrent=2.2 ; # current which to start with (Ampere)
$invdamp=25 ; # inverse damp factor for the exp-function (increasing this results in decreasing damp)

$pi=3.1413 ;

# [PART 2] - Calculation of the whole time which is needed to process the script
$zeit=-$invdamp*log($min/$startcurrent) ;
print 'Processing time:'.(int($zeit)+5)."" ; # 5 seconds of sleep plus 1 sec for rounding integer = 6

$testcurrent=$startcurrent ;

# [PART 3] - setting the startcurrents for the Quads
system "doocsput -c PITZ.MAGNETS/DIPOLE/PS9/SETPOINT -t 2 -d $startcurrent" ; # set the
current for the dipole
system "sleep 3" ; # give time for reaching stationary state

# [PART 4] - the main loop
for($i=0 ; $testcurrent¿$min ; $i++)
{
$testcurrent=$startcurrent*exp(-$i/$invdamp) ; #just the damped term which is used for aborting loop
$current=$testcurrent*cos(2*$pi*$i/$T);  values of the damped cosine oszilation
system "doocsput -c PITZ.MAGNETS/DIPOLE/PS9/SETPOINT -t 2 -d $current" ;
system "sleep 1" ;
}

# [PART 5] - decrease the current to the minus ten'th of the last value
$endcurrent=-0.5*($current) ;
system "doocsput -c PITZ.MAGNETS/DIPOLE/PS9/SETPOINT -t 2 -d $endcurrent" ;
system "sleep 1" ;

# Set current to zero
system "doocsput -c PITZ.MAGNETS/DIPOLE/PS9/SETPOINT -t 2 -d 0" ;
```

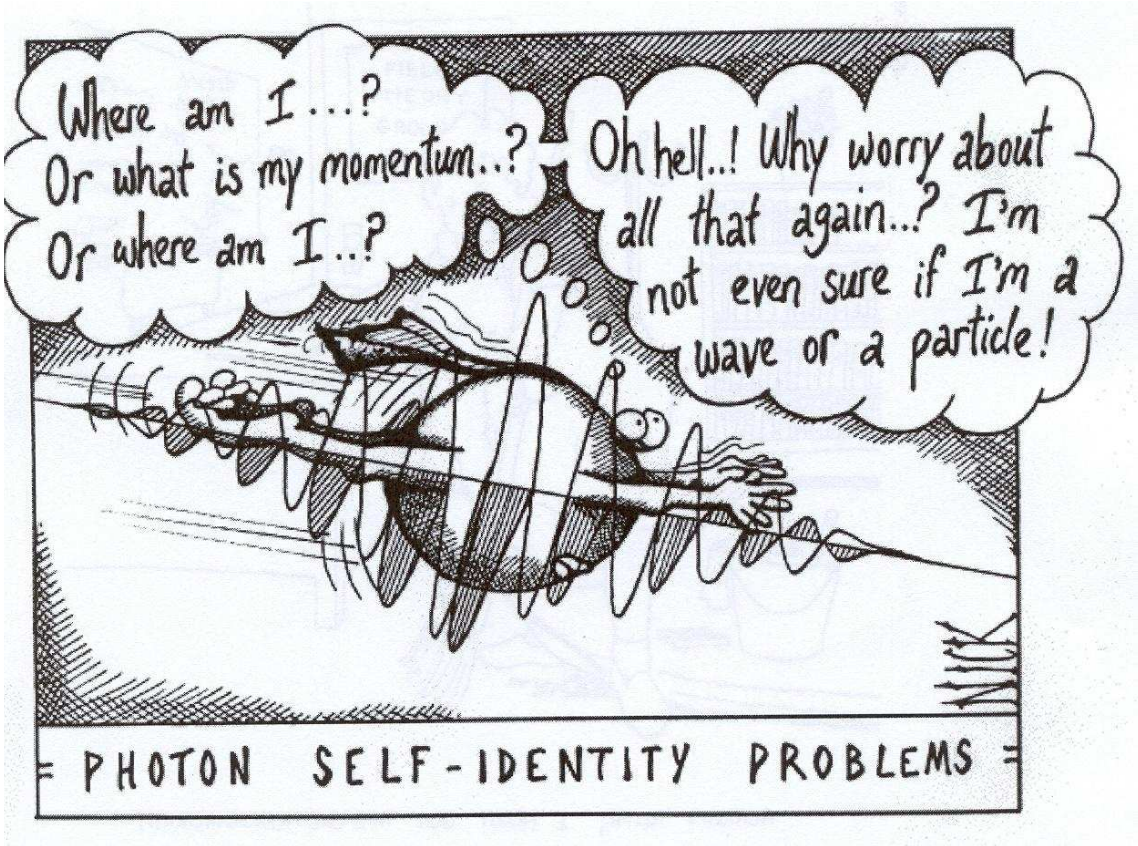
Where am I...? Or what is my momentum..? Or where am I..?
Oh hell..! Why worry about all that again..? I'm not even sure if I'm a wave or a particle!
PHOTON SELF-IDENTITY PROBLEMS

Production of heavy uncharged MSSM Higgs Bosons with $\gamma\gamma$ collisions in $b\bar{b}$ final states

Jens Dittrich
BTU Cottbus - Technical University of Cottbus
Universitätsplatz 5
03046 Cottbus
Email: dittrje@tu-cottbus.de

We studied the production of heavy Higgs Bosons H, A in high energy collisions of polarised Photons. Aspects of the different polarisation states in the $b\bar{b}$ final state are studied. It turned out, in one polarisation state the Higgs production is possible and additionally the background is very surpressed. Further we could obtain a characteristic angular distribution of the background process compared to the signal and further characteristic properties to differentiate between signal and background. Due to this and other properties we can suggest several cuts in the produced histograms to increase the significance of the signal.
Key words: Higgs Bosons; Supersymmetry; Photon collider; polarised Photon; Bottom final states

1 Introduction

The Higgs Bosons are required by the Standard-Model and supersymmetric extensions of it. The minimal supersymmetric extension (MSSM) contains two isospin doublets of the Higgs field. After electroweak symmetry breaking we get five elementary Higgs particles [1]: two neutral CP-even (h,H), one neutral odd (A) and two charged ($H^{\pm}$). In our studies we are limited to the uncharged states H and A, which are produced in high energetic $\gamma\gamma$ collisions.

We considered a future linear e^+e^- collider, which can use each bunch for collision only once. Due to this fact, it is possible to polarise the electrons up to nearly 80%. Next to the interaction point we used a long wave length Laser to produce high energetic photons through compton scattering. We assumed here no non linear effects. Due to the polarisation of the incoming electrons and photons one gets also polarised photons.

We declared the most frequently produced state as $+$ state, the other one as $-$ state. Because we collided two photons, we got 4 helicity states: $++$, $+-$, $-+$ and $--$, where two of them ($+-$, $-+$) lead to an equal distribution.

The process in $b\bar{b}$ final states seems to be the most interesting one, because you get a very surpressed background in the helicity state, forced for production of a Higgs particle. We differentiate the two helicity states $J = 0$ and $J = \pm 2$ which corresponds to the $++$ and $+-$ polarisation states of the incoming photons. The helicity state corresponding to $--$ polarisation states can be neglected.

We calculated the cross section for the background process in $++$ helicity mode with an external program at a fixed energy [2]. Due to this fact we had to normalize the calculated cross section in an energy window of ± 3 GeV coming from the energy resolution of the detector. Here we recognized the cross section is surpressed by a factor of 100 compared to the cross section coming from $+-$ helicity state. Anyway in the $--$ helicity channel, there are nearly no photons produced in the interesting energy region which could create more background.

In further analysis we used the program PYTHIA to generate the signal and background events and to fill the interesting properties in a histogram. Additionally we also used the program SIMDET which simulates the detector. There we applied different cuts to produce a signal with more significance. It turned out that an energy and an angle cut are the most effictive ones. Anyway there are other cuts to apply, too, which increases the significance.

For the signal we set up the beam energy in such a way, that the Higgs mass is equal to the energy of the highest peak in the interesting helicity channel. On the other hand the signal has a delta distribution like behavior. So it is no restriction of the generality to produce the Higgs particles only in an ± 3 GeV window around the highest peak, which is adapted to this mass.

2 Normalizing the cross section of the background

2.1 *Calculating the luminosity of $\gamma\gamma$*

The high energetic photons are produced by Compton scattering with the long wave length Laser. If you assume no non linear effects such as an interaction of an electron with two photons or interactions of low energetic electrons, you can get an explicit expression of the compton energy spectrum of the photons which is given in [3, Fig. 1]. The abscissa denotes the fraction of the photon energy compared to the energy of the electron beam. Due to cinematic reasons we cut off the spectrum at $y_{max} = \frac{x}{x+1}$ with the parameter x, which is set to the value $x = 4.8$. This constant is representing the experimentation arrangement and the adjusted value is in the region of the most powerful solid state lasers.

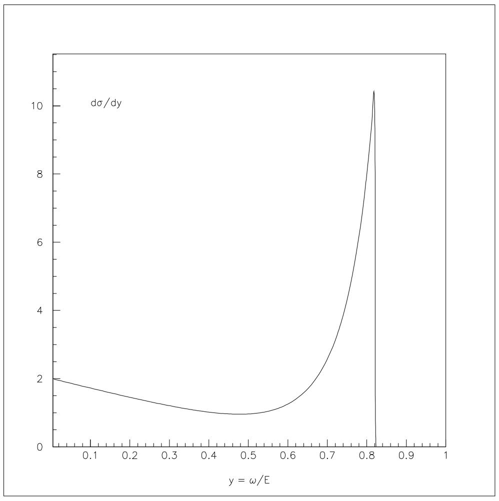

Fig. 1: *Spectrum of the compton scattered photons in terms of fraction of center of mass energy.*

Further we calculated the $\gamma\gamma$ luminosity in the following way with respect to the divergencies of the energy spectra:

$$\frac{\partial\mathcal{L}}{\partial z} = \int_0^{y_{max}}\int_0^{y_{max}} E_1(y_1)E_2(y_2) \,,\quad \delta(\sqrt{y_1y_2} - \frac{\sqrt{s}}{2E_b})\,dy_1\,dy_2$$

where E_1 and E_2 are the energy spectra of the scattered photons which depend also on the parameter x and E_b is the fixed energy of the incoming electron or positron. Due to 4-momentum conservation law we got the δ-distribution expression. Using a property of the delta distribution and respecting the divergencies, we got:

$$\frac{\partial\mathcal{L}}{\partial z} = \int_{y_{min}}^{y_{max}} \frac{E_1(y)E_2(\frac{s}{4E_b^2}\frac{1}{y})}{y}\frac{\sqrt{s}}{E_b}\,dy \;,$$

where now y_{max} is defined like above and $y_{min} = \frac{x+1}{x}\frac{s}{4E_b^2}$, So that integral is well-defined and convergent (Fig. 2). We denote that z is the fraction of the energy of an event compared to center of mass energy.

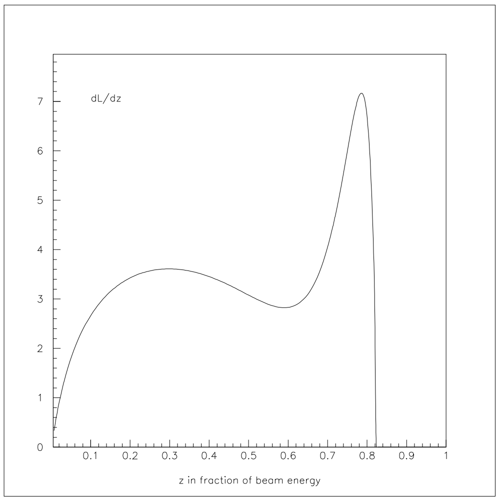

Fig. 2: *$\gamma\gamma$ differential luminosity distributions in terms of fraction of center of mass energy.*

To add polarisation states E_i turns into too $E_i\frac{1\pm\lambda_\gamma}{2}$, where $\pm$ denotes the $+$ or $-$ polarisation state and λ_γ is the average helicity of the photons. In the end we got different differential luminosity distributions (Fig. 3 - 5). You can easily see, that the $--$ polarisation state is very reduced at the interesting energies, so it can be neglected.

Further one can determine the $++$ helicity distribution has a peak near the maximum energy. Later we are going to calculate the corresponding beam energy of this peak and setting

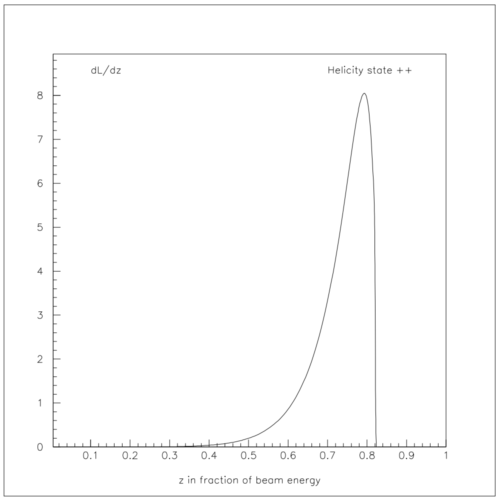

Fig. 3: $\gamma\gamma$ *differential luminosity distributions in terms of fraction of center of mass energy for two + helicity photons.*

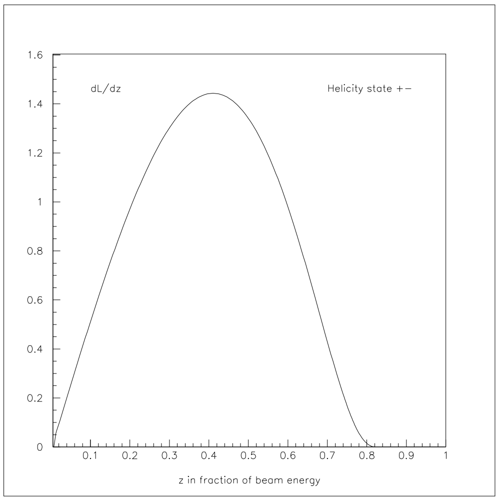

Fig. 4: $\gamma\gamma$ *differential luminosity distributions in terms of fraction of center of mass energy for one + and one + helicity photon.*

up the event generator to this energy for producing some Higgses with the peak mass.

2.2 Normalization of the cross section

We wanted to reproduce the data from [4]. There they run at an energy window of ±3 GeV. That is why we had to normalize the calculated cross section. We simply integrated over this energy window as follows: We could constate the number of events is equal to $N = \int_{y'}^{y''} \frac{\partial \mathcal{L}}{\partial y}\sigma(y)\, dy$ and the average luminosity $\langle \mathcal{L} \rangle = \int_{y_{min}}^{y_{max}} \frac{\partial \mathcal{L}}{\partial y}\, dy$. So due to the definition of luminosity we get for the average cross section $\langle \sigma \rangle = \frac{N}{\langle \mathcal{L} \rangle}$. Combining all three, we could calculate the normalisation factor:

$$\langle \sigma(x) \rangle = \frac{\int_{y'}^{y''} \frac{\partial \mathcal{L}}{\partial y}\sigma(y)\, dy}{\int_{y_{min}}^{y_{max}} \frac{\partial \mathcal{L}}{\partial y}\, dy},$$

where $y' = \frac{E_0 - 3GeV}{2E_b}$, $y'' = \frac{E_0 + 3GeV}{2E_b}$ are defined, $E_0 = xE_b$ is the interesting energy corresponding to x, y_{min} and y_{max} are defined as above. Further we assumed $\sigma(y) = const$ in this short given intervall. Combining the calculated luminosity and the normalisation factor $\langle \sigma(x) \rangle$ we got the luminosity distribution from Fig. 6.

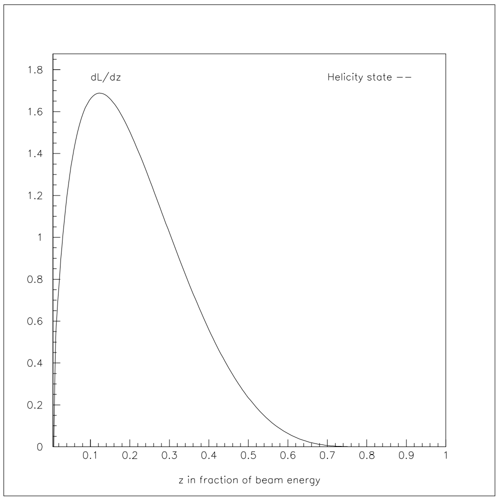

Fig. 5: $\gamma\gamma$ *differential luminosity distributions in terms of fraction of center of mass energy for two − helicity photons.*

3 Work with Pythia

3.1 Fixed Energy and cluster algorithms

It is very easy to run PYTHIA with fixed energy, you should follow the example in the manual. We also observed a bug in the PYGIVE function, which forbids to use character strings with more than 12 characters, when you want to fill an integer value.

For clustering we used an scaled JADE-Algorithm: You add two particles i and j to one jet, if the following estimation is fulfilled:
$(p_i + p_j)^2 = p_i^2 + 2\langle p_i | p_j \rangle + p_j^2 \geq 2\langle p_i | p_j \rangle$.

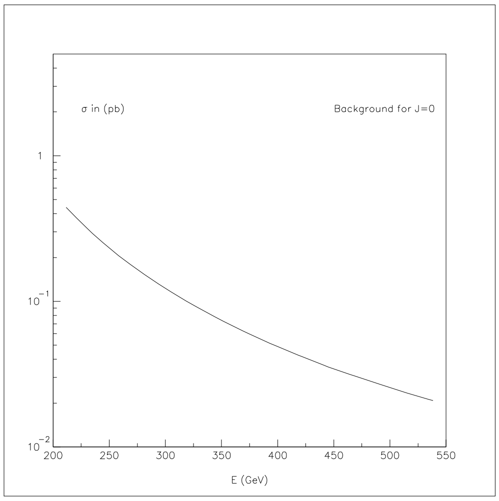

Fig. 6: *cross section for the background process $\gamma\gamma \to b\bar{b}$ in J=0 state.*

Due to cinematic reasons one can neglect the mass terms. And so, we get: $\langle p_i | p_j \rangle \leq y_{cut} s$. You do this for each combination of i and j as long as no combination fullfills the inequation.

One can specify the minimum number of jets in PYTHIA. If you additionally increase the y_{cut} to an unbelievable high value like 1.0 you get exactly the specified number of jets. In further steps we examined, whether the jets have a direction similar to their origin, the b-quarks. And in fact it works, even if you take away the neutrinos from the calculation of the jets because we cannot detect them. We have also seen PYTHIA is able to reproduce the angular distribution as expected for the background with an amassment in the direction of the beampipe.

3.2 Variable Energies

We wanted to run PYTHIA with a variable energy under a given spectrum of the photons for each beam. In the first attempt we could examine the pseudo random numbers produced by Fortran are evenly distributed. So it was easy to produce the random numbers following the spectra $f(x)$. First we normalized the $\int_0^{y_{max}} f(y)\,dy$, than we produced a random number $p \in [0,1]$ and calculated the x value which corresponds to $\int_0^x f(y)\,dy \stackrel{!}{=} p$, this gave us the proper distribution of random numbers. It works very fine, because the spectra are positive definite and so the integral as a function of its upper boundary is strictly monotonous increasing. For the signal process we considered the peak of the differential luminosity by a numerical way, and set up the beam energy exactly up to the corresponding value of the peak. Anyway we used here again an energy window of ± 3 GeV. It is a proper way of doing, because the Higgs has a very sharp and high delta-like peak.

4 Future Tasks

In future we have to normalize our data to the background signal due to the energy resolution of ± 3 GeV. Further we have to choose proper parameters of the detector. Today it seems to be a good idea to cut lower angles of the jets, because in most cases the background is emmitted nearly collinear to the beam pipe. On the other hand the Higgs is a scalar particle and it has no preffered direction of decay.

Acknowledgments

I want to thank Klaus Mönig, Aura M. Rosca and Achim Stahl for the fruitful collaboration in this project. Further I want to send a special thank to Wolfgang Lohmann and Achim Stahl, who invited me to the summer student program.

Another special thank goes to all the summer students who made the time here more variedly and helped each other very much.

References

[1] J.F. Gunion and H.E. Haber, Nucl. Phys. B272 (1986) 1 and B278 (1986) 449.

[2] G. Jikia and A. Tkabladze. Phys. Rev., D54:2030-2042, 1996, hep-ph/9601384

[3] TESLA - Technical Design Report, Part VI - Appendix, March 2001.

[4] M.M. Mühlleitner - Production of MSSM Higgs Bosons in $\gamma\gamma$ Collisions hep-ph/0101177.

Multiple Scattering of a π^- beam in the HERA-B detector.

Antonios Garas
Aristotle University of Thessaloniki
Department of Physics
Thessaloniki, Greece.
Email: agara@skiathos.physics.auth.gr

We study the effect of multiple scattering to a simulated 1 GeV beam of π^- using GEANT. The results are compared with the theoretical prediction according to Molière theory of multiple scattering.

1 Introduction

When a charged particle traversing ordinary matter, it is deflected by many small-angle scatters. Most of this deviation is due to Coulomb scattering from nuclei, and also to a lesser degree to the electron field, hence the effect is called multiple Coulomb scattering.

At least four different theories of the multiple scattering of electrons by atoms have been published by Molière [1][2], Snyder and Scott [3][4], Goudsmit and Saunderson [5], and Lewis [6], which are mathematically closely related, and which can give exact results if carefully evaluated. The first two use immediately the approximation of small scattering angles and therefore an expansion in Bessel functions. Goudsmit and Saunderson developed a theory valid for any angle by means of an expansion in Legendre polynomials. Lewis starts from the Legendre expansion and then goes over to the limit of small angles, thus establishing the connection between the first three methods.

In Molière theory, the Coulomb scattering distribution is roughly Gaussian for small deviation angles, but at larger angles (greater than a few θ_0, defined below) it behaves like Rutherford scattering, having larger tails than does a Gaussian distribution.

If we define the *spatial angle*, θ_{space}, as the difference between the angle in which the particle enters and exits the material, and the projection of this angle to a plane as θ_{plane}, then we can also define θ_0 as the r.m.s. of the angle between the directions projected on a plane of a particle before and after traversing a thickness x of a volume. θ_0 is related to θ_{space}^{rms} according to the equation:

$$\theta_0 = \theta_{plane}^{rms} = \frac{1}{\sqrt{2}}\,\theta_{space}^{rms}. \qquad (1)$$

It is sufficient for many applications to use a Gaussian approximation for the central 98% of the projected angular distribution, with a width given by [7][8]

$$\theta_0 = \frac{13.6MeV}{\beta cp} z\sqrt{x/X_0}\left[1 + 0.038ln\left(x/X_0\right)\right]. \qquad (2)$$

Here p, β c, and z are the momentum, velocity and charge number of the incident particle, and x/X_0 is the thickness of the scattering medium in radiation lengths[1]. This value of θ_0 is from a fit to Molière distribution [1][2] for single charged particles with $\beta = 1$ for all Z, and is accurate to 11% or better for $10^{-3} < x/X_0 < 100$.

Lynch and Dahl have extended this phenomenological approach, fitting Gaussian distributions to a variable fraction of the Molière distribution for arbitary scatterers [8], and achieve accuracies of 2% or better.

In our analysis we used a simulated beam of 1 GeV π^- traversing the volume of HERA-B detector using GEANT [9] Monte Carlo program. Our goal was to study the limits where formula

[1] In dealing with charged particles at high energies, it is convenient to measure the thickness of the material in units of the radiation length X_0. This is the mean distance over which a high-energy electron loses all but $1/e$ of its energy by bremsstrahlung.

(2) gives accurate results and can be used to describe multiple scattering.

2 The HERA-B detector

HERA-B [10] is an experiment originally proposed to study CP violation in the B system using an internal target at the HERA proton ring.

The HERA-B detector is a large aperture forward spectrometer (Fig. 1) with a geometrical acceptance between 0.01< θ <0.22 & 0 < ϕ < 6.28 [rads]. In GEANT [9] the detector is described by more than 30,000 volumes.

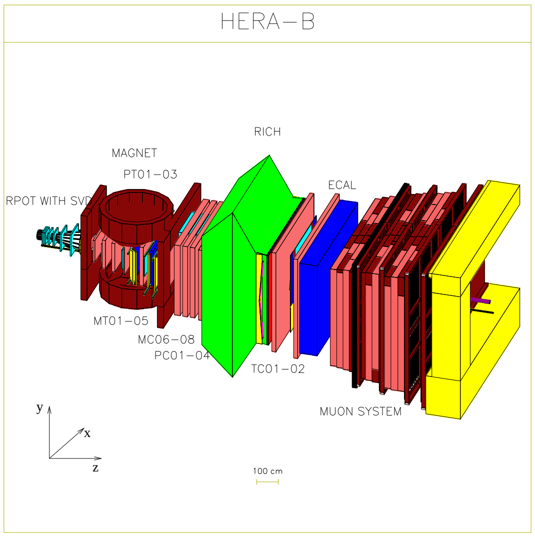

Fig. 1: *Overview of the HERA-B detector.*

In Fig. 1 one can see an overview of the HERA-B detector. The basic parts of the detector are listed below.

- **The Vertex Detector System**

  The Vertex Detector System (VDS) is defined for:

  - Primary vertex reconstruction.
  - Secondary vertex reconstruction.
  - Determination of impact parameters for tracks associated with tagging particles.

- **The Magnet**

  The HERA-B spectometer magnet is a normal-conducting dipole which provides a field integral of 2.2 mT. An integral part of the magnet system is the compensation coil which shields the electron beam so that the lepton beam may pass through HERA-B spectometer undeflected.

- **The Main Tracker**

  The particle flux which passes through the spectometer has a larger value near the beam pipe, decreasing as $\approx 1/r^2$ moving out from the beam pipe. The implications for the main tracker are that the inner region must have a segmentation which is fine enough not to be overwhelmed by the higher occupancy. As a result, the main tracker is divided into two tracking systems, the Inner Tracker and the Outer Tracker.

  The main tracker is also logically divided into three regions, labeled the TC, PC, and MC. The TC region is the area immediately downstream of the RICH, and prior to the ECAL. The PC region begins immediately downstream of the magnet and ends at the RICH and the MC region is the area inside of the magnet.

  - **The Inner Tracker** (ITR)

    The ITR consists of 10 stations of GEM MSGC (**G**as **E**lectron **M**ultiplier / **M**icro **S**trip **G**ass **C**hambers) detectors, with 184 detectors in total, each having 768 anode strips.

  - **The Outer Tracker** (OTR)

    The OTR utilizes honeycomb drift chambers as the basic unit of construction, formed from a gold/copper coated folded pokalon foil. Two different cell sizes, 5 mm and 10 mm are used, with the smaller cell size occupying the inner region of higher flux, and the 10 mm cells used in the outermost layers.

- **The RICH detector**

  The elements of the RICH detector are:

  - the C_4F_{10} gas radiator where Čerenkov photons are produced by charged particles.

– the two spherical mirrors which project Čerenkov photons to form rings on the focal surface,
– two planar mirrors which reflect the focal surface to above and below the spectometer,
– the photon detector in the focal surface
– the readout system

- **The Transition Radiation Detector** (TRD)

  The TRD is intended to complement the ECAL in the task of identifying electrons. The primary goal of this subdetector is to efficiently separate electrons from hadrons in the innermost region, where the track multiplicity is highest.

- **The Electromagnetic Calorimeter** (ECAL) The ECAL is responsible for providing the electron pretrigger signals that initiate the first level trigger algorithm.

- **The Muon Detector** The muon detector provides the muon pretrigger signals to the first level triger, as well as the information necessary for the reconstruction of muon tracks.

3 Results using only multiple scattering

In GEANT [9], one can choose which physical processes he wants to use for the simulation. We started our simulation by using only multiple scattering so to have a clear view of the difference between the results for the case we used Gaussian multiple scattering and the case we used Molière multiple scattering.

3.1 Molière multiple scattering

We will present here our results for the case the only physical process active was Molière multiple scattering. Fig. 2 is a scatter plot which shows the angular distribution (θ_{plane}) on the xz plane (the coordinate system that we use is shown in Fig. 1), versus the thickness of the material in radiation length. Here we have to say that the units we use in our simulation for the angles are [rad].

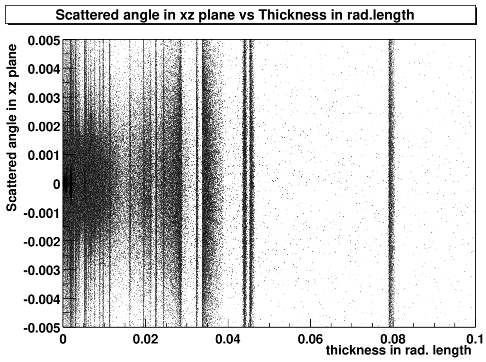

Fig. 2: *The θ_{plane} angle distribution vs thickness in rad. length.*

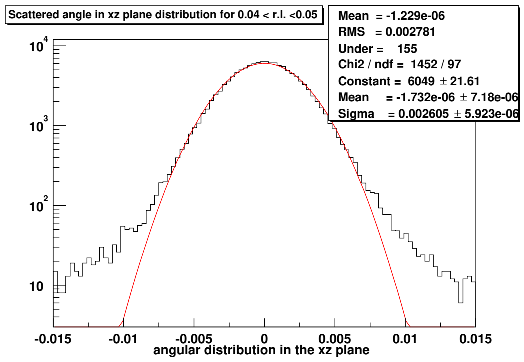

Fig. 3: *The θ_{plane} angular distribution in the x-z plane for Molière multiple scattering*

In Fig. 2 we can clearly see that geometrical volumes of the detector with specific thickness give almost all the possible angular values which corresponds to well formed lines.

Analyzing the angular distribution for a given thickness (Fig. 3) we can clearly see that it has larger tails than a Gaussian. This is the main difference between the angular distribution according to Molière and Gauss multiple scattering.

One way to study how accurate we can describe Molière multiple scattering using formula (2) is to compare the sigmas of the gaussian fit of formula (2) over some angular distributions like the one in Fig. 3, with the value obtained from formula (2). The result shown in Fig. 4 is in good agreement with the theory.

A second way to study the same thing is to take the profile histogram (the mean values) of the spatial angle distribution and compare it with the expected results of formula (2), multiplyied by $\sqrt{2}$ according to definitions of the spatial angle (Eq. (1)). We can see that the mean values plot (Fig. 5) gives bigger mean values for very thin materials than it is expected and it does not give zero.

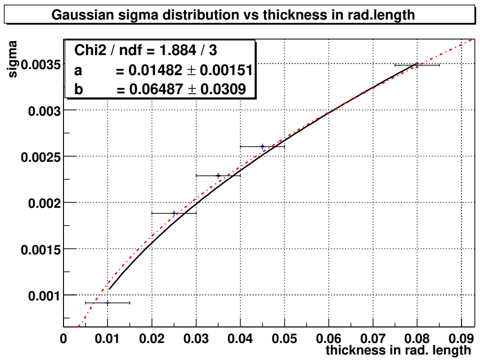

Fig. 4: *Gaussian sigmas vs thickness in rad. length. The dotted line is a plot of the formula (2), and the solid line is the fitted one.*

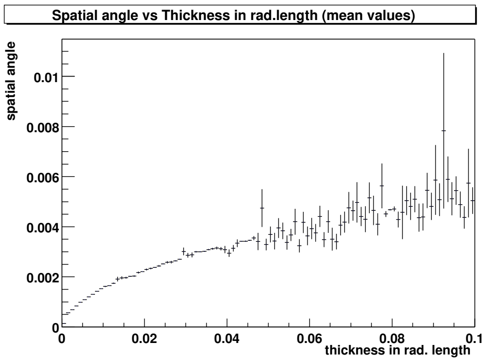

Fig. 5: *The θ_{space}^{rms} angular distribution vs thickness in rad. length.*

As a pointer to study this deviation we can use the χ^2 distribution (Fig 7) as it is given by the formula:

$$\chi^2 = \frac{(\chi_{exp} - \chi_{th})^2}{err^2} \tag{3}$$

In formula (3), χ_{exp} is the mean angular value we obtained from the simulation (Fig 5), χ_{th} is the angular value we expect according to formula (2) and *err* is the error for the χ_{exp} value.

In Fig. 6, we can see that for the region of thickness, in units of radiation length, > 0.01 we have a very good agreement and almost all the deviations from the expected values are inside the error bars.

So if we exclude the region of thickness < 0.01 which gives big deviation, and make a fit over the the mean values of the angular distribution

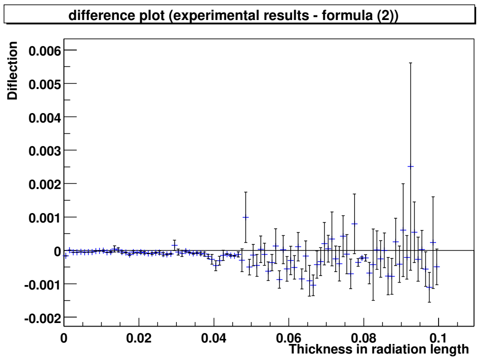

Fig. 6: *The θ_{space}^{rms} angular deviation vs thickness in radiation lengths.*

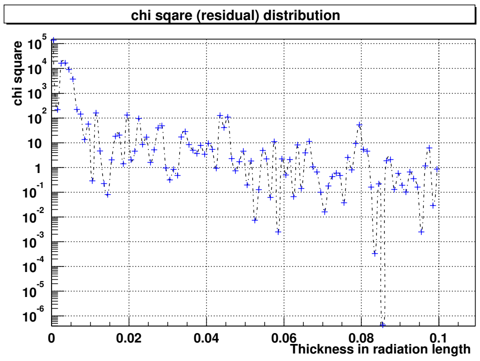

Fig. 7: *The χ^2 distribution vs thickness in radiation lengths.*

(Fig. 8), to the fotmula:

$$\theta_{space}^{rms} = \sqrt{2}\theta_0 = \alpha\sqrt{x/X_0}\left[1 + \beta ln\left(x/X_0\right)\right]. \tag{4}$$

we can verify again, that there is a good agreement with the formula (2).

3.2 Gaussian multiple scattering

After we discussed the results from our simulation, using only multiple scattering according Molière theory, we will see now the results obtained using the same procedure for the case that the only physical process active in GEANT [9] is Gaussian multiple scattering.

The purpose for this analysis is to compare the results and to see the difference between the two kinds of multiple scattering.

Comparing Fig. 9 and Fig. 3 We can see the main difference between Gaussian and Molière multiple scattering, which is, as we already mentioned above, that the θ_{plane} angular distribution for Molière theory gives larger tails.

Furthermore one can see from the Figures 10

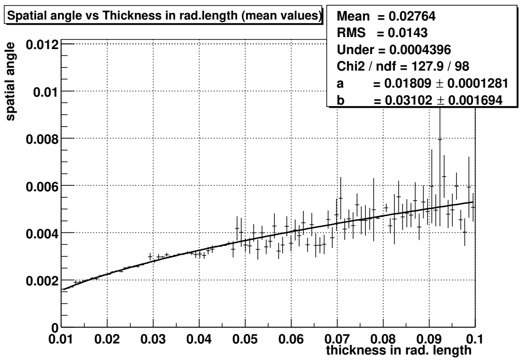

Fig. 8: *The θ^{rms}_{space} angular distribution vs thickness in rad. length and the fitted curve over this values.*

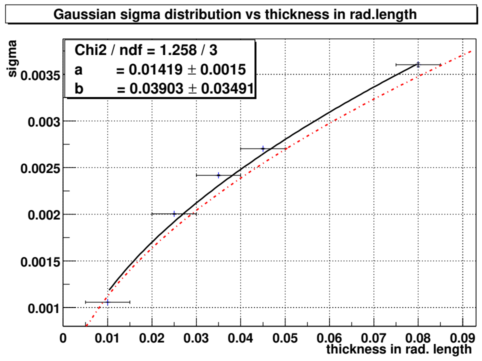

Fig. 10: *Gaussian sigmas vs thickness in rad. length. The dotted line with is a plot of the formula (2), and the solid line is the fitted one.*

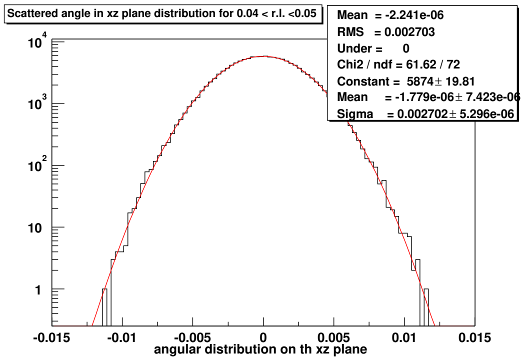

Fig. 9: *The θ_{plane} angular distribution in the x-z plane for Gaussian multiple scattering*

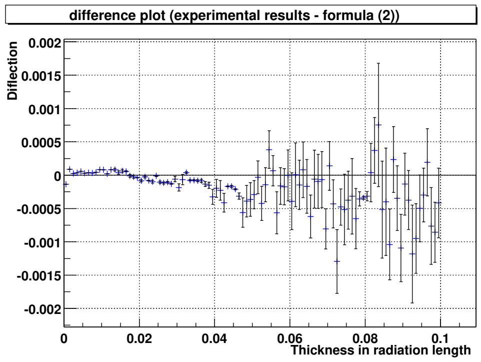

Fig. 11: *The θ^{rms}_{space} angular deviation vs thickness in radiation lengths, for Gaussian multiple scattering.*

and 13, that Gaussian multiple scattering is also well described by formula (2). But as we can see from Fig. 11 and Fig. 12 the region of thickness in radiation lengths which we have to exclude from our fit because of the deviation, is larger than the region for the case of Molière multiple scattering (now we have to exclude the region with thickness $<$ 0.02 cm), and the deviation itself is bigger.

3.3 Results including all physical processes

In this section we show the results that we produced following the same analysis as we described above, for the case of Molière multiple scattering with all the other physical processes active. We just want to see if there are any big differences between these results and the results we discused in section *3.1*.

First of all we have to make clear what we mean when we say that all the physical processes are active, and which are these processes. We already have mentioned that in GEANT [9], one can choose which physical processes will be used for the simulation.

In our simulation the active physical processes (The default option for GEANT [9]) were the following:

- Decay in flight with generation of secondaries.
- Multiple scattering according to Molière theory.
- Continuous energy loss without generation of δ -rays and full Landau-Vavilov-Gauss fluctuations.
- Photo-electric effect with generation of the electron.
- Compton scattering with generation of e^-.
- Pair production with generation of e^-/e^+.
- Bremsstrahlung with generation of γ.
- δ -rays production with generation of e^-

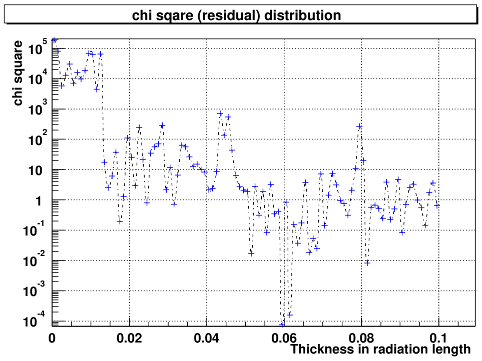

Fig. 12: *The χ^2 distribution vs thickness in radiation lengths, for Gaussian multiple scattering.*

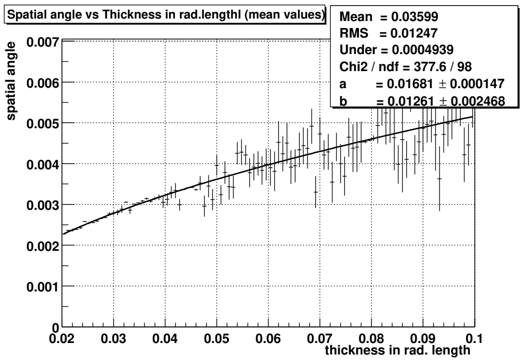

Fig. 13: *The θ_{space}^{rms} angular distribution vs thickness in rad. length and the fitted curve over this values, for Gaussian multiple scattering.*

- Positron annihilation with generation of photons.
- Hadronic interactions with generation of secondaries.
- The synchrotron radiation in magnetic field, is not simulated.

Now if we compare the results from this simulation with the results using only Molière multiple scattering we can see that they are not so different.

It has to be stated here, that in this case the deviation between the simulations results and the expected results according to formula (2) is smaller and in even more narrow region (Figs. 16, 17) But for better comparison reasons, we kept for the fitting the same cut, we used in the case of only Molière multiple scattering. The fitting results for that case are not so good, but still we can see that there is a good agreement with the theoretical predictions.

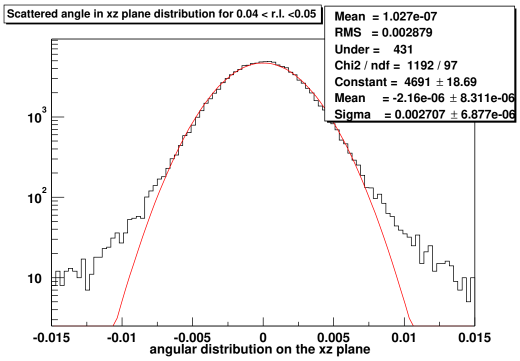

Fig. 14: *The θ_{plane} angular distribution the x-z plane, for Molière multiple scattering having all physical processes active.*

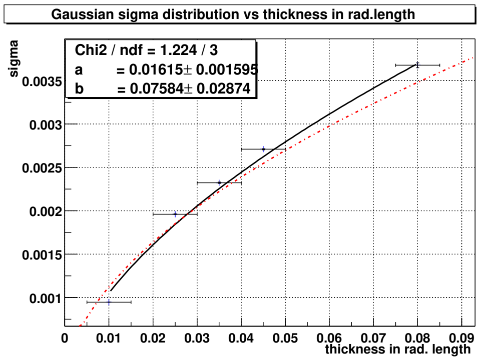

Fig. 15: *Gaussian sigmas vs thickness in rad. length, for Molière multiple scattering having all physical processes active. The dotted line is a plot of the formula (2), and the solid line is the fitted one.*

4 Conclusion

We studied the effect of multiple scattering to a 1 GeV π^- beam, traversing the HERA-B detector, using GEANT [9] Monte Carlo program. For our analysis we used three data sets obtained from the simulation. The first set gives information only for multiple scattering according to Molière theory, the second set gives information only for Gaussian multiple scattering and the third set gives information for multiple scattering according to Molière theory and for all the physical processes mentioned in subsection *3.3*.

A study of these three data sets showed that there is always a small region for very small thickness of the material, where there is a deviation between the simulated results and the theoretical expected results according to formula (2). Namely this region for Molière multiple

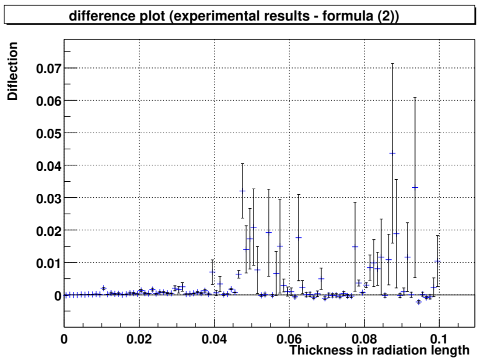

Fig. 16: *The θ^{rms}_{space} angular deviation vs thickness in radiation lengths, for Molière multiple scattering having all physical processes active.*

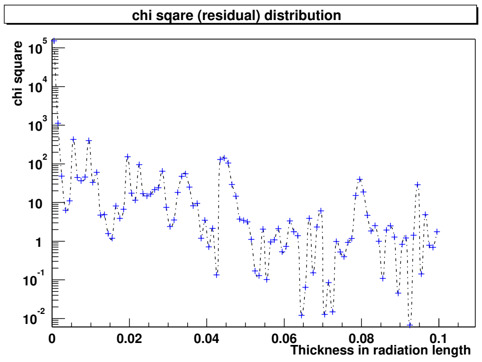

Fig. 17: *The χ^2 distribution vs thickness in radiation lengths, for Molière multiple scattering having all physical processes active.*

scattering is for thickness in radiation lengths < 0.01 cm, while for Gaussian multiple scattering the region of the deviation is for thickness in radiation lengths < 0.02 cm.

This deviation is because multiple scattering theories are not applicable for very thin materials. To overcome this limitation, single Coulomb scatterings are simulated in GEANT [9] .

So we can conclude that formula (2) describes very accurate Molière multiple scattering for material with thickness > 0.01 (in units of ratiation length) and can be used in very good agreement with the theoretical predictions.

5 Acknowledgments

I would like to thank the Zeuthen HERA-B group for making me feel welcome and for their help and support to this work. I would also like to thank my supervisor, Michael Walter and especially Siegmund Nowak for his valuable help and instructions.

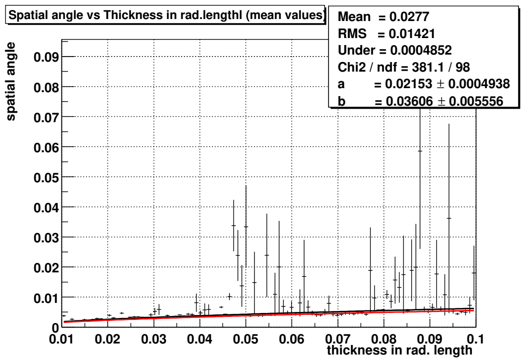

Fig. 18: *The θ^{rms}_{space} angular distribution vs thickness in rad. length and the fitted curve over this values, for Molière multiple scattering having all physical processes active.*

References

[1] G. Molière, Z. Naturforsch. **3a,** 78 (1948).

[2] H.A. Bethe, Phys. Rev. **89**, 1256 (1953).

[3] H. Snyder and W. T. Scott, Phys. Rev. **76**, 220 (1949).

[4] W.T. Scott, Rev. Mod. Phys. 35, 231 (1963).

[5] S.A. Goudsmit and J. L. Saunderson, Phys. Rev. **57**, 24 (1940).
S.A. Goudsmit and J. L. Saunderson, Phys. Rev. **58**, 36 (1940).

[6] H.W. Lewis, Phys. Rev **78**, 526 (1950).

[7] V.L. Highland, Nucl. Instrum. Methods **129**, 497 (1975).
V.L. Highland, Nucl. Instrum. Methods **161**, 171 (1979).

[8] G.R. Lynch and O.I. Dahl, Nucl. Instrum. Methods **B58**, 6 (1991).

[9] GEANT manual, CERN Program Library Long Writeup W5013.

[10] HERA-B Design Report, DESY-PRC 95/01, January 1995.

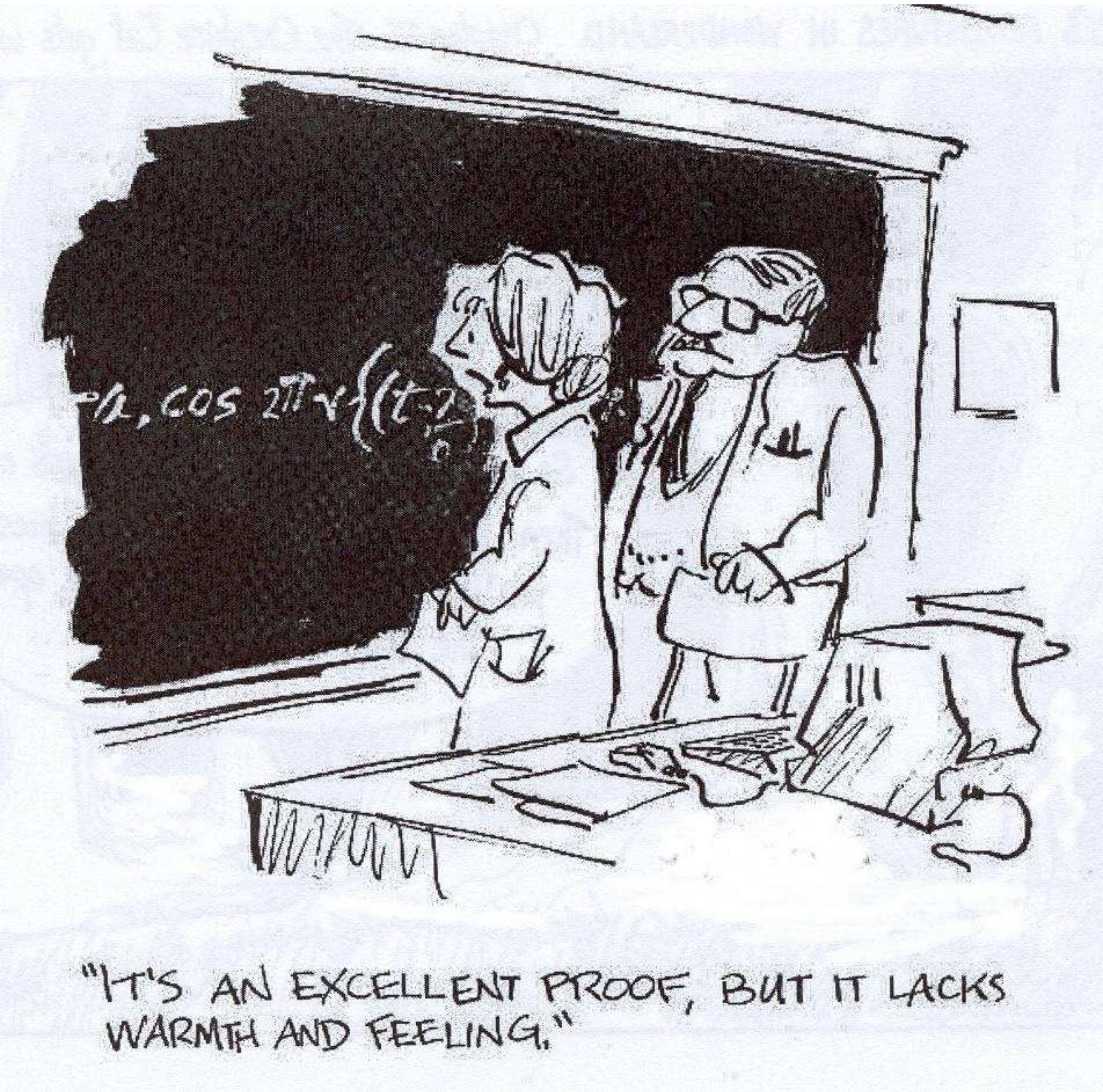
"IT'S AN EXCELLENT PROOF, BUT IT LACKS WARMTH AND FEELING."

Simulating electromagnetic showers with EGS4 and GEANT3

Diego Rodriguez
Departamento de F´isica. Universidad de Oviedo

Electromagnetic particles interact over all with matter by means of electromagnetic force. High energy electrons or positrons tend to loose energy in matter due to bremsstrahlung and photons tend to do pair creation. This means that an electromagnetic particle going into matter ends up creating a lot of secondary particles. That phenomena is called an electromagnetic shower. The aim of this work is trying to simulate this phenomena with two different Monte Carlo-based programs: EGS4 and GEANT3. The final idea of this simulations would be simulating the electromagnetic background for TESLA collimators.

1 Introduction

Photons and electrons interact with matter via Electromagnetic interaction. The main process for high energetic photons is pair creation, while for high energy electrons is bremsstrahlung. It means that each time an interaction takes place new particles are produced, so after a certain distance one has not the incident particle, but a lot of them. The phenomena is called electromagnetic shower or cascade.

Those showers have interest not just by themselves, but also they have a lot of practical interest. Many times one is interested in the stopping power of a material. That means that one wants to know what thickness of a certain material should br used for stopping charged particles. This is the situation we have in TESLA collimators.

TESLA is the new eletron-positron linear collider that DESY is planning to build in Hamburg. The idea for that is building a 33km linear collider in which TeV energies are accesible, due to absense of synchrotron radiation loss of energy. But having a big energy is not enough to have a machine suitable for high energy physics. Transition probabilities scale like the inverse of the fourth power of energy, which means that the bigger the energy the smaller the probability for a certain reaction to happen. It forces to increase the luminosity of the accelerator, so having a big current and a high density of particles is essential for a high energy accelerator. Apart from that a linear collider uses each bunch only once, which requires even bigger luminosity. Big luminosity is not just big current, but also big density in the beam. That means that the small size of bunches for TESLA is really important. Of course, there are also other practical reasons for good collimation to be necessary. For example, the smallest the bunch the best known the IP, wich is something really important for the vertex detector to be useful (which is fundamental if one wants to study QCD, Higgs physics...due to the necessity of tracking short lived particles, distinguishing jets...).

At a certain step of TESLA one needs to collimate the bunch. That means that one needs to give it a certain shape (more or less a cylinder...) in order to be able to focus it with the cuadrupoles...But when one produces the bunch it has not the correct shape nor size. It is more or less a cylinder but with tails in the perpendicular direction to its movement. In order to eliminate this tails one uses a collimator, which is just a slab of a certain material with a hole in the midle, so that only the part of the bunch which passes is that cylinder one would like to have.

The previously described situation is the ideal one. But in fact those tails will hit the slab of that material producing those electomagnetic showers. Some of the secondary particles of that shower will reach the end of the slab, so after the collimator there will be the collimated cylinder shaped bunch and also an electromagnetic back-

ground which of course is undesirable. That is why one is interested in simulating electromagnetic showers. If one is able to get an idea of the expected electromagnetic background due to this effect one will be able to either use the best material for reducing that noise for the collimator or to supress this background directly from the signal in the detector.
Simulations are really usefull in nowadays particle physics. Simulations are always based in Monte Carlo methods. The idea is using a random generator with the appropiate probability distribution to decide what will happen at each step of the tracking simulation. The point in using simulations in particle physics is that experiments and calculations are so complicated that one has to have a guide to what is expected, and that guide comes out of the simulation. Simulations are used for a huge variety of purpouses: reducing noise, deciding the correct range of energy... Because that importance is why people have developed various tools for doing that task. Perhaps the most well-known program for this purpouse is CERN's GEANT3. This is a widely used CERN program which allows the user to simulate lots of processes in user defined geometries and materials, and which tracks everything the user wants to know about the dynamics or kinematics of the reaction. But there are also other tools. One of them is SLAC's EGS4, which also allows to have control on the geometry and on the processes wich are taking place. The aim of this work will be starting with the simulations of electromagnetic showers in materials, with the idea of using it all for the simulations of that electromagnetic background in TESLA collimators. We will try to understand a bit of the physics beyond everything and to simulate it all with EGS4 and GEANT3. EGS4 is not a widely used program, so one of the biggest aims of this work is getting started in it.

2 A bit of physics

The correct picture of nature (at least at the energies we have!!!) is the one provided by quantum field theory (QFT). QFT is the only constitent way of linking two features which are essential: quantum behaviour and relativity. The interesting point for our pourpouse is that in QFT the number of particles is not fixed. It means that one can have creation and annihilation of particles. That is why we will obtain those electromagnetic showers.
For our pourpouses we are interested in QED (the quantum theory of Electromagnetic interactions). In QED one has charged leptons and the gauge U(1) boson which is the photon coupling to them. In our situation the fermionic field will be the electron. When the electron or the photon goes into material media it interacts with it via electromagnetic interactions. It means that it exchanges momentum via exchange of photons. Their interactions are equal to the ones between charged particles and photons in vacuum, but with two important remarks: material media are composed of non point like atoms, and those atoms are in a lattice and are much more massive than the electron. The first thing means that particles can interact with the inner parts of the atom if they have enough energy instead of interacting with it as a whole. The second statement means that one can consider the atom as an infinite massive particle. It all allows processes to occur that would be otherwise forbidden. That's the situation of bremsstrahlung. The atom absorbs momentum without recoil and allows an electron to produce just another electron and a photon. Otherwise this reaction would be forbidden by energy-momentum conservation.
Low energetic electrons and positrons tend to loose energy by ionization. That means that the electron hits the atom and takes away another electron, giving it a bit of its initial energy. The Bethe-Bloch[1] formula is a good description of this phenomena. If one increases energy the dominant process turns out to be bremsstrahlung. It occurs usually above a few MeV, so for the energies we are interested in the one can say that all the processes we have are bremsstrahlung. As we said before, bremsstrahlung would be forbidden if there would be no atom to take momentum and energy. After each bremsstrahlung interaction one has an electron and a photon, but there is still some energy deposited in the material due to the atom.
High energetic photons tend to do pair creation. They interact with the nuclear electromagnetic field and turn into an electron-positron pair, so after each pair creation one has a pair particle-antiparticle.
We are interested in the stopping power of the media. It is usually described by means of the so called radiation length. If is defined as the thickness of a material a particle needs to loose 1/e of

its initial energy by bremsstrahlung. The radiation length is a constant for each material and it is related to its desnity and atomic mass. There are theoretical predictions and also experimental fits for that radiation length as a function of Z and A for elements. See for example[1].

3 The programs we will use

As it was said before we will run EGS4 and GEANT3. The final purpouse of this work is simulating that electromagnetic background in TESLA collimators, but one of the by-the-way objectives is also getting started with EGS4 program. GEANT is a widely used program for particle physics, while EGS4 is not so widely used. It is also an older program, and perhaps its features are a bit less than those of GEANT3. But the point is that is much easier to use.
Both programs are based in Monte Carlo methods for simulating what is going on in the material. The basic idea is to provide a geometry, media set up and initial conditions to the program, and it will make the particle advance in finite steps, checking what happens to the particle at each step by a Monte Carlo simulation. Both programs have implemented the cross sections for different materials and different energies, so what they basically do is to throw a number and check in which region it falls, so that one can decide just by random generators what kind of interaction had happened and how much energy is depositated. After each step the program will have a list of outgoing particles with their energies. Then they will ask for the things the user wants to store (such as energies, charge...) and then they will check geometry and if everything is right, make advance all the particles which are in the shower as the first one. Of course, one can have control on the particles created by means of some flags and some parameters which can allow you to discard a particle.

3.1 EGS4

EGS4 was designed in the sixties in SLAC (USA). What it does is just making electromagnetic particles advance in a material media and have on account all the processes they can suffer for loosing energy.
EGS4 codes must be written not in FORTRAN but in MORTRAN, which is a sort of pre-processor for EGS4 codes. Then, after compling the pre-processed code one must run the program together with a so called PEGS4 file. PEGS4 is a program which comes in the same package as EGS4. It is the one which has the task of calculating all the cross sections, material data...
EGS4 program is a "simple one". Its structure is fixed. It has a main program in which you have to declare all your variables, initialize everything and declare the COMMON and COMIN (where the features of the program are) blocks. You also have to call HATCH subroutine and SHOWER subroutine. Those are internal subroutines which initialize the media data, make use of the PEGS4 file and start the run respectively. In fact the main control of the physical process is done by SHOWER. It computes what happens in each step and after it calls the user provided subroutine AUSGAB for scoring what the user wants. Then it calls HOWFAR, the other user provided subroutine for checking the geometry and makes the particle advance.
One important feature of EGS4 is that one can control the energies of the particles for being tracked, and consider that under a certain cut-off previously specified the particle is absorved. EGS4 has different options for selecting particles, types of interactions, reasons for discarding a particle... which can be looked up in the EGS4 tutorial or in one of the EGS4 manuals which are on the internet [2],[3].

3.2 GEANT3

GEANT3 is a much more common program in particle physics for Monte Carlo simulations. It is a CERN program, and its layout is much more complicated than EGS4. It also has a main program, in which one must do all the initializations and so on. Then one has to call GRUN, which is the subroutine which takes care of the shower. Then there is a long list of subroutines which are also called, many of them user-prepared. For further documentation see [4].
GEANT is a very powerfull tool for simulating physical processes. At first sight it seems to have much more options that EGS4.
GEANT3 is usually run with the help of CERN's PATCHY program. PATCHY is a program which allows you to introduce subroutines, features...in a very easy way in your code. In GEANT you don't have to provide any special file with media data, nor cut-offs...but you have to provide a data card (in a predefined

file) with some information about the events you are generating (number of events...).

There is a very interesting difference between EGS4 and GEANT3 for our purpouse. In GEANT3 you have to activate a flag (GSKING) if you want the secondary particles to be stored. So by default what you track is just the incident particle. In EGS4 things are different, and you always transport all the particles (assuming of course that their energy is above the cut-off). As we will see later this will create a problem in our EGS4 code. As a practical remark, it always a good idea to use some kind of energy counter so that one checks each time if energy is conserved as it should be.

4 The first steps with simulations...

As our firsts steps in the simulating world we will track particles and output their trajectories. This is just a visual way of getting a first idea of the thing, and to check in a fast way if things seem reasonable (if particles advance, if they create more secondaries...). What we will do is just shooting a particle to a slab of a certain material and store it position at each time. Then with that positions we can go to PAW and plot them. We can interpret those points as some of the points one would have in a bubble chamber, so actually what we get is the trajectory of the particles. The GEANT result is just for the incident particle (it means without activating GSKING). It is for a positron shot to 3cm thick Pb slab. As we will assume through all the paper, we are shooting the particles to that slab along z positive axis. In this case the slab started at x=-1.5cm and ended at x=1.5cm. For the EGS4 code it will start at x=0 and end at x=3cm. As it was said before, each point is one of the points in which the program ends a step and stores the information. One can think about them as the points in a bubble chamber. We show the xz view and the xy view (frontal one). It is shown in figues 1 and 2.

For EGS4 the result is much more confuse, because there we can see a lot of points, some of them for the incident particle, some of them for the secondaries. For example in fig. 3 we can see the track of a 9GeV electron in 3cm of Ne. Of course, the primary particle passes almost in a straight line.

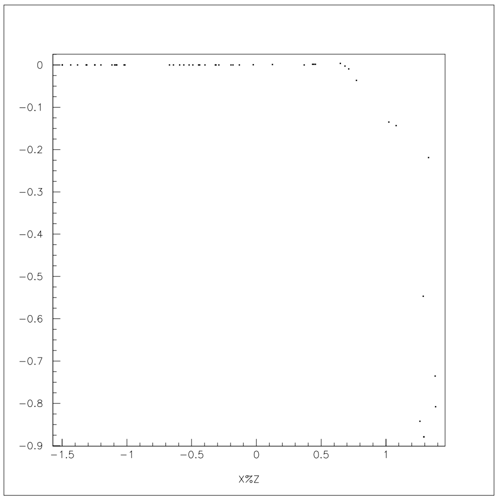

Fig. 1: *xz GEANT3 track for a 50MeV positron sent towards 3cm of Pb.*

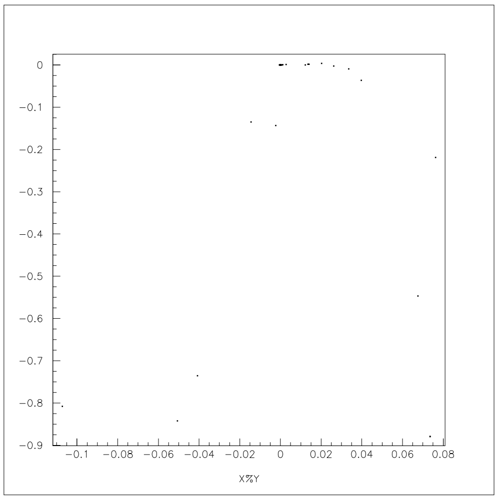

Fig. 2: *xy GEANT3 track for a 50MeV positron sent towards 3cm of Pb.*

As the last example we have a complete shower in 3cm of Pb originated by 50 50MeV electrons.

As one can see, the aspect of the shower is nice. One can see how the shower developes and how one gets a cone of particles symetric with respect to the z axis.

5 Simulation of the radiation lengths

For getting started with simulations using the tools we will try to simulate radiation lengths. As it was said before the radiation length is the length in which the energy drops down 1/e of

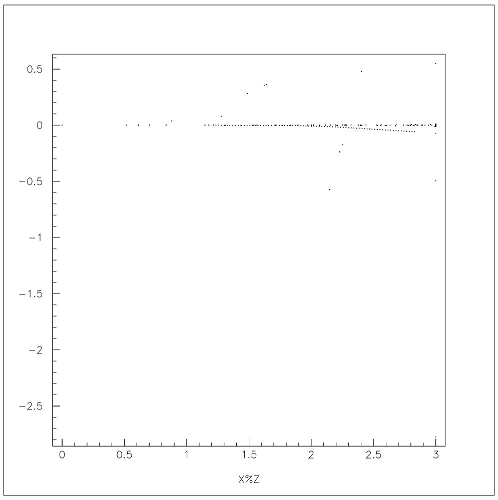

Fig. 3: *xz EGS4 track for a 9GeV electron sent towards 3cm of Ne.*

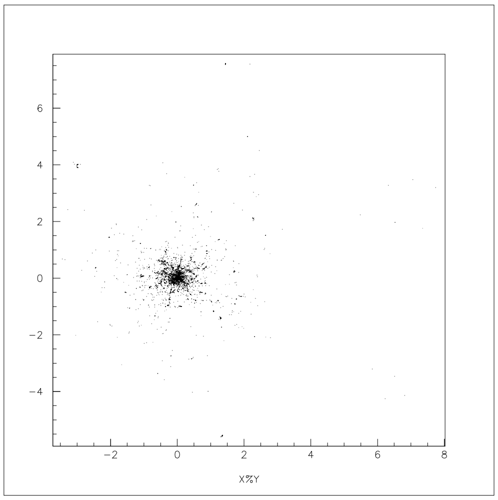

Fig. 5: *xz EGS4 simulation for 50 50MeV electrons in 3cm of Pb.*

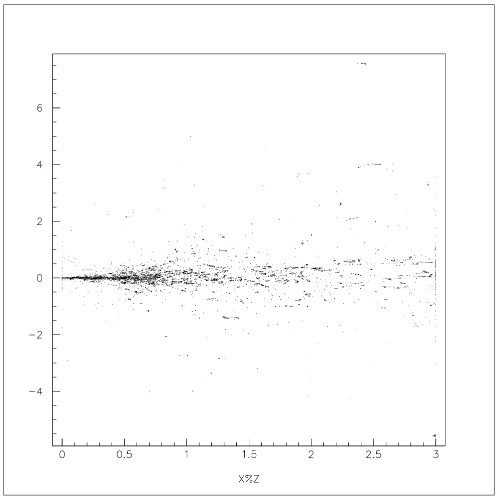

Fig. 4: *xz EGS4 simulation for 50 50MeV electrons in 3cm of Pb.*

the incident energy by bremsstrahlung.
In principle one should always turn on the flag which chooses among all the posible processes only bremsstrahlung, but as it was said before bremsstrahlung is the dominant process at high energies, so if one is simulating GeV electrons one can forget about turning that flag on.
The key to the simulation is that the radiation length is defined for the energy loss of the incident electron. That means that one has to track just the incident electron, look what happens to it in each interaction and compute how much energy it loosses. The rest of the particles in the shower are not interesting at all. One is just interested to get the energy as a function of the depth in the material for the incident electron. There arises one question...how do you know which one is the inicident electron? Well, electrons are indistinguishable particles, but their interactions are for sure the QED ones...and the only allowed interaction for an electron is a vertex with electron going in and electron and photon going out, so it is obvious which electron "is the inciden one". Of course, it is not the same electron, but for this purpouse one can forget about that. In fact, the presence of matter changes a bit this interaction. Now one has an ingoing electron and a photon and an electron going out, but there is some energy deposition to the material (it has to absorb some energy!!!). So what one needs is to track that inciden electron. As it was noticed before, it is something easy to do in GEANT3, but not that easy in EGS4. In that program there exists a pointer to the particles on stack, namely NP. When an interaction occurs, EGS4 it puts the secondary particles in the stack in order of decreasing energy, so that if one of the particles is discarded because being below some cut-off energy one can discard the rest of the stack (this is a way of saving CPU time). In general the incoming particle (for us the electron) tends to get the biggest outgoing energy, so most of the times NP=1 is the incoming particle. But the other situation can happen, and at a certain position NP=1 can turn out to be not that incident electron but a photon, making all the simulation useless.For avoiding this situation what one can do is just tracking the negative charged particles. In the

begining one has just a -1 charged particle. At the first interaction one will get as output particles an electron and a photon. If one discards automatically the photon (charge not equal to -1) one is again in the begining of the situation. It is obvious that this way one just tracks the incident particle.
In GEANT3, as it was said before, all this stuff is much easier, because by default the program tracks just the incident particle.
So at this stage now we know how to track the incident particle. Now the problem is how to compute the radiation length. The very first idea which comes to your mind is just computing the energy as a function of the distance and when it is below the apropiate cut-off (1/e) score the distance (which should be the radiation lenght). Then repeat it for many electrons and do statistics with all the data in for exaple PAW.
The idea of this program would be start with a very thin layer of some material, and shoot an electron to it and compute its energy when it goes out. If that energy is not in accordance with the appropiate threshold (the one from the definition of radiation length) then increase the thickness till the proper energy loss is found. Then score there the zhickness as an estimation of the radiation length, and repeat it again for having statistics.
At first sight it should work. But if one has a look to the output of the program it is evident that the energies at which the program decided that the radiation length had been achieved is not always close to the real one. That is because the discretization. Sometimes for one step the threshold is not achieved, and for the next step it is passed a lot. Because of this problem we uses another method for computing radiation lengths.
The method that we will use relies on the definition of the radiation length. What we will do is just throw particles to the slab and compute their energy as a function of the depth. This time we can use a very thick slab so that we have data enough.
Doing this is really straightforward in GEANT3 because the easy track of the incident particle, while for EGS4 one has to use that trick we mentioned before (just tracking the charged particles). As a first example we will shoot a beam of 5TeV electrons to 3cm of Pb (fig.6, 7), and compute the energies as a funtion of the depth for each one. The idea is having a lot of points to sample. The next step would be making a profile histogram of it all to get clearer numbers. By the moment, we will be happy just with an estimation of the numbers. This proceure will be a used throughout the paper.

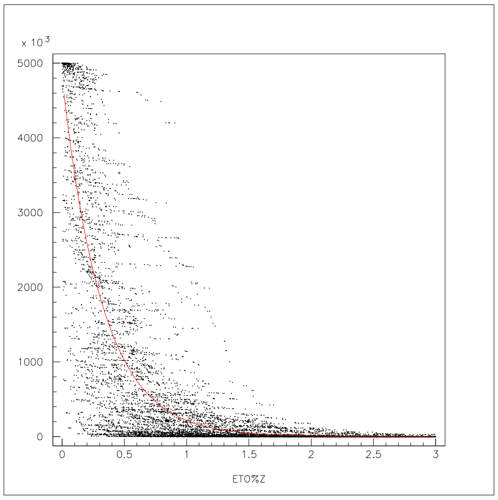

Fig. 6: *GEANT3 simulation for 5TeV electrons in 3cm of Pb.*

This scattered plot has been fit to an exponential. Perhaps the fit is not too good, so let's forget about it.

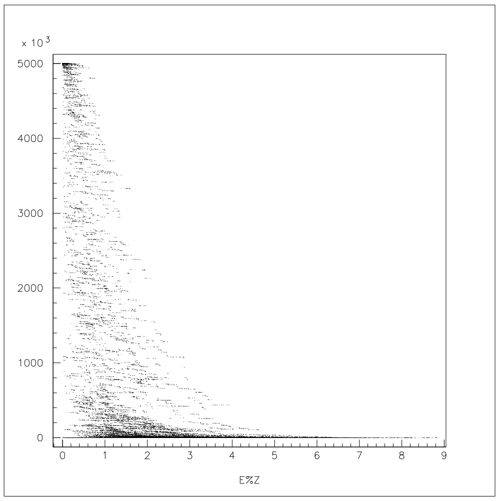

Fig. 7: *EGS4 simulation for 5TeV electrons in 3cm of Pb.*

As one can see, the shape of the curves is the same for the two programs. Perhaps one has more dispersion in the EGS code, but from this thing one would estimate (just by looking when the energy loss is under the threshold in a rough way) that the radiation length in Pb is

about 0.5cm for both plots, while in books it is 0.56cm, which is in good agreemente having on account that we only made an estimation.
We note that the two programs give more or less the same result indicating that (more or less) our programs are correct. Perhaps they could be made better. For example the EGS code tracks each electron more than one time, because it scores its position and energy as outgoing particle of the last step and ingoing particle for the next ones. That is why we get a lot of points all together in short lines. But what we can see there is also more or less the distance between interactions...which is just the distance between those small lines. In any case, as an introduction in the program and as an estimation of the simulation, one can forget about this problem by means of a lot of events.
Another important test of our calculations would be being sure that the shape and the value of the radiation lenght is the same for all incoming energies. That means that the curve should look more or less equal at all energies, and the distance at which the lost energy is 1/e of the initial one should be the same. This is shown in the next 2 GEANT plots (fig. 8, 9). One is done at 50MeV and the other at 5GeV for the same 3cm Pb slab. Forgetting again about that fit, one can see that using the estimator we discussed before the radiation length is more or less the same, and around 0.5cm, really near to the right number.

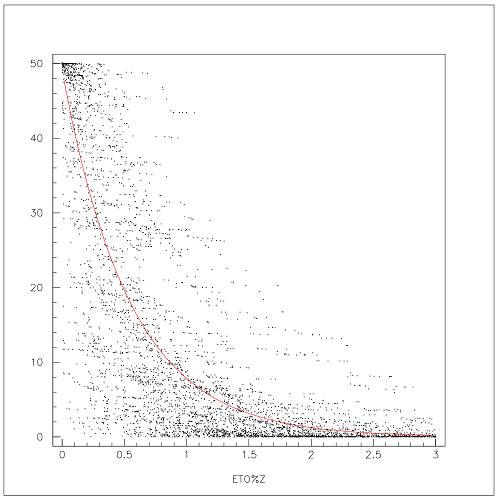

Fig. 9: *GEANT3 simulation for 50MeV electrons in 3cm of Pb. The radiation length is about 0.5cm.*

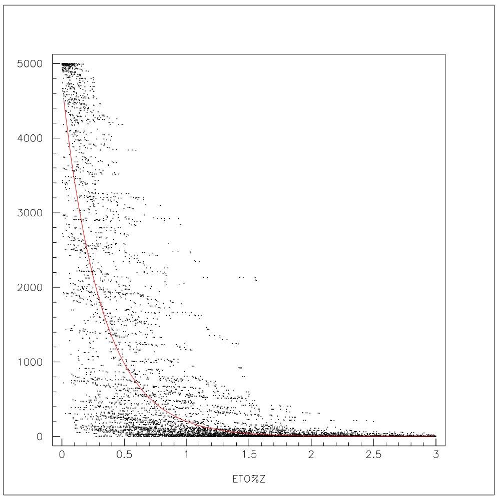

Fig. 8: *GEANT3 simulation for 5GeV electrons in 3cm of Pb. The radiation length is about 0.5cm.*

So the conclusion is that everything seems to be reasonable, and the radiation lenght seems to be more or less the expected number and to have more or less the behaviour it should have.

5.1 Estimation of radiation lengths of different materials

Now that we know that our code in both programs is more or less working, we will try to estimate this radiation length for different materials. On one hand we want to test if we get the right numbers and on the other hand we want to check that the behaviour is the correct one in a big range of materials with very different radiation lengths.
What we will do is just follow the procedure we have for different materials at a big but fixed energy (5TeV) so that we always have that bremsstrahlung we are looking for.
There is no point on showing all the plots we got. We will just show the table (table 1) with the estimated radiation lengths.
Of course, one must ask what is the precission of this data. As it was said before, this is just an estimation. The main aim for this work is getting started with EGS4, and that is why we will just estimate this numbers. A second step would be refining the code and getting for each distance not a lot of numbers, but a mean value. Perhaps the best idea would be performing at each thickness a statistical analisis to get the mean value (with errors!!!) of the energy at each depth. That would be the way of having a nicer plot and having also a definite curve for

fitting. In this case it not obvious if one must fit the data to a exponential or to a hyperbolic function.

Tab. 1: *Estimated and measured[1] radiation lengths (in cm) for different materials.*

MAT	ESTIMATED RL	MEASURED RL
Pb	0.5	0.56
Fe	0.6	0.56
C	18	18.8

Table 1 has been produced with the outcoming data of EGS4 program.
As one can see the results seem to be at least reasonables. They are consistent with the numbers that appear in the books[1].
It is important to notice that the program seems to be correct at all scales. That is why we chose C and Pb. Those 2 materials have a very different radiation lenght (2 orders of magnitude), and eventhough the program seems to have a good behaviour.

6 Conclusions

The main purpouse of this work was helping to get started with this EGS4 program, in order to be able to simulate background in TESLA collimators. In order to have some kind of guide we also used GEANT3 for comparing results.
We got a reasonable knowledge of EGS4, and we are able to design and modify EGS4 code. We also learnt particular details about the internal behaviour of this program and some coding tricks[5].
We used and practised all these technical stuff by means of the simulation of radiation lengths in different materials, using the previously well-known GEANT3 program for comparison.
Comparing EGS4 with GEANT3, the CERN's program seems at least at first sight to be more flexible, but more complicated. It seems that with GEANT3 one can do whatever we want, while with EGS4 refinated things turn out to be a bit complicated.—— What we got is something in principle reasonable. We got a definite number for radiation length in each material (not dependent on energy) which fit with the measured number in a reasonable way, so we can conclude that our understandig of EGS4 is in the right direction.
Of course there are some points which are for further studies:

- First of all a systematic analysis of the data should be done. The proposal would be fitting to the proper function the deposited energy for each depth, so we get the mean deposited energy with errors. One suggestion [6] could be a *profile histogram.* Then, one can use all of this numbers to fit them and extract the exact radiation length, which should be near the one on books.

- Some improvements on the algorithm should be done. We have said that with this algorithm we are computing more that one time each electron. This should be a little effect in our work (in the end we just estimated if the numbers were reasonable), but it is not acceptable for further works.

- Some deeper knowledge of EGS4 and MORTRAN is required. For example the way of storing the data is somewhat rude. It should be improved for an efficient management of the data.

As a conclusion one can say that the main task of this work was computing with EGS4, so physics is somehow appart. In the end we got a satisfactory point with the knowledge of EGS4 which we hope will be useful for future works.

Acknowledgments

I would like to express my gratitude to all the people here in DESY-Zeuthen, and specially to my supervisor H.J.Schreiber for his patience with me and my problems with computers.
Spetial thanks for V.Balandin for helping me so much with that EGS4 code and for all the time he spent with me explining me it all. I cannot forget all the other summerstudents, who have become my family over this 2 months, and spetially Ivan Calvo, who has become not just my partner but my friend.
I also learnt that distance is never too big...thanks to all the students in Hamburg for all the friendship and support they gave me,

and spetially to Lucas and Belen. They made this summer unforgetable...
Also I must thank my family and my friends there in Gijon for being there everytime I needed them.
And of course my deepest and sincere gratitude to M.A.R.Osorio and A.Nieto. They have been not just my scientific guides but also my friends, my advisors and even sometimes my fathers.

References

[1] *Pysical Review D*, 1996, page 132 and ff.

[2] W.R. Nelson, H. Hirayama and D.W.O. Rogers, *The EGS4 Code System*, SLAC-Report-265,1985.

[3] H. Hirayama and Y. Namito, *Lecture Notes of EGS4 Course at KEK*, KEK International 99-5,1999.

[4] CERN Program Library Long Writeup W5013, *GEANT Detector Description and Simulation Tool*, CERN, 1993

[5] D. Rodriguez, *Basic basics of EGS4*.

[6] A.Garas, private comunication.

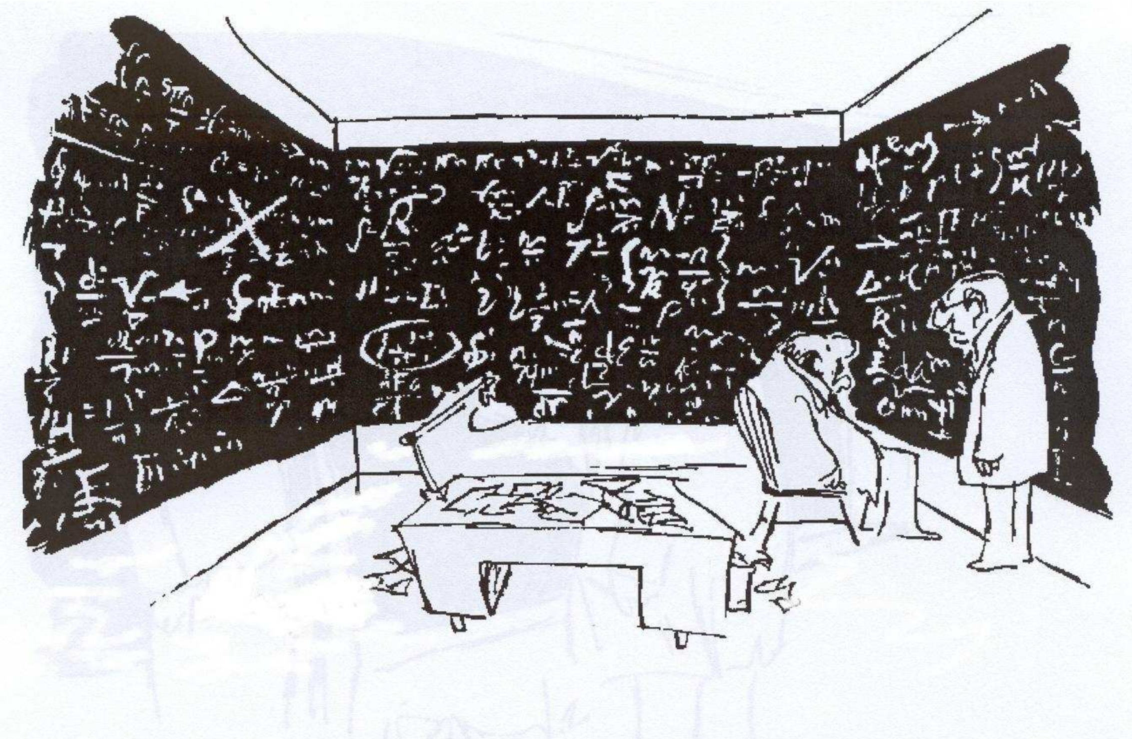

"Whatever happened to *elegant* solutions?"

The boson sector of the Standard model

Yaroslav Rodionov
Moscow Institute of Physics and Technology
Dolgoprudny, Moscow region,

This summarizing chapter is devoted to classical Higgs mechanism in the Standard model.

1 Introduction

1.1 A brief summary of the results of Yang-Mills theory

It's well-known that the usual QED lagrangian has $U(1)$ symmetry. The main purpose of Yang-Mills theory is the construction such a lagrangian , that would have $SU(2)$ symmetry. Let's consider a gauge scalar field:

$$\phi = \begin{pmatrix} \phi_1 \\ \phi_2 \end{pmatrix}$$

(the fundamental representation of $SU(2)$)

$$\mathcal{L} = \partial_\mu \phi^\dagger \partial_\mu \phi - m^2 \phi^\dagger \phi - \lambda(\phi^\dagger \phi)^2 \tag{1}$$

This lagrangian has a global symmetry $SU(2)$

$$\phi(x) \longrightarrow \phi\prime(x) = \omega\phi(x)$$

$$\omega \in SU(2)$$

where ω doesn't depend on space-time coordinates.

Let's try to modify our lagrangian to obtain one that has a gauge $SU(2)$ symmetry.

$$\phi(x) \longrightarrow \phi\prime(x) = \omega(x)\phi(x)$$

$$\omega(x) \in SU(2)$$

It may be easily seen that the discribed lagrangian hasn't got a gauge symmetry becouse of the presence of the terms $\partial_\mu \omega(x) \cdot \phi(x)$. As usual we should introduce a covariant derivative D_μ which satisfies the relation:

$$(D_\mu \phi)\prime = \omega D_\mu \phi \tag{2}$$

Following the standard procedure we introduce the vector field A_μ. And for our derivative we 'll have the expression:

$$D_\mu \phi = \partial_\mu \phi + A_\mu \phi \tag{3}$$

Under gauge transformations the field A_μ must transforms like

$$A\prime_\mu = \omega A_\mu \omega^{-1} + \omega \partial_\mu \omega^{-1} \tag{4}$$

if we want to satisfy the relation (2). Let's now consider an infinitesimal transformation

$$\omega = 1 + \epsilon(x) \tag{5}$$

where ϵ belongs to the Lie-algebra of the gauge group $SU(2)$ We see that

$$\omega \partial_\mu \omega^{-1} = -\partial_\mu \epsilon(x) \tag{6}$$

$\Rightarrow \omega \partial_\mu \omega^{-1} \in$ Lie-algebra of $SU(2)$ So we may conclude that A_μ also belongs to the Lie-algebra of $SU(2)$ It's absolutely obvious that

$$A_\mu \in ASU(2) \quad \forall \omega \in SU(2)$$

where $ASU(2)$ is a designation of the Lie algebra of $SU(2)$

It's the consequence of the fact that $\omega A_\mu \omega^{-1}$ is nothing else than the adjoint representation of $SU(2)$

Gauge vector field A_μ is well-known as Yang-Mills field. Now we should construct the lagrangian for the field A_μ itself. It may be easily checked that the tensor:

$$F_{\mu\nu} = \partial_\mu A_\nu - \partial_\nu A_\mu + [A_\mu, A_\nu] \tag{7}$$

transformes like:

$$F\prime_{\mu\nu}(x) = \omega(x) F_{\mu\nu}(x) \omega^{-1}(x) \tag{8}$$

Now we may introduce a gauge-invariant lagrangian like this:

$$\mathcal{L}_A = \frac{1}{2g^2} Tr F_{\mu\nu} F^{\mu\nu} \tag{9}$$

where g^2 is a positive constant.

We may see the crucial difference between a non-abelian gauge theory and the usual electrodynamics, namely: the non-abelian lagrangian has terms that are third or fourth order of the field $A_\mu : Tr(\partial_\mu A_\nu \cdot A^\mu A^\nu)$ and $Tr(A_\mu A_\nu A^\mu A^\nu)$ That means that the motion equations of Yang-Mills field are non-linear even in the absence of other external fields. The gauge field A_μ may be expressed in terms of three real fields the following way:

$$A_\mu(x) = -ig\frac{\sigma^a}{2}A^a_\mu(x) \tag{10}$$

where $a = 1, 2, 3$; and $\frac{\sigma^a}{2}$ are Hermitian generetors of $ASU(2)$ i.e Pauli-matrices.

Than we find the expression of the field tensor $F_{\mu\nu}$:

$$F_{\mu\nu} = -ig\frac{\sigma^a}{2}(\partial_\mu A^a_\nu - \partial_\nu A^a_\mu)+$$

$$+(ig)^2 A^a_\mu A^b_\nu \left[\frac{\sigma^a}{2}, \frac{\sigma^b}{2}\right] = -ig\frac{\sigma^a}{2}(\partial_\mu A^a_\nu - \partial_\nu A^a_\mu)-$$

$$-g^2 A^a_\mu A^b_\nu i\epsilon^{abc}\frac{\sigma^c}{2} \Longrightarrow$$

$$F^a_{\mu\nu} = \partial_\mu A^a_\nu - \partial_\nu A^a_\mu + g\epsilon^{abc}A^b_\mu A^c_\nu \tag{11}$$

So, we may express our lagrangian like following:

$$\mathcal{L} = \frac{1}{2g^2}F^a_{\mu\nu}F^{\mu\nu\ a}(-ig)^2 Tr\frac{\sigma^a}{2}\frac{\sigma^b}{2} = -\frac{1}{4}F^a_{\mu\nu}F^{\mu\nu\ a} \tag{12}$$

This is a prominent Yang-Mills lagrangian.

2 The Boson sector of the Standard Model

2.1 General situation

The boson sector of the standard model is a sample of a partial breaking of a gauge symmetry. The general situation is following:

Let's G is a gauge group, A_μ is a gauge vector field and

$$\left(A^{vac}_\mu, \phi^{vac}\right)$$

is a basic state.

Assume that $A^{vac}_\mu = 0$ and ϕ^{vac} is a constant. If we switch off all the gauge fields the symmetry group G will become to be global. Vacuum state ϕ^{vac} breaks the global symmetry to some extent. Following a standard procedure we may devide the generators of AG in two parts: the generators of a stability subgroup H: (t_h), and the others: (t_α) If the group G was really the group of a global symmetry there would be Nambu-Goldstone massless bosons in the model. And the number of them would be equal to the number of the non-stability generators. Let's now assume that our group is a gauge one. Than our model will conserve the gauge symmetry H and the bosons which correspond to the AH generators will remain to be massless. But the fields corresponding to the non-stability generators will become to be massive and Nambu-Goldstone bosons will disappear.

The most vivid illustration of this general situation is the standard model.

2.2 Standard model

Gauge group: $SU(2) \times U(1)$

For each component: $SU(2)$ and $U(1)$ we have different coupling constants: g and $g\prime$; Let A^a_μ and B_μ to be the gauge fields for $SU(2)$ and $U(1)$ groups respectively. Model contains one doublet of the scalar fields. Generators of $SU(2)\times U(1)$ are $\frac{\sigma^a}{2}$ and $Y = \frac{1}{2}$. Y is a so-called hypercharge.

The lagrangian must be a polynomial of not more than the 4th power. All these requirenments fix it:

$$\mathcal{L} = -\frac{1}{4}F^a_{\mu\nu}F^{\mu\nu\ a} - \frac{1}{4}B_{\mu\nu}B^{\mu\nu}+$$

$$+(D_\mu\phi)\dagger D^\mu\phi - \lambda\left(\phi\dagger\phi - \frac{v^2}{2}\right)^2 \tag{13}$$

where

$$F^a_{\mu\nu} = \partial_\mu A^a_\nu - \partial_\nu A^a_\mu + g\epsilon^{abc}A^b_\mu A^c_\nu$$

$$B_{\mu\nu} = \partial_\mu B_\nu - \partial_\nu B_\mu$$

$$D_\mu\phi = \partial_\mu\phi - i\frac{g}{2}\sigma^a A^a_\mu\phi - i\frac{g\prime}{2}B_\mu\phi$$

As the vacuum state we choose:

$$A^a_\mu = B_\mu = 0$$

$$\phi = \begin{pmatrix} 0 \\ \frac{v}{\sqrt{2}} \end{pmatrix}$$

Stability generators are such matrices that:

$$Q\phi^{vac} = 0$$

So we may conclude that

$$Q = \begin{pmatrix} a & 0 \\ b & 0 \end{pmatrix}$$

But matrix Q must be hermitian $\Longrightarrow$

$$Q = \begin{pmatrix} 1 & 0 \\ 0 & 0 \end{pmatrix}$$

So there is a stability subgroup with generator Q: $U(1)_{em}$. We expect that there will be a massless gauge field corresponding to this subgroup in the lagrangian.

Let's consider small excitations in the neighbourhood of the vacuum state. We fix the unitary calibration.

$$\phi = \begin{pmatrix} 0 \\ \frac{v}{\sqrt{2}} + \frac{\chi}{\sqrt{2}} \end{pmatrix}$$

(it may be easily shown that we always can choose such a colibration) Here $\chi(x)$ is a real field. In this case the unitary calibration doesn't fix the vacuum state completely. In fact: the gauge transformation doesn't change this state:$Q\phi = \phi$. So the full lagrangian has an $U(1)_{em}$ invariance.

To find the quadratic lagrangian we should calculate the covariant derivative:

$$D_\mu \phi = \partial_\mu \phi + \left[-\frac{ig}{2} A^1_\mu \begin{pmatrix} 0 & 1 \\ 1 & 0 \end{pmatrix} - \frac{ig}{2} A^2_\mu \begin{pmatrix} 0 & -i \\ i & 0 \end{pmatrix} \right] \phi$$

$$+ \left[-\frac{ig}{2} A^3_\mu \begin{pmatrix} 1 & 0 \\ 0 & -1 \end{pmatrix} - \frac{ig\prime}{2} B_\mu \begin{pmatrix} 1 & 0 \\ 0 & 1 \end{pmatrix} \right] \phi$$

This way we obtain:

$$D_\mu \phi = \begin{pmatrix} -\frac{ig}{2\sqrt{2}} (A^1_\mu - iA^2_\mu)(v + \chi) \\ -\frac{i}{2\sqrt{2}} (g\prime B_\mu - gA^3_\mu)(v + \chi) + \frac{1}{\sqrt{2}} \partial_\mu \chi \end{pmatrix}$$

Let's introduce two complex fields:

$$W^\pm_\mu = \frac{1}{\sqrt{2}} (A^1_\mu \mp iA^2_\mu) \qquad (14)$$

We also introduce two real ones:

$$Z_\mu = \frac{1}{\sqrt{g^2 + g\prime^2}} (gA^3_\mu - g\prime B_\mu) \qquad (15)$$

$$A_\mu = \frac{1}{\sqrt{g^2 + g\prime^2}} (gB_\mu + g\prime A^3_\mu) \qquad (16)$$

The fields Z_μ A_μ satisfy the relation:

$$Z^2_\mu + (A_\mu)^2 = (A_{\mu^3})^2 + B^2_\mu \qquad (17)$$

After a simple calculation we'll obtain the expression:

$$D_\mu \phi = \begin{pmatrix} -i\frac{gv}{2} W^+_\mu \\ \frac{1}{\sqrt{2}} \partial_\mu \chi + \frac{i\sqrt{g^2+g\prime^2}}{2\sqrt{2}} v Z_\mu \end{pmatrix} + \begin{pmatrix} -i\frac{g}{2} W^+_\mu \chi \\ \frac{\sqrt{g^2+g\prime^2}}{2\sqrt{2}} Z_\mu \chi \end{pmatrix}$$

This way we find the contribution of the covariant derivative in to the quadratic lagrangian.

$$[(D_\mu \phi)\dagger D\mu\phi] = \frac{1}{2} (\partial_\mu \chi)^2 + \frac{g^2 v^2}{4} \mathcal{W}^+_\mu \mathcal{W}^-_\mu + \qquad (18)$$

$$+ \frac{1}{2} \left(\frac{(g^2 + g\prime^2) v^2}{4} \right) Z^2_\mu$$

Let's calculate the kinetic term in the lagrangian:

$$-\frac{1}{4} \mathcal{F}^a_{\mu\nu} \mathcal{F}^{\mu\nu\ a} - \frac{1}{4} B^2_{\mu\nu} = \qquad (19)$$

$$= -\frac{1}{2} \mathcal{W}^+_{\mu\nu} \mathcal{W}^{\mu\nu -} - \frac{1}{4} (\mathcal{F}^3_{\mu\nu})^2 - \frac{1}{4} (B_{\mu\nu})^2$$

Here $\mathcal{F}^a_{\mu\nu}$ and $\mathcal{W}^\pm_{\mu\nu}$ are the tensors of the fields A^a_μ and $W^\pm_\mu$ respectivly.

Using the identity (17) we may rewrite the right part of this expression.

$$-\frac{1}{2} \mathcal{W}^+_{\mu\nu} \mathcal{W}^{\mu\nu\ -} - \frac{1}{4} \mathcal{Z}_{\mu\nu} \mathcal{Z}^{\mu\nu} - \frac{1}{4} F_{\mu\nu} F^{\mu\nu}$$

where

$$\mathcal{Z}_{\mu\nu} = \partial_\mu Z_\nu - \partial_\nu Z_\mu$$

$$F_{\mu\nu} = \partial_\mu A_\nu - \partial_\nu A_\mu$$

So we see that there are standard kinetic terms for the complex vector field $W^\pm_\mu$ and real vector fields Z_μ A_μ in our lagrangian.

At last the quadratic part of the potential is equal to

$$V = \lambda v^2 \chi^2$$

We may introduce now the masses of our new fields:

$$m_W = \frac{gv}{2}$$

$$m_Z = \frac{\sqrt{g^2 + g\prime^2} v}{2}$$

$$m_\chi = \sqrt{2\lambda} v$$

Collecting all the terms we obtain the full lagrangian:

$$\mathcal{L} = -\frac{1}{2}\mathcal{W}^+_{\mu\nu}\mathcal{W}^{\mu\nu\,-} + m_W^2 W^+_\mu W^{\mu-} - \frac{1}{4}F_{\mu\nu}F^{\mu\nu} - \quad (20)$$

$$-\frac{1}{4}\mathcal{Z}_{\mu\nu}\mathcal{Z}^{\mu\nu} + \frac{m_Z^2}{2}Z_\mu Z^\mu + \frac{1}{2}(\partial_\mu\chi)^2 - \frac{m_\chi^2}{2}\chi^2$$

This lagrangian describes the massive complex vector field:W^+_μ(and $W^-_\mu = (W^+_\mu)^*$) with the mass m_W (the field of W-bosons), massless vector field (photon A_μ), massive real vector field with the mass m_W(Z-bozons) and the massive real scalar field χ(Higgs-field)

Let's calculate the charges of $W^\pm$-bosons. We know that the vacuum state is invariant with respect to group $U(1)_{em}$ i.e. with respect to transformations

$$\omega(x) = e^{i\frac{\sigma^3}{2}\alpha(x)} \quad (21)$$

and

$$\Omega(x) = e^{i\alpha(x)} \quad (22)$$

simultaneously. Higgs doublet remains to be invariant under such transformations (i.e it's a neutral field) But

$$\hat{A}_\mu \to \hat{A}_\mu\prime = \omega\hat{A}_\mu\omega^{-1} + \omega\partial_\mu\omega^{-1} \quad (23)$$

$$\hat{B}_\mu \to \hat{B}_\mu\prime = \hat{B}_\mu + \Omega\partial_\mu\Omega^{-1} \quad (24)$$

where

$$\hat{A}_\mu = -ig\frac{\sigma^a}{2}A^a_\mu \qquad \hat{B}_\mu = -ig\prime B_\mu$$

Using the explicit formulas (21) and (22) we obtain:

$$\hat{A}\prime_\mu = -i\frac{g}{2}\left[(\cos\alpha A^1_\mu + \sin\alpha A^2_\mu)\sigma^1\right] - \quad (25)$$

$$-i\frac{g}{2}\left[(cos\alpha A^2_\mu - sin\alpha A^1_\mu)\sigma^2\right] - ig\frac{\sigma^3}{2}\left(A^3_\mu + \frac{1}{g}\partial_\mu\alpha\right)$$

From this expression we may find out the transformation rules for the fields A^1_μ A^2_μ A^3_μ, namely:

$$(A^1_\mu \pm iA^2_\mu)\prime = (A^1_\mu \pm iA^2_\mu)e^{\mp i\alpha} \quad (26)$$

$$A^3_\mu\prime = A^3_\mu + \frac{1}{g}\partial_\mu\alpha \quad (27)$$

and for the field B_μ using (22) and (24) we find

$$B_\mu\prime = B_\mu + \frac{1}{g}\partial_\mu\alpha \quad (28)$$

But $A^1_\mu \pm iA^2_\mu$is nothing as $W^\pm_\mu$ So we may conclude that $W^\pm$-bozons has charges ± 1. From fields A^3_μ and B_μ it's easily seen that we may compose the neutral field:

$$Z_\mu \propto gA^3_\mu - g\prime B_\mu$$

We see that lagrangian that has the $SU(2) \times U(1)$ symmetry led to the existance of the charged $W^\pm$-bosons , neutral Z-boson and Higgs boson. $W^\pm$ and Z were experementally discovered and it was a great success of the standard model.

Acknowledgments

I want to thank prof. Fred Jegerlehner and Michail Kalmykov for their support during the summer student program at DESY-Zeuthen. This support was very useful for me. Our discussions helped me get a good understanding of the basic principals of gauge theories. I'd like to express a special gratitude to Michail Kalmykov, whose support let me achieve a profound background for further study of Quantum Field Theory.

References

[1] F. Jegerlehner Electroweak Theory and LEP Physics.

[2] Michail E. Peskin Daniel V.Schroeder An introduction to Quantum Field Theory.

Influence of cameras's finite sensitivity on electron beam size measurements

J. Bähr[a], V. Miltchev[a]
[a] DESY Zeuthen, Platanenalle 6, 15738 Zeuthen, Germany

B. Skorodumov[b]
[b] MEPhI(State University), Kashirskoe Sh.31, Moscow, Russia

The perfomance of JAI CV-M10RS cameras in electron beam RMS size measurement is studied. A problem with high black level is investigated. Some possible solutions are presented. Error estimations are given.

1 Introduction

The Photoinjector Test Facility at DESY Zeuthen (PITZ, Fig.1) is a test stand for a research and development of laser driven electron sourses, which can be applied to Free Electron Lasers (FEL). The scientific goal of the project is to obtain electron beam with optimized transverse and longitudial emittance [1]. The process of optimization of the beam quality includes an extended investigation of diverse beam parameters like transverse size, transverse beam position etc. In order to make such a research, a CCD camera set up is used.

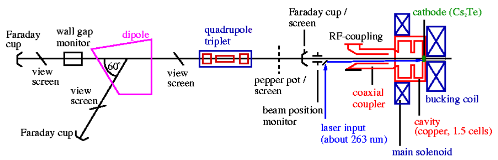

Fig. 1: *Schematics overview of PITZ*

Fig. 2: *The view of the CV-M10RS camera*

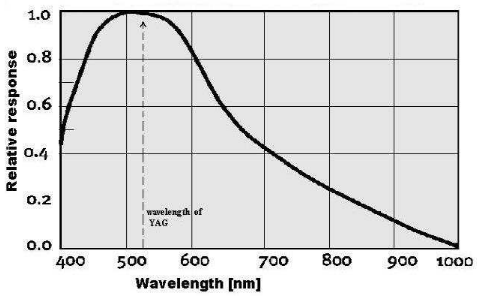

Fig. 3: *Relative response of JAI CV-M10RS cameras as function of the wave length*

2 TV-system

The TV-system at PITZ employs video cameras JAI CV-M10RS (see Fig.2). The features of these cameras are summarized in Table 1 and Fig.3 [2]. In addition, the cameras are remote controllable via an $RS232$ interface (see Fig.4). The most important parameters, which can be varied from remote are as follows:

- GAIN defines the amplification factor for the video signal, applied for a given CCD camera. When using a high gain, the camera works in saturation mode (see Fig.5). Therefore, the gain is usually set to the level just below the saturation[1].

- SET UP LEVEL defines the software intensity thereshold (minimum intensity, which can be detected by the camera, see Fig.6). Usually set up level is set up to the smallest value.

[1] Due to the saturation the results of the image processing could be inaccurate

Tab. 1: *Specifications of CCD camera.*

Image area	6.4mm(H)x4.8mm(V)
Cell size	$8.3\mu \star 8.3\mu m$
External trigger mode	Edge pre-selector pulse width control
Sensitivity	$1.0\text{lux} = 1.5\frac{mW}{m^2}$ (for the green light)
Scan mode	Interlaced/Non-interlaced
Gamma	$1.0 - 0.45$
Gain	Manual/Avto
Interface	RS 232

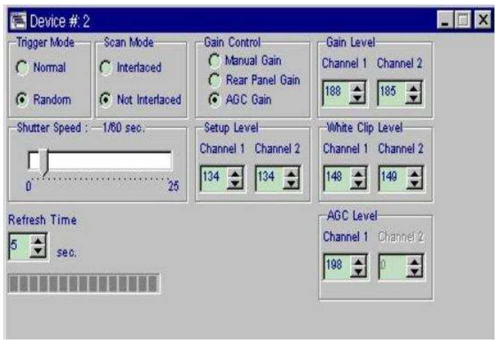

Fig. 4: *RS232 client interface*

- WHITE CLIP defines the intensity level, above which the signal will be clipped (Fig.7). Usually white clip is set to the highest possible value.

3 Typical experimantal setup

The typical experimental setup for transverse measurements put into practice at PITZ is illustrated on Fig.8. The incoming electrons hit YAG(Yttrium Aluminium Garnet) screen and couse a scintillation in the volume of the YAG cristal. The emitted photons are detected by CCD camera. The entire image is later statistically processed.

4 Concept of image processing

In order to obtain values for beam's Root Mean Square (RMS) size S and position $\bar{X}$ the acquired video data is statistically processed. Assuming that the light intensity distribution is

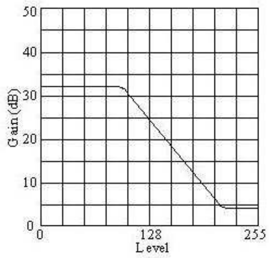

Fig. 5: *Dependance of the gain on control level value*

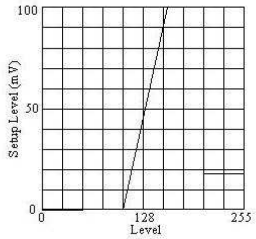

Fig. 6: *Dependance of the black level on control value*

linearly proportional to the transverse density of the electrons in the electron beam, one defines a particle distribution function $f(x, y)$ in the $\{X, Y\}$ transverse space. The RMS values are calculated in the standart way:

$$\int\int f(x,y)dxdy = 1 \tag{1}$$

$$\bar{x} = \int\int f(x,y)xdxdy \tag{2}$$

$$S^2 = \int\int (x-\bar{x})^2 f(x,y)dxdy \tag{3}$$

5 The Problem

In the measurenent procedure described above (see in Chapter 4), it is assumed that the threshold T (Fig. 9) of the sensitivity of the CCD camera is infinitely small ($T \to 0$). During the measurement, the CCD camera provides only information about the portion above the threshold T. On Fig.9 this corresponds to the areas $A1$ and $A2$. It has to be underlined that the both curves $G_1(x), G_2(x)$ correspond to the same distribution $f(x, y)$ in the $\{X, Y\}$ transverse space, but the gain level G is different for $A1$ and $A2$. Hence, the measured values S_{meas}, $\bar{X}_{meas}$ will differ for the different gains.

$$S_{meas} \neq S_{meas} \neq S_{teor} \tag{4}$$

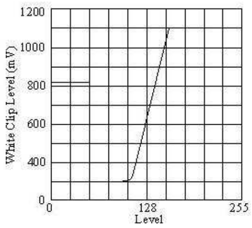

Fig. 7: *Dependance of the white clip on control level value*

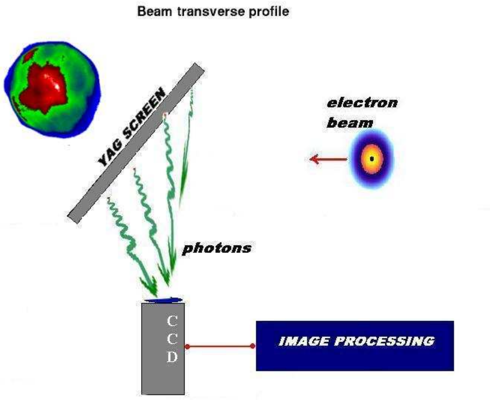

Fig. 8: *The typical set up*

Here S_{teor} is a theoretical value which could be obtained if the threshold T is infinitely small ($T \to 0$). In general, the beam size is systematically underestimated ($S_{meas} < S_{teor}$). The goal of our research is to develop measurement procedure which gives a result independent of the gain G. Into account has to be taken, that at high gains the camera works in saturation mode (Fig.9)

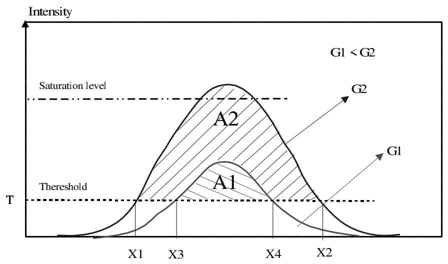

Fig. 9: *Demonstration of thereshold and flat top of CCD camera*

6 Experimental testing

In order to experimentally verify the effect described in Chapter 5, we decided to compare a measured RMS size with the one predicted by the theory. For this purpose we used a diffraction pattern created by a lazer beam of wave length λ on a narrow rectangular slit of width a (Fig.10).

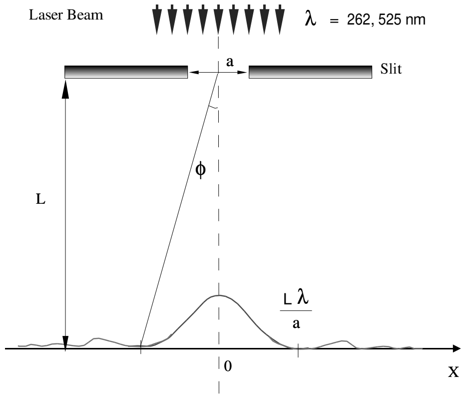

Fig. 10: *Principal sketch of experiment*

A transverse size σ_{exp} of the central diffraction maximum was measured for different slit widths:

$$a = 20\mu m, 50\mu m, 80\mu m, 100\mu m \tag{5}$$

and for two different wavelength λ:

$$\lambda = 262nm, 525nm \tag{6}$$

A theoretical prediction σ_{teor} for the transverse size of the central maximum was derived by using the well known expression for intensity [3], [4].

$$I(x,\phi) = I_0 \frac{\sin^2\left[\frac{\pi a}{\lambda}\sin\phi\right]}{\left[\frac{\pi a}{\lambda}\sin\phi\right]^2}. \tag{7}$$

$$\sigma^2_{teor}(x) = \frac{\int_0^{\frac{L\lambda}{a}} x^2 \frac{\sin^2\left[\frac{\pi a}{\lambda L}\right]}{\left[\frac{\pi a}{\lambda L}\right]^2} dx}{\int_0^{\frac{L\lambda}{a}} \frac{\sin^2\left[\frac{\pi a}{\lambda L}\right]}{\left[\frac{\pi a}{\lambda L}\right]^2} dx} \tag{8}$$

The results[2] of the experiment σ_{meas} compared with theoretical predictions σ_{teor} are given in Table 2 and Fig.12, 13, 14. As one can see in Table 2, the experementally measured

[2] Note: in all measurements the CCD camera was in linear mode, without saturation.

Tab. 2: *Measured and expected RMS sizes.*

$L = 10cm$			
$\lambda[nm]$	$a[\mu m]$	$\sigma_{teor}[mm]$	$\sigma_{meas}[mm]$
262	20	0.439	0.140
	50	0.176	0.076
	100	0.088	0.055
525	50	0.352	0.210
	80	0.220	0.180
	100	0.176	0.156

RMS sizes are much different from the theoretical predictions. Hence, the effects, described in Chapter 5 play significant role in measuring beams RMS sizes with CCD cameras.

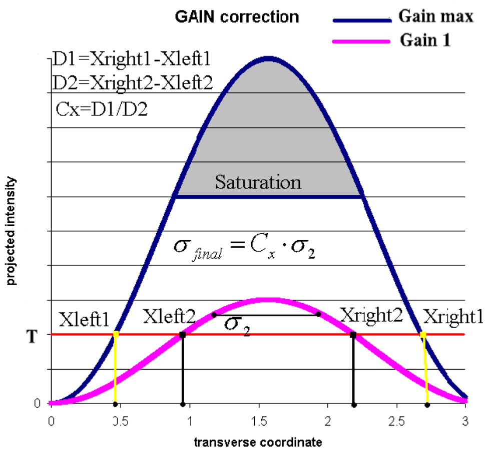

Fig. 11: *Dependance of the measured size on the gain*

7 Possible Solution

In solving the above described problem we assume the following model(Fig.11): initially at Gain 1 we have an intensity distribution visualized at Fig.11 by lower red curve. The CCD camera thereshold T has a certain finite value. When measuring the RMS size of the distribution $I_1(x)$ we obtain data only for the part above the sensitivity level T. Therefore the measured RMS size σ_2 is smaller than the real one. To correct this effect we introduce a correction factor C_x. In order to evaluate C_x one has to set the camera gain to the highest pos-

Tab. 3: *Theoretical test for the gain correction.*

$Thereshold = 20\%Max, \sigma = 1$					
$Gain$	Δ_1	Δ_2	$C_x = \frac{\Delta_1}{\Delta_2}$	σ_2	σ_{final}
3.55	4.79	3.56	1.34	0.83	1.11
7.94	5.42	3.56	1.51	0.83	1.26
17.78	5.99	3.56	1.67	0.83	1.39
39.80	6.50	3.56	1.81	0.83	1.51

Tab. 4: *Theoretical test for the gain correction.*

$Thereshold = 4\%Max, \sigma = 1$					
$Gain$	Δ_1	Δ_2	$C_x = \frac{\Delta_1}{\Delta_2}$	σ_2	σ_{final}
3.55	7.36	0.64	1.11	0.99	1.10
7.94	7.79	0.64	1.17	0.99	1.17
17.78	8.20	0.64	1.23	0.99	1.23
39.80	8.58	0.64	1.29	0.99	1.28

Tab. 5: *Theoretical test for the gain correction.*

$Thereshold = 0.15\%Max, \sigma = 1$					
$Gain$	Δ_1	Δ_2	$C_x = \frac{\Delta_1}{\Delta_2}$	σ_2	σ_{final}
3.55	7.84	7.18	1.09	1.00	1.09
7.94	8.25	7.18	1.15	1.00	1.15
17.78	8.63	7.18	1.20	1.00	1.20
39.80	9.00	7.18	1.25	1.00	1.25

Tab. 6: *Theoretical test for the gain correction.*

$Thereshold = 0.032\%Max, \sigma = 1$					
$Gain$	Δ_1	Δ_2	$C_x = \frac{\Delta_1}{\Delta_2}$	σ_2	σ_{final}
3.55	8.63	8.02	1.08	1.00	1.08
7.94	9.00	8.02	1.12	1.00	1.12
17.78	9.35	8.02	1.17	1.00	1.16
39.80	9.69	8.02	1.21	1.00	1.21

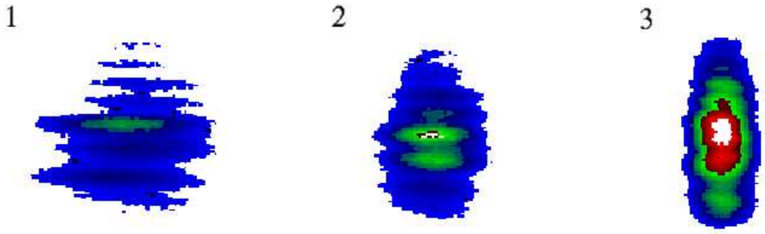

Fig. 12: *Diffraction patterns of UV light after slit 20 μm (1), 50 μm(2), 100(3) μm width*

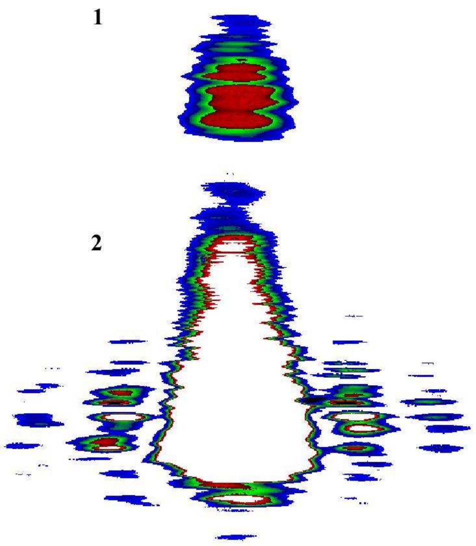

Fig. 13: *Diffraction patterns obtained at (1) Gain = 180 and (2) Gain = Max.*

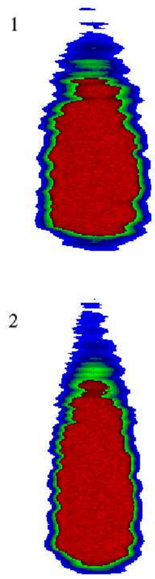

Fig. 14: *Diffraction patterns of UV light after slit 80 μm (1), 100(2) μm width*

sible level. Thus we obtains a new distribution $I_2(x) = GI_1(x)$. $I_2(x)$ is visualized on Fig.11 by the upper blue curve. Here G stands for amplification defined by the cameras gain. In the crossections of $I_2(x)$ with T are X_{L_1} and X_{R_2} and correspondily if $I_1(x)$ intersects T at the points X_{L_2} and X_{R_2} than one defines the value of C_x as:

$$C_x = \frac{X_{R_1} - X_{L_1}}{X_{R_2} - X_{L_2}} \tag{9}$$

The final value for the RMS size is assumed to be the product of σ_2 and C_x:

$$\sigma_{final} = C_x \sigma_2 \tag{10}$$

The above described method for gain correction was tested at first from theoretical point of view. The results for an initial *Gaussian* distribution I_1 are given in Table 3, 4, 5, 6. The same method was tested with real experimantal data, aquired during the experiment described in Chapter 6. The method was applied for the central diffraction maximum of the green light and slit width $a = 50\mu m$ (Fig.13). The parameters of the procedure are as follows:

$$\left.\begin{array}{l} X_{L_1} = 2.435mm \\ X_{R_1} = 4.113mm \end{array}\right\} \Delta_1 = 1.678mm$$

$$\left.\begin{array}{l} X_{L_2} = 2.757mm \\ X_{R_2} = 3.855mm \end{array}\right\} \Delta_2 = 1.098mm$$

$$C_x = \frac{\Delta_1}{\Delta_2} = 1.53mm \qquad (11)$$

$$\sigma_2 = 0.21mm \Longrightarrow \sigma_{final} = 0.32mm \qquad (12)$$

From Table 2 one sees that the theoretical prediction is equal to $\sigma_{teor} = 0.352mm$ The value fot the correction RMS size well agrees with theoretical expectations.

8 Conclusions

If the thereshold (black-level) of the cameras is too high ($>5\%$ of the peak intensity) than the error in direct measuring the beam's RMS size will be intolerably high. In this case the effect described in Chapter 5 of this paper plays significant role. The ideal solution of this problem whould be to reduce the thereshold to much lower value ($<5\%$ of peak intensity). According to Table 4, 5, 6, the error is expected to be less then an 1%. Another possibility is to apply correction of the measured RMS size according to Chapter 7. In this case the RMS size could be over estimated up to 50% (see in Table 3 - 3).

References

[1] F. Stephan *et.al.*, **Photo Injector Test Facility under constraction at DESY Zeuthen**, Proc.FEL2000, Durham, (2000).

[2] CV-M10 Operation Manual, **http://www.jai.com**

[3] M. Born, E. Wolf **Principles of Optics** *Third Edition*, (Pergamon Press, London, 1965).

[4] B. M. Yavorsky, A. A. Detlaf, Moscow, **Handbook of physics** *Nauka*, (1977).

Measurements of Electron Energy Deposition in the HERMES Silicon Recoil Detector (1 GeV-6 GeV)

Eric Switzer
University of Chicago
erswitze@uchicago.edu

The first prototype module for the Hermes Silicon Recoil Detector (SRD) shows that energy deposition is Landau-distributed, and the test beam II results with the a micro vertex module (ZEUS) indicate that the Landau distribution stays essentially fixed across the energies 1 GeV to 6 GeV. This is because collisional energy losses dominate charge deposition and depend very little on electron energies 1 GeV-6 GeV. Despite the impact of Bremsstrahlung in overall energy loss over this range, its contribution is only $(9.0 \pm 0.1) \times 10^{-5}$ *in* 300 μm *silicon. By adjusting the beam II beam energy and comparing with models, we determine that the energy deposition mechanism is best described by a truncated Bethe-Bloch form with a radiative (Bremsstrahlung) correction. In the TIGRE, charge clustering is not observed, but is a large effect in the micro vertex module and must be accounted for. The results of this study are presented in this report.*

1 Introduction

The TIGRE silicon strip detector will be implemented in the HERMES silicon recoil detector (SRD) to measure relatively low energy recoil protons in the 1-70 MIP (corresponding to 7 MeV to 1.5 GeV) range. The HERMES SRD will extract kinematic information about the recoil protons from pulse heights, so it demands a detailed understanding of energy loss mechanisms and a calibrated output [12]. Preliminary tests of the HELIX readout amplifier and TIGRE strip detector are based on charge injection [4] and electron beam tests [5].

The TIGRE detector [12] has 128 silicon strips in a junction configuration. These strips are read out separately through high and low gain channels in anticipation of a high dynamic range (1-70MIP). Charge injection tests [4] have verified the high and low gain channels, and a beam test is necessary to study cross talk and noise of the entire detector. Beam tests of the TIGRE boards with the 1 GeV to 6 GeV electrons from a parasitic beam of the DESY II ring in Hamburg will represent the response of the TIGRE/HELIX in the 1 MIP range.

Protons and other massive particles passing through silicon have a dE/dx parameterized by the Bethe-Bloch form that is dominated by collisional effects at these low energies. For less massive particles, like electrons, Bremsstrahlung loss must be considered at relatively low energies. Electrons and positrons in the 1 GeV to 6 GeV range are bent by the nuclear charge centers of the target, and because of their low mass, will radiate most of their energy. Nearly all of this energy is radiated out of the silicon and can not be registered by the junction; the effect is on the order of 3% of the total ionization signal at 6 GeV, and much less at 1 GeV. Total energy loss is not equivalent to the total energy deposit.

Charge deposition in the form of electron-hole pairs is registered by a reverse-biased, fully depleted, silicon pn junction. We measure the charge deposition properties in two types of detectors, 1) the wide-pitch TIGRE detector, planned for the HERMES recoil detector, and 2) the fine-pitch ZEUS microvertex detector, already tested and employed by ZEUS. The TIGRE and ZEUS microvertex detector are read out by the HELIX chipset.

2 Bethe-Bloch and the Landau distribution

2.1 Energy loss versus energy deposit

An electron beam with energy E traveling through silicon ($Z = 14$) will lose energy by two major processes, collisional (ionization processes), and radiative (Bremsstrahlung), in the ratio: [7]

$$\frac{dE_{radiative}/dx}{dE_{collisional}/dx} \approx \frac{EZ}{1600 m_e c^2}$$

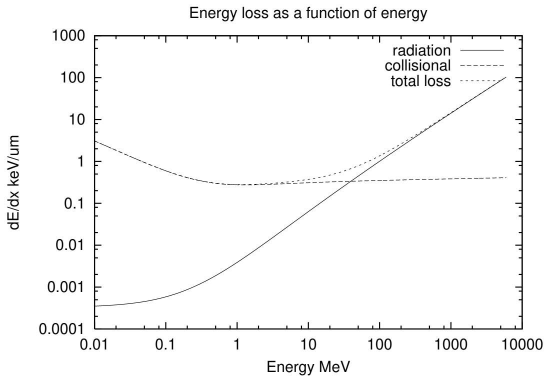

Fig. 1: *Total average energy loss in silicon as a function of beam energy, indicating that radiative effects dominate at higher energies.*

In a 1 GeV electron test beam this ratio is ≈ 17, and much higher at 6 GeV. The electrons *lose* most of their energy in silicon by radiative processes. Unlike the collisional process, where the electrons immediately form electron-hole pairs and give signals, the Bremsstrahlung photons have a low reabsorption probability in the silicon that depends on their energy and the silicon's thickness. Though an electron has fixed energy, the Bremsstrahlung photons it generates have a continuous intensity spectrum, $I(\omega)$. For the bending of an electron around the charge of the silicon nucleus with electron shielding (Thomas-Fermi in a gas) is: [9] (plotted schematically in figure 2)

$$I(\omega) = \frac{e^2}{3\pi\epsilon_o c^3}|\dot{v}(\omega)|^2 \Rightarrow I(\omega) = \frac{Z^2 e^6 N}{12\pi^3 \epsilon_o^3 c^3 m_e^2 \gamma} ln\left(\frac{192\beta}{Z^{1/3}}\right)$$

$$\text{for } E < (\gamma - 1)m_e c^2$$

This means that a Bremsstrahlung photon has a (theoretically) equal probability to have any energy from 0 to $(\gamma - 1)m_e c^2$. A photon of a given energy has a well-known reabsorption cross section in silicon (with photo, Compton and pair components) σ_{tot}. Defining the reabsorption probability $f(E)$ for photons (energy $= E$) traversing a solid of thickness ℓ, with equal probability of being generated anywhere in the solid, (figure 3)

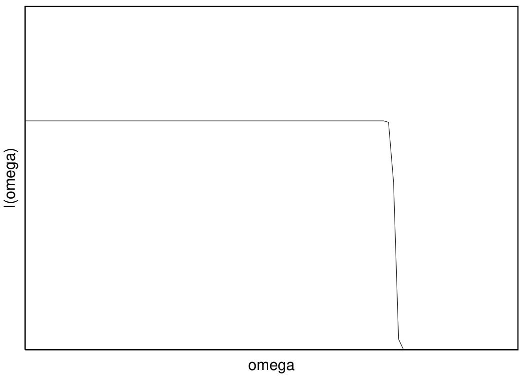

Fig. 2: *Schematic drawing of the Bremsstrahlung spectrum for a with energy cutoff $(\gamma - 1)m_e c^2$, it is roughly constant.*

$$f(E) = \frac{I_{absorbed}}{I_{initial}} = \frac{1}{\ell}\int_0^\ell \left(1 - \exp\left\{\frac{-N_A \sigma(E)\rho x}{A}\right\}\right)$$
$$= 1 - \frac{1}{\ell\mu}(1 - e^{-\mu\ell})$$

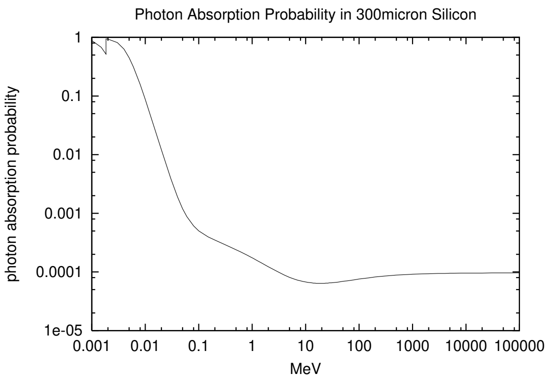

Fig. 3: *Low energy Bremsstrahlung photons have a much higher absorption probability in the solid, but the spectrum is dominated by photons above 1MeV, so the overall energy absorption is small. $\sigma(E)$ is provided by the Xcom simulation (physics.nist.gov/cgi-bin/Xcom/). The notch at 0.001 MeV is due to shell effects.*

Where $\mu = N_A \sigma(E)\rho/A$. Integrating $f(E)E$ over the Bremsstrahlung spectrum gives the percent of radiant energy that is reabsorbed in the silicon, Λ. To simplify the calculation, the photon absorption cross section is nearly flat across the energy ranges in question above ≈ 1 GeV, by the Xcom simulation, 1.60 b/atom. [2] Especially below 1keV, the cross sections are orders of magnitude larger and must be treated numerically.

$$\Lambda = \int_0^{(\gamma-1)m_e c^2} f(E) E dE \bigg/ \int_0^{(\gamma-1)m_e c^2} E dE$$

Numerical integration shows that this correction factor is $(9.0 \pm 0.1) \times 10^{-5}$, with error due to uncertainties in the physical constants of the silicon. This means that, while Bremsstrahlung is on the order of 17 times larger than collisional processes, the effect is greatly diminished because most of the γ escape.

2.2 *Radiative dE/dx*

All of the models that we employ include a Λ-corrected radiative loss term. For an electron of E in the silicon, $\frac{dE}{dx}$ is approximated by: [7]

$$\frac{dE_{brem}}{dx} = \Lambda \left(\frac{e^2}{\pi \epsilon_o} \right)^2 \frac{Z^2 N_A E \rho}{137 m_e^2 c^4 A} \left[4 \ln \left(\frac{2E}{m_e c^2} \right) - \frac{4}{3} \right]$$

Where N_a is Avagadro's number, and Z is the proton number. The relation between β^2 and kinematic parameters ($E = T + m_e c^2$, p) is

$$\beta^2 = \frac{p^2}{\gamma m_e c} = \frac{c^2 p^2}{E^2} = \frac{E^2 - m_e^2 c^4}{E^2}$$

2.3 *Model 1: Standard Bethe-Bloch with Radiative Deposit*

In the regime 1 GeV-6 GeV, density corrections play an important role in the collisional cross section. [8] In their absence at 6 GeV, the expectation is incorrect by 50% for collisional energy loss estimates. Grupen (with density modification from Leo) gives the energy loss: [6]

$$\frac{dE_{coll}}{dx} = -4\pi N_A r_e^2 m_e c^2 \rho \frac{Z}{A\beta^2} \left[\ln \left(\frac{\gamma m_e c^2 \beta \sqrt{\gamma - 1}}{I\sqrt{2}} \right) + \right.$$

$$\left. \frac{1}{2}(1-\beta^2) - \ln(2)\frac{2\gamma - 1}{2\gamma^2} + \frac{1}{16}\left(\frac{\gamma - 1}{\gamma} \right)^2 - \frac{\delta}{2} \right]$$

With the parameters,

Z	integer charge of target particles
A	atomic mass of target
I	mean excitation energy in target (173.0eV for Si)
X	$\log_{10}(\beta\gamma)$

Where δ is empirically determined for silicon,

$$\delta = \begin{cases} 0 & X \leq 0.20 \\ 4.6052X - 4.44 + 0.1492(2.87 - X)^{3.25} & 0.20 < X < 2.87 \\ 4.6052X - 4.44 & X \geq 2.87 \end{cases}$$

For a thin solid and energies in the nearly linear high energy range, the energy deposit is given by $dE/dx \Delta x$. Total most probable energy loss as a function of beam energy for this model is plotted in figure 4, for 1 GeV-6 GeV.

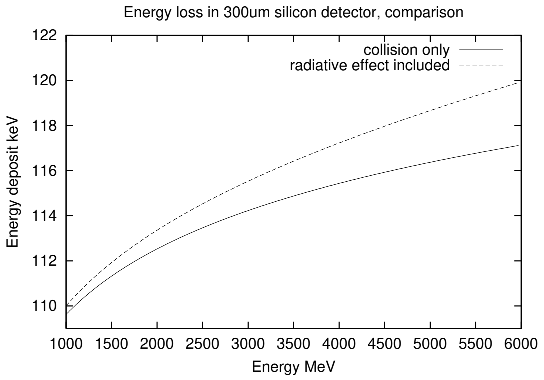

Fig. 4: *Most probable energy deposited in 300μm silicon in the ordinary BB model (model 1); though Bremsstrahlung is a very weak deposition effect in the thin solid, it can be registered as a 3% deviation at 6 GeV.*

2.4 *Model 2: Truncated Bethe-Bloch with Radiative Deposit*

Just as the Bremsstrahlung photons have a low reabsorption over the volume of the silicon, the electrons produced in collisional events may not be reabsorbed in the solid, and even if they are, the energy deposit may not be registered because is spans many channels. This is an effect applicable to finite (effectively small) volume detectors. [13] Knock-on electrons at high energies give an effective cutoff T_{cut}, above which recoil electron energy will not be deposited in the silicon. [14] Writing the truncated form,

$$\frac{dE_{coll}}{dx} = -4\pi N_A r_e^2 m_e c^2 \rho \frac{Z}{A\beta^2} \left[\frac{1}{2} \ln \left(\frac{2 m_e c^2 \beta^2 \gamma^2 T_{upper}}{I^2} \right) \right.$$

$$-\frac{\beta^2}{2}\left(1+\frac{T_{upper}}{T_{max}}\right)-\frac{\delta}{2}\Bigg]$$

Where $T_{upper} = \min(T_{max}, T_{cut})$ and

$$T_{max} = \frac{\gamma^2\beta^2 m_e c^2}{1+\gamma}$$

The reabsorption probability is more difficult to calculate because the knock-on electrons have a wider angular distribution (so they traverse different lengths in the silicon) and have a more complicated energy spectrum than the Bremsstrahlung photons. As Yamamoto points out, the T_{cut} parameter only changes the "offset" of the dE/dx curve, but not the shape of the curve. Calibration studies for the conversion of analog to digital converter (ADC) count to particle energy *must* take this offset into account in the regime 1 GeV to 6 GeV. However, without this calibration data now, we can not discriminate differences in the T_{cut} parameter for reasonable values. Figure 5 shows a summary of the models, and figure 6 shows the importance of radiative corrections in the truncated model.

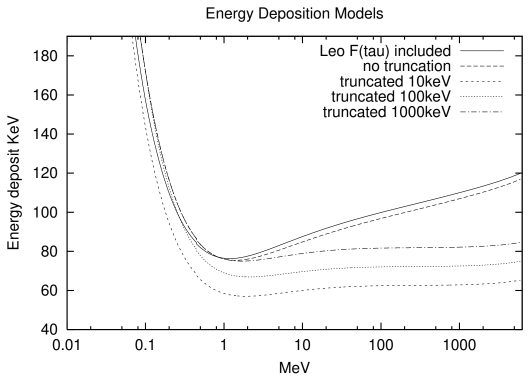

Fig. 5: *Most probable energy loss for several different truncation models.*

2.5 Most Probable Energy Deposition

In a thin absorber, the central limit weakly applies to the area around the maxima of energy deposition, but the entire distribution is no longer Gaussian–it has a long tail. This is because of large fluctuations in the number of collisions. Some particles will collide with higher frequency, lose energy, collide more and more frequently, and deposit more energy. This process is characterized by the Landau distribution. [6] A reasonable approximation is Moyal's, [10]

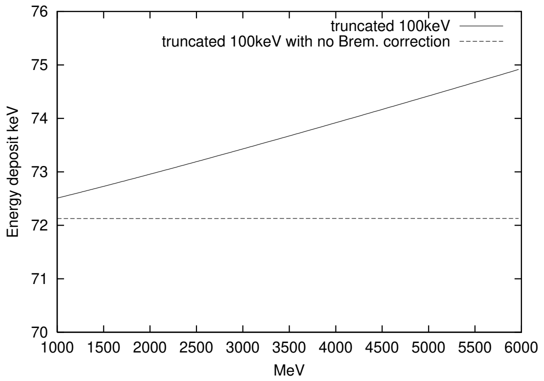

Fig. 6: *Most probable energy loss for a 100keV truncation model with and without the Bremsstrahlung loss term. Note that with truncation, the energy loss is literally flat across the energy range, and it is only the radiative term that leads to a small increase. Plotting this over the energy range 0.01 MeV, to 6 GeV, the radiative loss correction is nearly invisible.*

$$L(\lambda) = \frac{1}{\sqrt{2\pi}}\exp\left(-\frac{1}{2}(\lambda + e^{-\lambda})\right)$$

Where

$$\lambda = \frac{\Delta E - \Delta E_p}{\zeta}$$

$$\zeta = 2\pi N_A r_e^2 m_e c^2 z^2 \frac{Z}{A\beta^2}\rho x$$

E_p, the most probable energy is the mean of the equation in λ, $E_p = -\zeta\langle\lambda\rangle + \langle\Delta E\rangle$ and $\langle\Delta E\rangle$ is given by the Bethe-Bloch form. Integrating λ

$$\langle\lambda\rangle = \int_{-\infty}^{\infty}\lambda L(\lambda)d\lambda = \gamma + \ln(2) \approx 1.27036$$

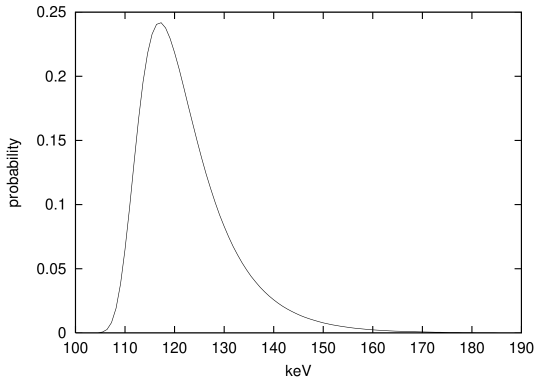

Fig. 7: *Landau distribution for most probable energy deposition 117 keV in 300μm silicon.*

3 Reverse Bias and Junction Capacitance

3.1 Reading out the charge deposition

Energy loss in a solid will create a large number of electron-hole pairs. These pairs are separated in the depletion region— electrons travel to the n side, holes to the p side. The HELIX amplifier reads pulse heights from the n or p sides of the TIGRE strip detector. The pulse heights are maximized by maximizing the depletion region width (and minimizing the area where electron-hole pairs can recombine in the solid). This is done by applying a reverse bias.

Reverse bias in pn junction refers to a negative voltage applied to the n-type cathode. A reverse bias increases the potential across the junction and depletes the region around the junction of its mobile carriers–it widens the depletion region. The reverse bias needed to fully deplete a junction is related to the device scales and the acceptor/donator number densities.

A nice argument (due to Mott-Schottky) relates the depletion region width to the junction capacitance. [1] This way, the depletion region width can be measured easily through capacitance. (See appendix for a derivation)

$$C(V) = \frac{\epsilon_{Si}}{\ell(V)} = \sqrt{\frac{e\epsilon_{Si}N_aN_d}{2(N_d+N_a)(V_o-V_{ext})}}$$

Where V_o is the internal potential and N_a, N_d are the acceptor and donor number densities, respectively. Because of internal potential V_o, a 0 bias p-n junction does not have infinite capacitance.

3.2 Measurements

A probe station with needles contacting the silicon structure's output pads can apply a reverse bias and read off the capacitance. This was conducted in the DESY-Zeuthen silicon lab with an automated data acquisition system.

In $1/C(V)^2$, the relation to V is linear, so by plotting this (figure 9) for test structure 1150-18 and fitting a line, the intercept gives V_o and slope gives information about carrier concentration. Also, based on the capacitance, the depletion region width can also be measured (figure 8). This indicates that at zero applied voltage, the thermal diffusion extends over $(78 \pm 3)\mu m$ from the junction site. In addition, the depletion region can not be forced to extend much further than $241\mu m$, roughly the order of junction thickness.

The measurements are of test structure 1150-18, not with the actual TIGRE junctions out of safety precaution, but the general process of finding the depletion voltage is identical. For the test structure:

(maximum) depletion voltage	$(19 \pm 2)V$
width of maximum depletion region	$(241 \pm 15)\mu m$

[1] The simplifying assumption here is the "full-depletion limit", where the depletion region's boundaries are sharply defined, and the p-n junction is infinitely sharp. In reality, the depletion region is thermally broadened, and the pn junction itself has characteristic width. This approximation is valid at normal operating temperatures, and for uniformly doped junction layers.

4 Noise and Data

The TIGRE detector is connected to a fan-out that divides the charge in each strip in to a high and low gain channel. In the test device at the time of test beam I, three couplings are available, none, 10pF, 22pF. However, [4] and [5] plan further tests with 5pF coupling. The coupling fanout is bonded to a board with 4 HELIX128 chips [3]. This amplifier and data acquisition scheme has several sources of noise that must be processed out of the test data.

4.1 Noise Processes and Subtraction

Noise falls in to three domains: a constant offset that depends on the channel ($\text{Offset}_{channel}$), an offset on all channels that depends on time ($\text{CMN}(t)$), and a Gaussian noise process that varies with time and channel, ($\text{Noise}(t)_{channel}$).

$$\text{Output}(t)_{channel} = \text{Signal}(t)_{channel} + \text{Offset}_{channel} + \text{Noise}(t)_{channel} + \text{CMN}(t)$$

The first two noise terms are simple to subtract, but $\text{Noise}(t)_{channel}$ must remain in the final signal and be subtracted by a Gaussian fit. Outlining common mode and offset subtraction:

Time is discretely parameterized by trigger number, $t \in \{1...N_{events}\} = T$, and the output channels range from 1 to 512. With pedestal run data, the beam is inactive, and $\text{Offset}_{channel}$ is just the average (because Gaussian noise is centered around zero), so that the offset per channel is just the average:

$$\text{Offset}_{channel} = \frac{1}{N_{events}} \sum_{t=1}^{N_{events}} \text{Output}(t)_{channel}$$

In the amplifier configuration [3] silicon strips are read out through four amplifiers $C_1 = \{1...128\}$, $C_2 = \{129...256\}$, $C_3 = \{257...384\}$, $C_4 = \{385...512\}$. We will work under the assumption that common mode noise is only common to one amplifier block.

With the beam on, there is a subset of channels on each chip at each time where $\text{Signal}(t)_{channel} \approx 0$; a channel where no electron hole pairs are excited. Let H_i = channels in the given amplifier chip such that $\text{Signal}(i)_{channel} \approx 0$. The common mode noise at each time is then,

$$\text{CMN}(i) = \frac{1}{\sharp H_i} \sum_{channel \in H_i} (\text{Output}(i)_{channel} - \text{Offset}_{channel})$$

To perform this subtraction, the analysis software must know what constitutes $\text{Signal}(t)_{channel} = 0$ on top of a Gaussian noise process. σ exclusion must be high enough that noise is not recognized as a signal and excluded the subtraction, but low enough so that signal events are excluded. At $> 3\sigma$, 99.73% of Gaussian noise events are excluded. This is an effective cutoff. [5]

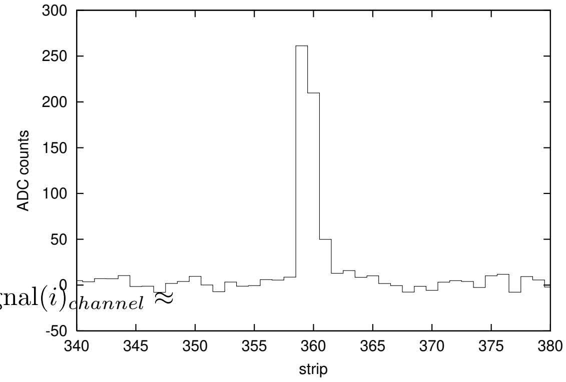

Fig. 8: *An anti-symmetric charge deposition event with two main activations.*

4.2 Clustered Charge Deposition–ZEUS detector module

When a charged particle passes through the junction, it may deposit a charge trail that extends over several strips in a detector with fine pitch-width. The full width at half maximum of the charge trail is roughly 10μm. [11] Figure 10 shows a large anti-symmetric charge deposition, and 11 shows a relatively symmetric deposition over several channels in one event in the ZEUS Micro Vertex Detector during the test beam II.

This effect must be accounted for in the event analysis to recover the Landau distribution. In the relatively symmetric deposition above, the ADC bins 190, 330, and 520 would be incremented in the analysis software, even though in reality the total charge deposit in that event is of order 1040 ADC counts. A simple summation-over-neighboring channels over 3σ (head-tail algorithm) works well to separate the events from

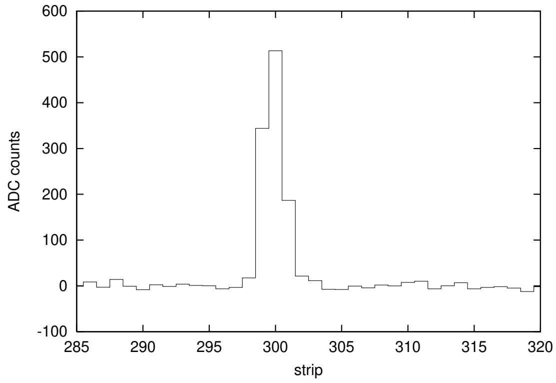

Fig. 9: *A relatively symmetric deposition over a larger area.*

the noise, and a complicated cluster analysis is not necessary.

5 Beam Tests

The DESY II ring stores a fixed-energy beam that provides the test areas in Halle 2 with variable energy electrons by a conversion process. The ring electrons travel through a carbon fiber and generate Bremsstrahlung photons in the process described earlier. These photons travel downstream to a target where they pair produce in a magnetic field that fans out into electrons and positrons of a wide energy range. These are selected (from 1 GeV to 6 GeV) into the test beampipe by a bending magnet. The device under test (either the TIGER or MVD with HELIX module) is held in a xy table with adjustable angle along the beam's path in the test area. Triggering is threefold, performed by a horizontal and vertical finger-counter in the front and another in the rear of the detector. Triggers coincident with the HERA clock (physics triggers) begin the HELIX readout through an ADC. The VME and storage are controlled from a shielded control room with LabView. Triggering, latencies, beam energy, and collimator settings are also operated remotely in the control room.

5.1 Beam test 1 - TIGRE: the Landau curve and effect of charge coupling

Test beam I dealt with the TIGRE, the wide-pitch junction detector planned for the HERMES recoil detector. The xy table allowed the TIGRE to move and accept the electron beam through strips that are read out with differing amounts of coupling capacitance (charge division, figure 13). See [4] for information on the wide dynamic range available through charge sharing. Because of the wide pitch, no cluster analysis is needed, and the detector immediately gives a Landau feature in the ADC histograms as a function of coupling capacitance. (figure 14) By subtracting the Gaussian, a the Landau feature is recovered. (figure 15). The data from Beam test I also corroborate the charge injection tests and the application of charge division [5].

5.2 Beam test 2 - ZEUS: clustering, cross section as a function of energy

Because the ZEUS MVD's fine pitch, the $\approx 1cm$ wide DESY II electron beam spreads electron hits over 85 channels, shown in figure 16. The fine pitch also allows two, three, and or more strips to be activated due to one electron charge deposition. The correction is described in the section “Data and Noise”. Without the charge clustering correction, the signal pulses per strip give a broadened and washed-out Landau curve (figure 17), because the entire event pulseheight is not histogrammed, just several fractions of it. Figure 18 shows the ADC count histogram after summing over neighbors.

There are three process that maximize the signal to noise ratio: adjusting the position of the beam (to hit the silicon target and avoid dead areas), adjusting the latency, and adjusting the reverse bias voltage. The beam positioning is relatively straightforward, and the reverse bias voltage is known from device parameters and probe table studies, but latency is a free parameter.

It takes a finite amount of time for the HELIX and downstream components to process the data, so if it is requested too soon or too late, the recorded data has a deficit of ADC counts (figure 19) because it does not trigger on the maxima of the input data pulse. The optimal value of readout latency pushes the Landau out to higher ADC counts, away from the Gaussian feature, thereby increasing signal to noise ratios.

After maximizing the output ADC counts, the beam energy was changed from 1 GeV to 4 GeV, then to 6 GeV to study energy deposition. At both 4 GeV and 6 GeV, the Landau distribution has a surplus of counts at the low end, so immediate fits to a Landau distribution are shifted to lower ADC counts. However, by fitting from the area around the peak of the Landau to the tail, much better χ^2 values are achieved. By plotting these observed most probable peaks (and models scaled to ADC counts), we have figure 12. Uncertainties listed are in the fitting parameters–they are presumed to be only statistical errors. These results show that the truncated Bethe-Bloch form best parameterizes the data, and that the small Λ-corrected radiative term is needed to explain a nearly linear 2% increase from 1 GeV to 6 GeV.

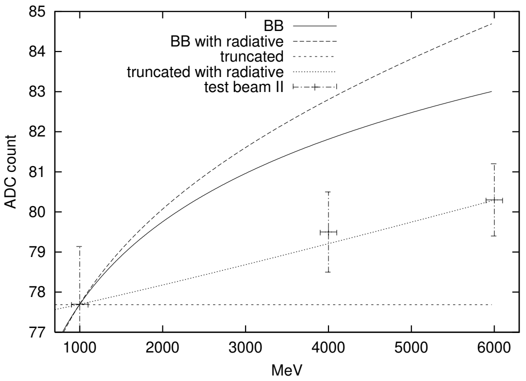

Fig. 10: *The energy deposition as a function of beam energy for several models. Test beam II data shows that a truncated BB with radiative loss terms (although small) gives the best model from 1 GeV to 6 GeV. Because there is no calibration between energy deposition and ADC count, these models are scaled to all match with 1 GeV data.*

6 Conclusion

Data from the two Hamburg test beams of the TIGRE with HELIX DAQ validates several expectations of energy deposition in silicon. We have shown a Landau distribution of energy deposition with a slightly larger spread than expected (due to multiple absorbers in test setup). The noise processes show an expected Gaussian behavior and offsets, common mode and white noise can all be subtracted in the offline analysis. After an optimization of ADC counts per event to increase the signal to noise ratio (latency and charge cluster analysis), we investigated the energy deposition behavior over a range of energies 1-6 GeV. These results show that a truncated Bethe Bloch form with a Λ corrected Bremsstrahlung term parameterize the energy loss from 1 GeV to 6 GeV. Further, the data from test beam II show the necessity for the inclusion of truncated energy deposition models in ADC count $\leftrightarrow$ kinematic calibrations in the Silicon Recoil Detector.

7 Acknowledgements

I would like to thank the HERMES Silicon RD group and DESY for letting me be involved in the project over the summer 2002–It's been a wonderful experience. Ingrid, thank you for all the help and explanations...the test beam was only a little painful. Arne, thanks for the suggestion about the truncated Bethe-Bloch form!

8 Figures and Histograms

8.1 Test Beam I

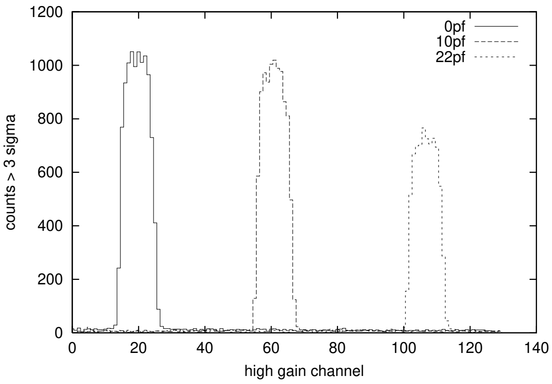

Fig. 11: *A sum of all hits in each high gain channel over 3σ for each stage of the beam test. Each region represents the width of the DESY II electron beam.*

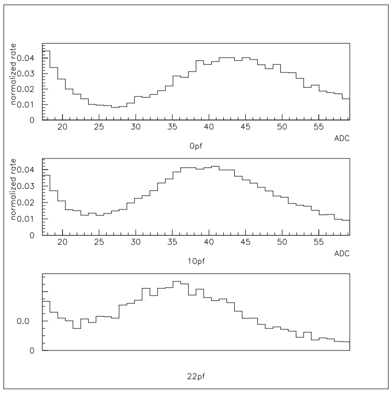

Fig. 12: *Histograms comparing the role of capacitive coupling on the output amplitude. With charge coupling turned off, the signal (Landau) to noise (Gaussian) ratio is highest.*

8.2 Test Beam II

References

[1] Bart. *PN Junctions.* World Wide Web, http://ece-www.colorado.edu/ bart/book/pndiode.htm.

[2] Berger et al. *Xcom simulation.* World Wide Web, http://physics.nist.gov/cgi-bin/Xcom/.

[3] Feuerstack-Raible et al. Helix128-x user manual. Technical report, NIKEF, 1999.

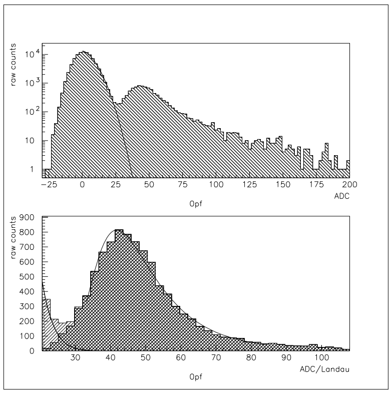

Fig. 13: *Test Beam I: By first identifying the Gaussian feature (top) and subtracting it, the double-hashed Landau curve remains (bottom).*

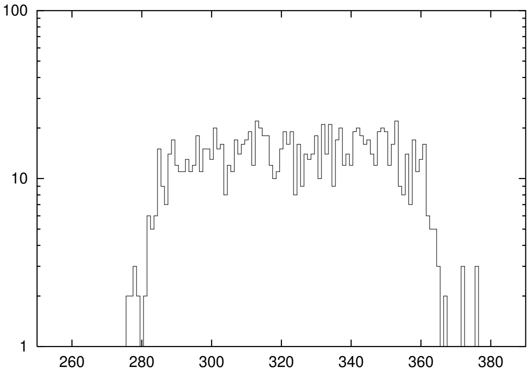

Fig. 14: *Test Beam II: Hitlist in the ZEUS module, showing the large number of active strips at 5 sigma as a function of ADC channel.*

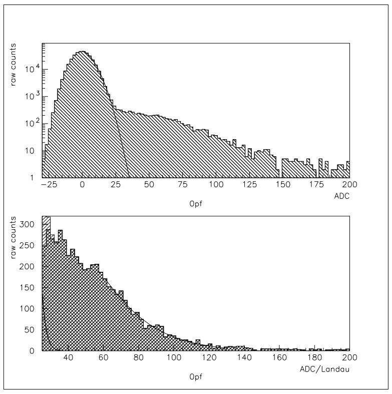

Fig. 15: *Test Beam II: Raw signal before clustering correction. The Landau is broadened and mangled by finite-width charge deposition on a fine-pitch detector. This is not seen in the larger TIGRE detector.*

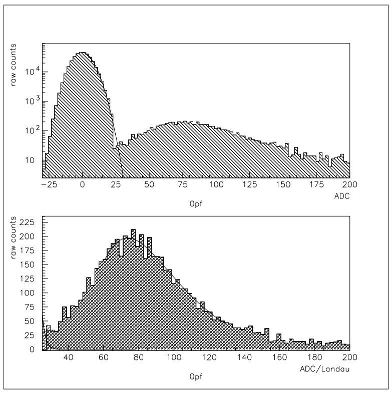

Fig. 16: *Test Beam II: Histogram after clusters events of the two nearest neighbors have been folded into the signal.*

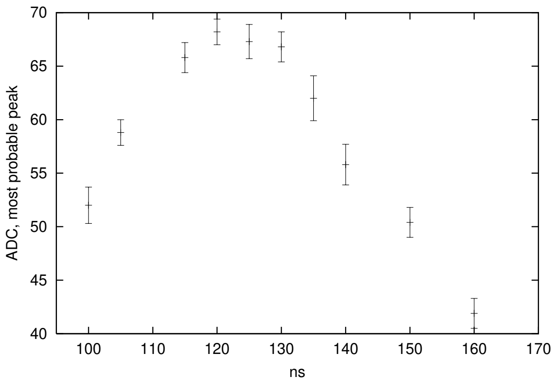

Fig. 17: *Test Beam II: The ADC count is optimized when the latency of 120ns is added to the normal 36 clock-cycle latency of the HELIX readout.*

[4] M. Kopytin et al. Decision on the readout chip for the new hermes silicon recoil detector. Technical report, DESY-Zeuthen, 2002.

[5] Gregor et at. Test-beam results of a first prototype for the hermes silicon recoil detector. 2002.

[6] Grupen. *Particle Detectors.* CUP, Cambridge, 1996.

[7] Krane. *Introductory Nuclear Physics.* Wiley, New York, 1988.

[8] Leo. *Techniques for Nuclear and Particle Physics Experiments: A How-to Approach.* Springer-Verlag, Berlin, 1994.

[9] Longair. *High Energy Astrophysics.* CUP, Cambridge, 1992.

[10] Moyal. Theory of ionization fluctuations. *Phil. Mag.*, 1955.

[11] Peisert. Silicon microstrip detectors. Technical report, INFN, Padova, 1992.

[12] Stewart. The hermes recoil detector. Technical report, DESY, 2002.

[13] Arne Vandenbroucke. *private communication.*

[14] Yamamoto. Energy loss particle identification for collider detectors. Technical report, Dept. of Physics and Astronomy UHawaii.

Fast Beam Diagnostics through Beamstrahlung at TESLA

Marko Ternick
DESY Zeuthen
Platanenallee 6, 15738 Zeuthen, Germany
Email: Marko.Ternick@desy.de

Version 1
5. September 2002

To adjust the beams of the TESLA linear collider at high luminosity, fast beam diagnostics are needed. In other words, one has to measure the beam parameters within one bunch spacing of a few hundred nanoseconds. We use energy distributions of e^+e^- pairs created by beamstrahlung. These distributions depend strongly on beam parameters like horizontal and vertical beam size. A way to reconstruct these beam parameters is shown here. Numerical results are calculated for TESLA but the technique is equally valid for all other linear colliders. This report summarizes my work as a summer student at DESY Zeuthen.

1 Introduction

At circular e^+e^- colliders one of the main problems is synchrotron radiation because is a big source of energy loss. To avoid this, linear accelerators are planned, such as JLC in Japan, NLC in the U.S. and TESLA in Germany. Linear colliders have another big drawback - one can use the beams only once. Therefore, one has to increase the luminosity to get reasonable high event rates. The luminosity is defined as [1]

$$\mathcal{L} = \frac{1}{4\pi}\frac{f_{rep} n_b N_e^2}{\sigma_x \sigma_y} \times H_D, \tag{1}$$

where
f_{rep} is the pulse repetition frequency,
n_b is the number of bunches per pulse,
N_e is the number of electrons (positrons) per bunch,
$\sigma_{x,y}$ is the horizontal (vertical) beam size at interaction point and
H_D is the disruption enhancement factor (typically $H_D \approx 2$).

To increase the luminosity one can for example increase the repetition frequency, the number of bunches or the number of particles within one bunch. Another way is to decrease the beamsize σ_x or σ_y. But for very small bunches the electric field becomes so large that the disturbing effects on the electron and positron bunches can not be neglected. In this way electrons are accelerated towards the center of the positron bunch, and vice versa. This is known as the pinch effect. On the one hand this is very good because it increases the luminosity by a factor H_D of approximately two. This factor is often called disruption enhancement. On the other hand, accelerated charged particles emit photons. This radiation is called beamstrahlung and was first observed at SLAC [4]. The average fractional beam energy loss due to beamstrahlung is [1]

$$\delta_E \approx 0.86 \frac{r_e^3 {N_e}^2 \gamma}{\sigma_z(\sigma_x + \sigma_y)^2}, \tag{2}$$

where
r_e is the classical electron radius and
γ is the relativistic factor E_{beam}/m_0c^2.

By choosing $\sigma_x \gg \sigma_y$, the energy loss δ_E becomes independent of the vertical beamsize σ_y. So we can increase the luminosity by decreasing the vertical beam size without increasing the energy loss at the same time. The relation $\sigma_x \gg \sigma_y$ means we use flat beams. This is planned at all future linear colliders with a ratio $R = \frac{\sigma_x}{\sigma_y} \approx 100$. [1] [2] [3]

2 LCAL at TESLA Detector

Beamstrahlung follows almost the direction of the electrons and positrons with a very small angle with respect to the beam axis typically a few mrad [5]. For this reason most of the photons are hidden in the beampipe and it is not easy to detect them. But if the photons are highly energetic, i.e. photons with an energy above one MeV, they will create e^- e^+ pairs in the field of the bunch. Due to electromagnetic repulsion electrons (positrons) are deflected to larger angles in positive (negative) z-direction. In the TESLA-Detector these particles can be studied at the so-called LCAL (Luminosity CALorimeter). It will cover a range from 6 mrad to 28 mrad and will be located at a distance of 220 cm on both sides of the interaction point [6].

Figures 1 to 6 show the normalized energy distribution for different beam parameters.[1] The circle in the figures is the outer radius of the beampipe. One can see the energy distribution for the standard TESLA setup and energy distributions for different beam parameters. Obviously, with changed beam parameters the distributions becoming different. For example a somewhat longer bunch will result in a smaller maximal radius (figure 3) and a bunch with an angle in the x-z plane will result in a different angular distribution (figure 4).

To characterize the distribution at LCAL we have defined special quantities: the average radius, energy and arrival time which will referred to hereafter as observables.

The average radius is defined as:

$$\bar{r} = \sum_i r_i E_i, \tag{3}$$

where the sum runs over all pixels with radius r_i bigger than the beampipe radius of 12 mm and pixel energy E_i.

The average energy is:

$$\bar{E} = \frac{E}{N}, \tag{4}$$

where
E is the total energy and
N is the number of particles.

The arrival time is:

$$\bar{t} = \frac{\sum_i t_i}{0.9N}, \tag{5}$$

where the sum runs over the central 90% of the distribution. We have chosen to use a truncated mean because a very small fraction of extremely late particles would shift the average value by a factor of order ten.[2]

3 The Mathematics

Now we can vary some beam parameters and see how the observables change. In figure 7 to 12 the change of the observables $\bar{r}$, $\bar{E}$ and $\bar{t}$ is shown in dependence of the parameters σ_x and σ_z. The vertical line corresponds to the TESLA standard value. In the diagrams, you can see fitting curves $f_{\bar{r}}(\sigma_x, \sigma_z)$, $f_{\bar{E}}(\sigma_x, \sigma_z)$ and $f_{\bar{t}}(\sigma_x, \sigma_z)$. You can also see that these curves are different for example for the energy. We can expand the functions in a Taylor series:

$$\begin{aligned}\bar{E} = f_{\bar{E}}(\sigma_x, \sigma_z) &= f_{\bar{E}}(\sigma_{x_0}, \sigma_{z_0}) \\ &+ \frac{\partial f_{\bar{E}}}{\partial \sigma_x}(\sigma_x - \sigma_{x_0}) + \frac{\partial f_{\bar{E}}}{\partial \sigma_z}(\sigma_z - \sigma_{z_0}) \\ &+ \ldots,\end{aligned} \tag{6}$$

where
$f_{\bar{E}}(\sigma_{x_0}, \sigma_{z_0}) = \bar{E}_0$ is the energy average for standard TESLA parameters. The partial derivatives are obtained from the slopes of the fitted functions near the TESLA standard parameter values.

We can do a similar expansion for $\bar{t}$ and $\bar{r}$ to get the matrix equation (to first order)

$$\begin{pmatrix} \bar{E} - \bar{E}_0 \\ \bar{t} - \bar{t}_0 \\ \bar{r} - \bar{r}_0 \end{pmatrix} = \begin{pmatrix} \frac{\partial f_{\bar{E}}}{\partial \sigma_x} & \frac{\partial f_{\bar{E}}}{\partial \sigma_z} \\ \frac{\partial f_{\bar{t}}}{\partial \sigma_x} & \frac{\partial f_{\bar{t}}}{\partial \sigma_z} \\ \frac{\partial f_{\bar{r}}}{\partial \sigma_x} & \frac{\partial f_{\bar{r}}}{\partial \sigma_z} \end{pmatrix} \begin{pmatrix} \sigma_x - \sigma_{x_0} \\ \sigma_z - \sigma_{z_0} \end{pmatrix}$$

or

$$b = Ax \tag{7}$$

This overdetermined system is not trivial to solve because a rectangular matrix can not be

[1] The simulations are done with Daniel Schulte's GUINEA PIG [7].

[2] The number of particles N is not measureable (since there are in the order of 10^4). This is only to show how the basic technique works.

inverted in the usual way. So we use the generalized matrix inverse of Moore and Penrose[8] which has a very nice property: for a given system $b = Ax$, the shortest length least squares solution is $x = A^{+}b$. We can calculate the inverse in the following ways

$$A^{+} = (A^{T}A)^{-1}A^{T} \tag{8}$$

if $A^{T}A$ is invertible or

$$A^{+} = A^{T}(AA^{T})^{-1} \tag{9}$$

if AA^{T} is invertible.

As a proof of the principle we simulated with GUINEA PIG a bunch of width $\sigma_x = 600\ nm$ and length $\sigma_z = 250\ \mu m$. Please have in mind that the TESLA standard parameter are $\sigma_x = 553\ nm$ and $\sigma_z = 300\ \mu m$, respectively. We used the technique described above to get $\sigma_x = (596.69 \pm 16.32)\ nm$ and $\sigma_z = (241.49 \pm 7.94)\ \mu m$ where the errors are the statistical ones.

4 Outlook

At the moment we investigate other observables of the energy as well as the angular distribution. For example the maximal radius and an angle which characterizes the rotation of the energy distribution.

Acknowledgments

I would like to thank my supervisor Achim Stahl for all his help, Jens Dittrich for first aid in mathematical questions, Wolfgang Lohmann and Eric Switzer for correcting the English spelling and grammar.

References

[1] TESLA Technical Design Report, p II-12ff, http://tesla.desy.de/new_pages/TDR_CD/PartII/accel.html

[2] JLC-I, KEK Report 92-16, 1992, p 126, http://www-jlc.kek.jp/JLC.proposal-e.html

[3] NLC Zeroth-Order Design Report, p 785, http://www.slac.stanford.edu/accel/nlc/zdr/

[4] G. Bonvicini *et al.*, First Observation of Beamstrahlung, Phys. Rev. Lett. **62** (1989) 2381-2384

[5] G. Bonvicini and J. Welch, Large Angle Beamstrahlung as a Beam-beam Monitoring Tool, arXiv:physics/9812023, http://motor1.physics.wayne.edu/~cinabro/beamstrahlung/beamstrahlung.html

[6] TESLA Technical Design Report, p IV-89f, http://tesla.desy.de/new_pages/TDR_CD/PartIV/detect.html

[7] Daniel Schulte, GUINEA PIG, http://www-sldnt.slac.stanford.edu/nlc/programs/guinea_pig/Original%20GP%20Home.html

[8] Eric W. Weisstein, CRC Consise Encyclopedia of Mathematics, p 1197, or Eric Weisstein's World of Mathematics http://mathworld.wolfram.com/Moore-PenroseMatrixInverse.html

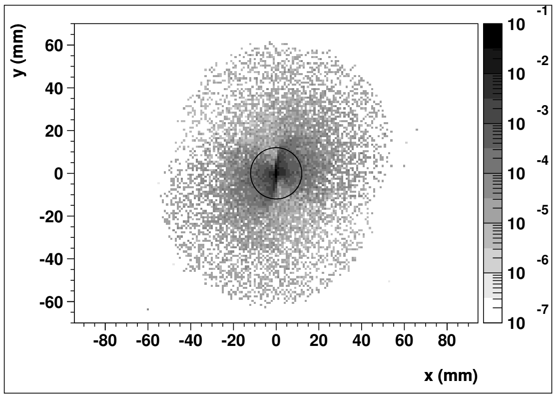

Fig. 1: *Energy distribution at LCAL for standard TESLA setup:* $\sigma_x = 553.0$ *nm,* $\sigma_y = 5.0$ *nm,* $\sigma_z = 300$ μm.

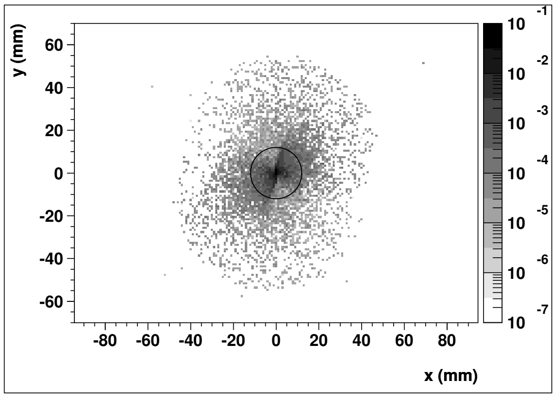

Fig. 2: *Energy distribution at LCAL for a bunch with* $\sigma_x = 829.5$ *nm corresponding to 150% of the standard TESLA setup.*

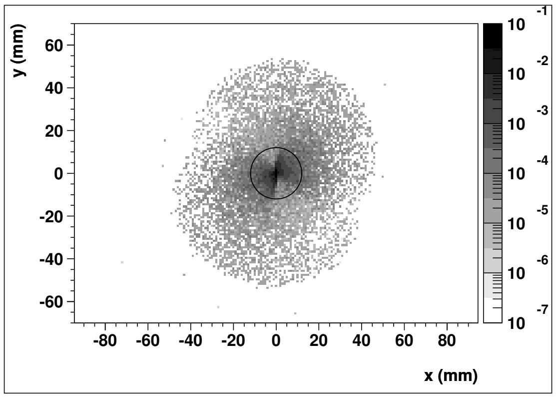

Fig. 3: *Energy distribution at LCAL for a bunch with* $\sigma_z = 450$ μm *corresponding to 150% of the standard TESLA setup.*

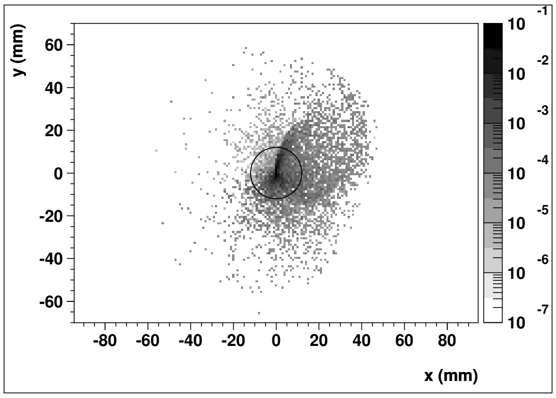

Fig. 4: *Energy distribution at LCAL for a bunch with an angle of 0.25° in the x-z plane. TESLA standard is 0.0°.*

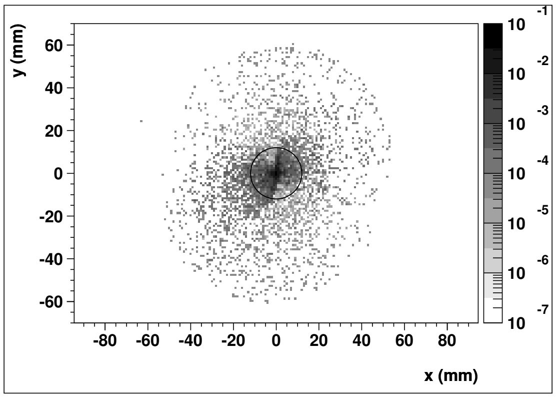

Fig. 5: *Energy distribution at LCAL for a bunch with an angle of 0.0025° in the y-z plane. TESLA standard is 0.0°.*

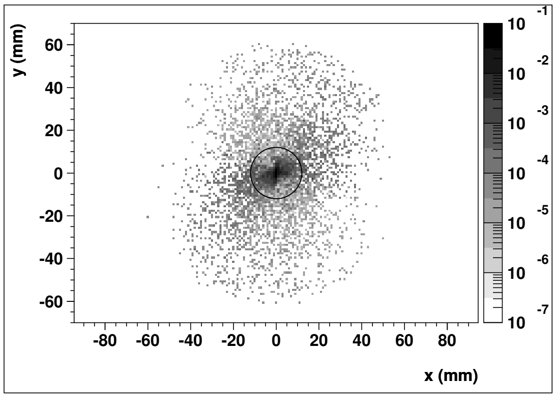

Fig. 6: *Energy distribution at LCAL for a bunch with a tranverse tilt angle of 7.5 °. TESLA standard is 0.0°.*

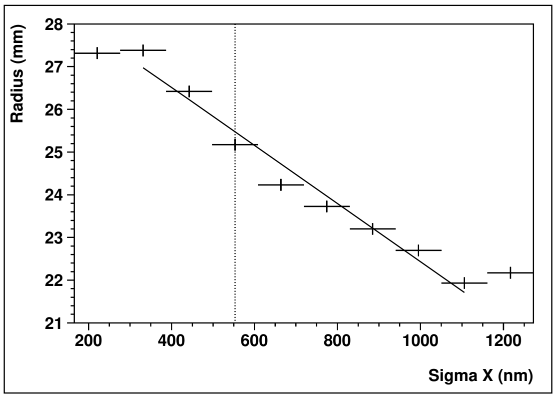

Fig. 7: *The radius versus the bunch width* σ_x

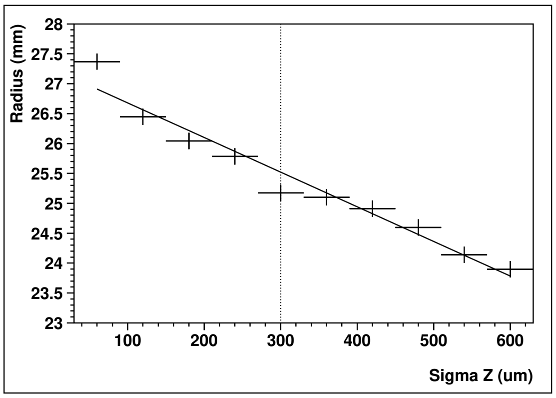

Fig. 10: *The radius versus the bunch length* σ_z

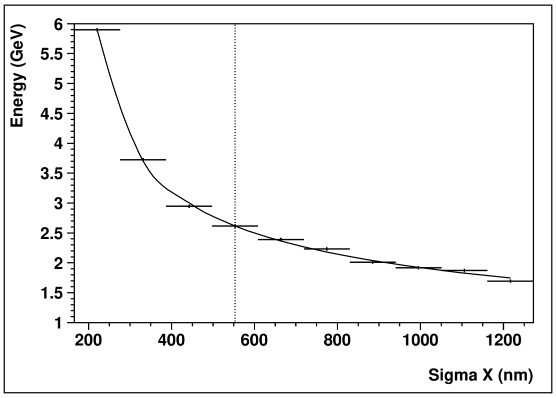

Fig. 8: *The energy versus the bunch width* σ_x

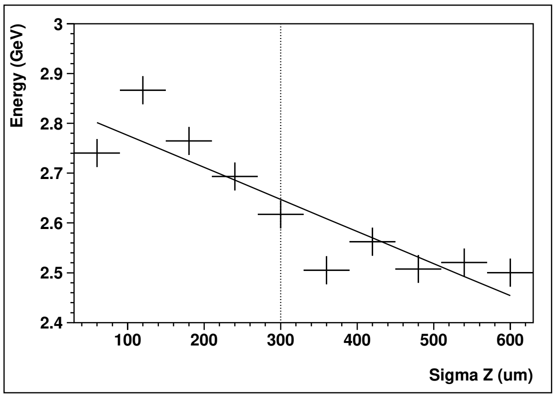

Fig. 11: *The energy versus the bunch length* σ_z

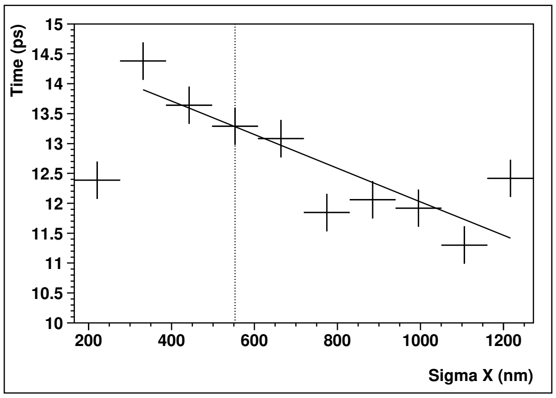

Fig. 9: *The arrival time versus the bunch width* σ_x

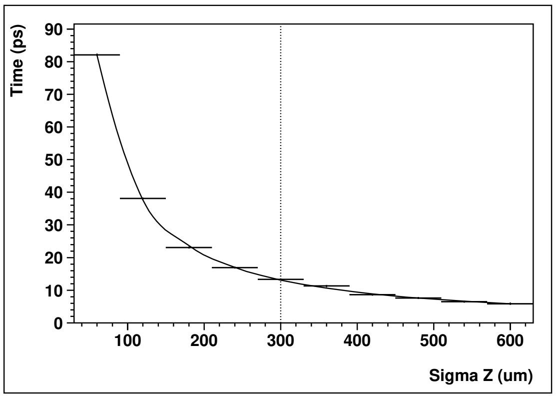

Fig. 12: *The arrival time versus bunch length* σ_z

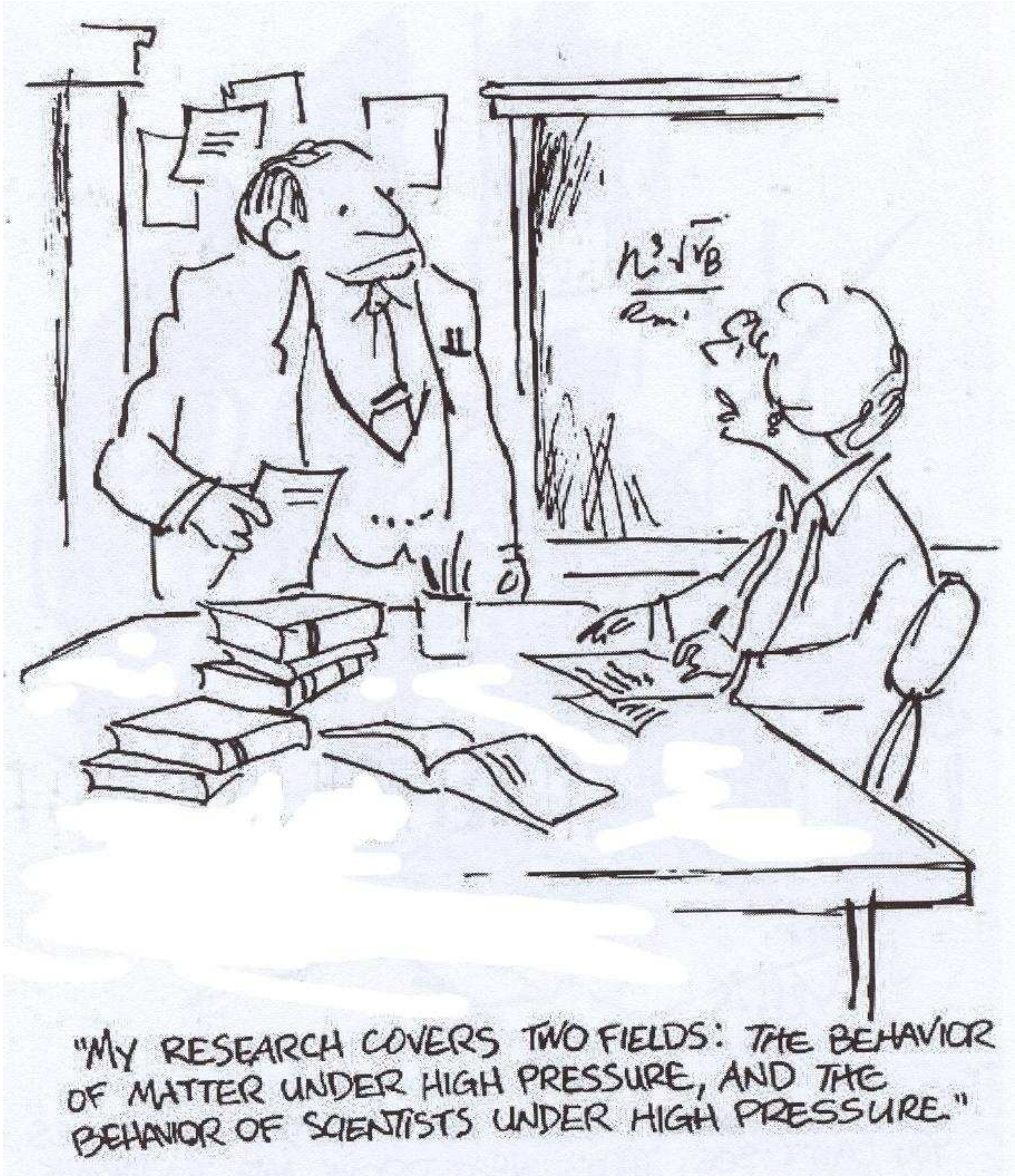
"MY RESEARCH COVERS TWO FIELDS: THE BEHAVIOR OF MATTER UNDER HIGH PRESSURE, AND THE BEHAVIOR OF SCIENTISTS UNDER HIGH PRESSURE."

Simulation of hadronic cascades in ice

Thorben Theedt
Email: theedt@web.de
Web page: http://www-zeuthen.desy.de/~theedt

During the time of the DESY SUMMER STUDENT PROGRAM 2002 I joined the AMANDA group. Amanda stands for "Antarctic Muon And Neutrino Detector Array" and one of the major aims of this group is the search for neutrino sources in the universe. My major task was the simulation of hadronic cascades in ice using a program based on the GEANT4 framework. My work was supervised by Marek Kowalski. This report gives a short overview of my work and shows the results of my simulations. For further information you may also visit my home page ore some of the web pages that are listed at the and of this report.

1 Motivation:Why is AMANDA interested in hadronic cascades?

AMANDA is a neutrino detector. It consists of optical modules that are arranged along strings in the ice of the south pole and detects the Cherenkov-light of charged particles that traverse the ice with an velocity faster than the velocity of light in this medium. The question is what happens when a neutrino interacts weakly with an atomic nuclei of the ice and what does the detector signal look like? Since there are three neutrino flavors we have to answer this question seperatly for each flavor.

- *the electron-neutrino*
  The charged current reaction for the electron-neutrino is given by equation (1).

  $$\nu_e + N \rightarrow e + X \tag{1}$$

  The electron generated in this reaction looses almost all its energy via Bremsstrahlung causing an electromagnetic shower. Due to the deep inelastic interaction with the neutrino the nuclei is destroyed and creates a collection of hadrones X. These hadrones may either decay or interact strongly with other nuclei. This is what is called a hadronic shower. The whole reaction can be described by a feynmann-diagram (Figure 1). The most frequent hadrones in an hadronic shower are the pions and the kaons. Some properties of this particles are listed in Table 1. In the AMANDA detector an electron-neutrino-event will have an extension of a few meters and create a sphere like Cherenkov light pattern.

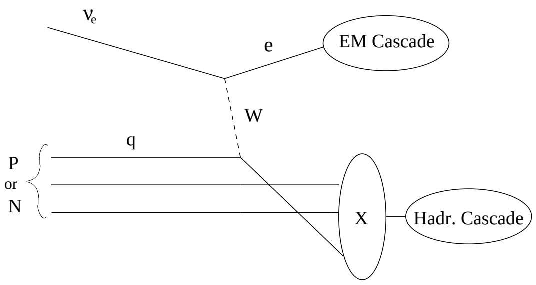

Fig. 1: *Feynmann-Diagram for reaction (1)*

- *the muon-neutrino*
  The charged current reaction for the muon-neutrino is given by equation (2)

  $$\nu_\mu + N \rightarrow \mu + X \tag{2}$$

  Because of the large mass the muon emits less Bremsstrahlung and will cover a long distance (order of km for muons with energies in the order of TeV) in the ice before it decays via one of the decay modes listed in Table 1 or interacts with a nuclei. The muon track can be reconstructed via the the signals of the optical modules and since the direction of the muon is well aligned with the neutrino direction one obtains the direction of the neutrino. For the search of neutrino point sources the muon-neutrino is the prime flavor. Due to the deep inelastic reaction the nuclei is destroyed into several hadrones causing an hadronic shower as described for the electron-neutrino.

- *the tau-neutrino*

  The charged current reaction for the tau-neutrino is given by equation (3)

  $$\nu_\tau + N \rightarrow \tau + X \tag{3}$$

  Like for the muon the energy-loss via Bremsstrahlung for the generated tau is low. Due to the small mean life time of the tau (see Table 1) the distance covered by the tau before its decay is very small. The decay of the tau leads to an electromagnetic or an hadronic shower. In the AMANDA detector a tau-neutrino-event will be seen as two superimposed spherical light-pattern.

As described above the different neutrino flavors can be distinguished by the "track" of the outgoing lepton. In all three cases the detector signal of the hadronic shower is described as spherical. The question is whether this is always true. In a hadronic shower muons may be generated and dependent on their energy they will cover a certain distance in the ice. The signals of these muons may lead to difficulties in the distinction between the different neutrino events. This is why a good knowledge of hadronic cascades is important for AMANDA. In my work I was simulating hadronic showers in ice looking for the energy spectrum of generated muons with an energy $E_\mu > 100$ MeV.

Tab. 1: *mass, mean life and decay modes of the muon, pion and kaon (All data taken from [1])*

	mass [MeV]	mean life [s]	decay modes
e^-	0.51	$1.3 * 10^{32}$	stable
μ^-	106	$2.2 * 10^{-6}$	$e^-\bar{\nu_e}\nu_\mu (\approx 100\%)$
τ^-	1777	$290.6 * 10^{-15}$	$\mu^-\bar{\nu_\mu}\nu_\tau (\approx 17\%)$ $e^-\bar{\nu_e}\nu_\tau (\approx 18\%)$ $\tau^-\nu_\tau (\approx 11\%)$
π^0	135	$8.4{*}10^{-17}$	$\gamma\gamma (\approx 99\%)$
π^-	140	$2.6 * 10^{-8}$	$\mu^-\bar{\nu_\mu} (\approx 100\%)$
π^+	140	$2.6 * 10^{-8}$	$\mu^+\nu_\mu (\approx 100\%)$
K^0	498	$0.9{*}10^{-10}$	$\pi^+\pi^- (\approx 69\%)$ $\pi^0\pi^0 (\approx 31\%)$
K^-	494	$1.2 * 10^{-8}$	$\mu^-\bar{\nu_\mu} (\approx 64\%)$ $\pi^-\pi^0 (\approx 21\%)$ $\pi^-\pi^-\pi^+ (\approx 6\%)$ $\pi^0 e^-\bar{\nu_e} (\approx 5\%)$ $\pi^0\mu^-\bar{\nu_\mu} (\approx 3\%)$
K^+	494	$1.2 * 10^{-8}$	K^+ modes are charge conjugates of the K^- modes

2 Generation of the data

The question that underlies the following analysis is this one: How many muons are created in an hadronic shower that is caused by pions (π^-) of a certain energy (0.1 TeV, 1.0 TeV and 10 TeV) and what does the energy- spectrum of the generated muons look like? The (simulated) detective volume is an ice cube with an extension of 30m. The density of the ice is set to 0.925 g/cm^3 . The first simulation (run1) starts with 10,000 π^- of 0.1 TeV, run2 with 1,000 π^- of 1.0 TeV and run3 with 10 π^- of 10 TeV. All data are obtained from a GEANT4 based program. The histograms below are created with *root*.

Remark: The generation of the data with GEANT4 takes quite a long time. To simulate a shower caused by 10,000 π^- with an energy of 0.1 TeV it takes about forty hours.

3 Results

Figure 2a shows the energy-distribution of the muons created in the shower in its differential form while Figure 2b shows the integral form. The histograms are normalized in the way that the number of muons in a bin is divided by the number of primary pions times the energy of the pions in units of TeV. In the energy range from -0.5 to 1.5 the curves have been fitted by an exponential function $f(E_\mu) = exp(aE_\mu + b)$. The resulting parameters of these fits are given in Table 2.

For a better understanding of the energy-spectrum of the muons it is interesting to know the "parent" of each muon created in the cascade.

Figure 3 shows the muon-energy-spectrum of run1 (0.1 TeV) and run2 (1.0 TeV) in its differential form divided into muons that have been caused by the decay of a pion resp. a kaon.

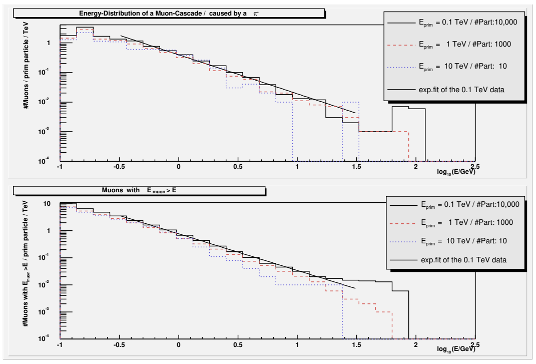

Fig. 2: *Energy- distribution of the muons generated in the shower in its a) differential b) integral form*

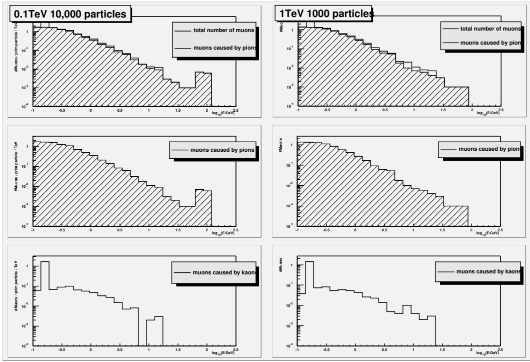

Fig. 3: *Muon-energy-distribution in its differential form devided into muons generated in a pion- or kaon- decay*

Tab. 2: *parameters of the exponential fits*

energy	constant (b)	slope (a)
diff.form		
0.1 TeV	-0.9334	-3.0291
1.0 TeV	-1.1409	-2.9850
10 TeV	-1.3079	-2.8505
int. form		
0.1 TeV	-0.2597	-3.1178
1.0 TeV	-0.5096	-3.2593
10 TeV	-0.6280	-3.8880

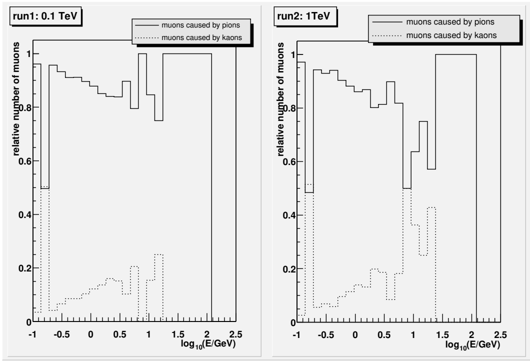

Fig. 4: *Relative number of muons created by pions resp. kaons*

As you can see most of the muons are generated by the decay of the pion. To get more detailed information Figure 4 shows the relative number of muons created by pions resp. kaons.

The next step would be to interpret the spectrum with respect to the physics of hadronic showers and the decay of hadrones to see weather the spectrum makes sense in a physically way. This seems necessary, since we are using the GEANT4 package in a way untested by experiment. A full analysis will go beyond the scope of this work. For a start there is one attribute of the spectrum that can be interpreted in the following way: As you can see in Figure 2 and 3 there is a peak at the energy region of $E_\mu = 160$ MeV and as you can see in Figure 4 more than fifty percent of the muons in this bin are due to the decay of a kaon. If one calculates the decay of a kaon in rest you get an energy of $E_{\mu,cal} = 152.487$ MeV. This value lies inside the peak-bin.

Figure 5 shows the number of muons created per primary pion. The distributions are approximated by a Poisson- distribution (4).

$$p(x) = \frac{m^x}{x!} exp(-m) \tag{4}$$

In this equation m is the mean value of the distribution and x is the number of muons generated per primary particle. The mean value can be interpreted as the multiplicity of the primary pion with respect to its energy. The values for the different energies are listed in Table3.

4 Summary and Discussion

A GEANT4 simulation has shown that hadronic showers from incident pions into ice generate a large number of low energy muons. The number of muons generated increases slightly slower than linear with the energy of the incident par-

Tab. 3: *energy dependend multiplicity of the pions for muons with E_μ > 100 MeV*

particle	energy	multiplicity	RMS
π^-	0.1 TeV	1.1593	1.114
π^-	1.0 TeV	9.5460	3.973
π^-	10 TeV	76.7273	23.460

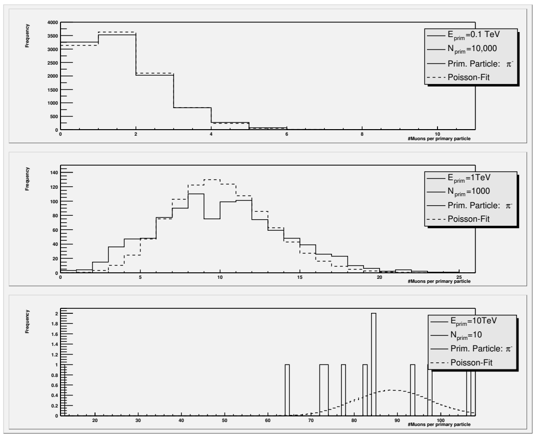

Fig. 5: *Number of muons generated per primary particle*

ticle. The muon energy spectrum, $\frac{dN}{d\log(E)}$ above 300 MeV was parameterized with an exponential. The results could have implications for AMANDA. For example, a 1 TeV hadronic cascade produces about one muon above 1 GeV, and in about 3 % of the cases a muon above 10 GeV. A muon with 10 GeV energy propagates a distance in ice of about 50 m. In order to test the effect on the AMANDA event simulation, the parameterizations of the muon multiplicity and spectrum will be included as an option in the program ksplit, designed for making cascade simulation in AMANDA more realistic.

References

[1] The European Physical Journal / Review of Particle Physics / Volume 15 2000 /Springer

[2] Richard Wigmans / Calorimetry / Energy Measurment in Particle Physics / Oxford Science

[3] Alexander Biron / Dissertation / Search for Atmospheric Muon-Neutrinos and Extraterrestric Neutrino Point sources in the 1997 AMANDA B10 Data

[4] Marek Kowalski / On the Cherenkov-light emission of hadronic and electro-magnetic cascades / Internal Report

For further information you may also visit one of the following web pages:

[5] AMANDA-WEB-PAGE: http://amanda.berkeley.edu/amanda/amanda.html

[6] GEANT4-WEB-PAGE: http://wwwinfo.cern.ch/asd/geant4/geant4.html

[7] ROOT-WEB-PAGE: http://root.cern.ch

[8] HOME-PAGE of MAREK KOWALSKI : http://www-zeuthen.desy.de/~mkowalsk

Participants of the DESY Zeuthen Summer Student Program 2002

1. **Yaroslav Rodionov**, Russia
   Email: rodyar@rambler.ru
2. **Iván Calvo**, Spain
   Email: calvorubio@hotmail.com
3. **Eric Switzer**, USA
   Email: erswitze@uchicago.edu
4. **Stephan von Coelln**, Germany
   Email: stephan_von_stephan@public.uni-hamburg.de
5. **Thorben Theedt**, Germany
   Email: theedt@web.de
6. **Antonios Garas**, Greece
   Email: agara@skiathos.physics.auth.gr

Missing reports:

- Mathias Faber
- Stefan Golla

7 **Stefan Golla**, Germany
Email: tpmilki@gmx.de

8 **Boris Skorodumov**, Russia
Email: boris_skorodumov@mail.ru

9 **Diego Rodriguez Gomez**, Spain
Email: diego@fisi35.ciencias.uniovi.es

10 **Mathias Faber**, Germany
Email: faberna@tu-cottbus.de

11 **Marco Ternick**, Germany
Email: markoternick@gmx.de

12 **Jens Dittrich**, Germany
Email: jediemail@gmx.de


1
2
3
4
5
6
7
8
9
10
11
12